================ **PHYSICS** ================

Relaxation Properties of the Nonequilibrium Polyacenequinone Surface

R. V. Afanas'eva, T. G. Ermakova, and Academician M. G. Voronkov

Dielectric spectra of amorphous polyacenequinone (PAQ) [1] can play an important role in studying kinetic phenomena in disordered semiconductors [2–4].

We have interpreted temperature dependences of the frequency position ν_m for two maxima of the tangent of the dielectric-loss angle $\tan\delta(\nu)$ in spectra of a mixture of PAQ grains with paraffin (Fig. 1, curve *1*).

The PAQ under study was obtained with the help of a technique described in [5], i.e., through the cyclic polycondensation over 24 h of pyrene with pyromellitic dianhydride in the presence of anhydrous zinc chloride at 300°C.

Curves *1–4* in Fig. 1 are evidence of the practically constant low-frequency (LF) position for the maximum of the quantity $\tan\delta(\nu)$ within the range (–60, +20°C). The change of the position of the high-frequency (HF) maximum for $\tan\delta(\nu)$ is symbatic to the temperature dependence of the electric conductivity σ for pressed samples of PAQ grains (Fig. 2).
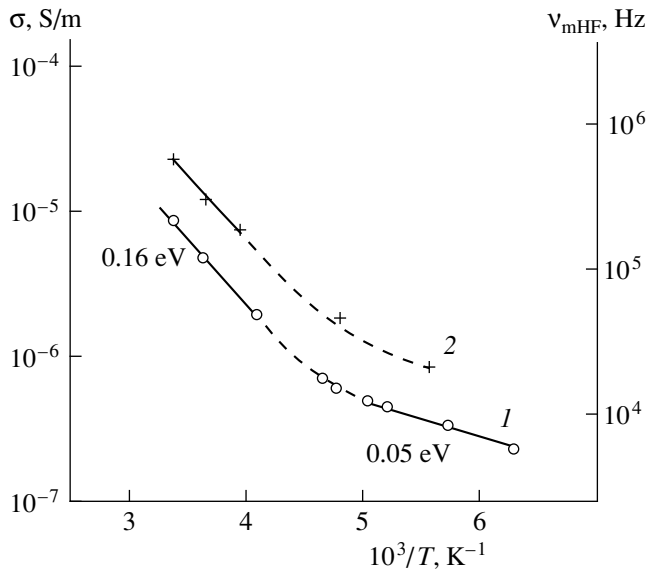
According to thermal-emf data, PAQ is a hole semiconductor [6]. For polymers with a system of conjugate bonds, this is caused, as a rule (for measurements in ambient air), by oxygen adsorption [6]. In accordance with the mass spectra of the thermal-desorption products emanating in the case of PAQ vacuum heating [7], the surface changes of this polymer and a combination of electrophysical properties caused by these changes can be associated with the effect of oxygen adsorption. The Van Ruyven model of an isotype heterojunction with double depletion can serve as a basis for relaxation processes in the surface barrier (cit. according to [8]). The correlation of the values of σ for pressed samples and ν_{mHF} in spectra of PAQ grains insulated by paraffin (Fig. 2) is a consequence of the quasi-insulated state of the surface-state systems and is associated with electronic processes in the surface space-charge regions of contacting grains. As is well known, in the equivalent circuit, this corresponds to two Schottky diodes connected opposite to each other. In an alternating electric field, this is manifested as an exchange of surface states by charge carriers predominantly from the volume of the state's own grain. In the model [9] of an intergrain barrier, such behavior is caused by the antiparallel orientation of the surface dipoles due to the redistribution of the electron density between the adsorbed oxygen and the surface-active center. It is possible that the absence of changes for ν_{mHF} within the range –60, +20°C (Fig. 1, curves *1–4*) is associated with a similar process. This indicates that the mechanism of the LF relaxation process is electron tunneling in the system of adsorption bonds.

In the model of inhomogeneous semiconductors with large-scale fluctuations in electric potential, the independence of $\nu_{mHF}(T)$ corresponds to a tunnel recombination channel for charge carriers through the regions of the potential-relief maxima [2]. In the qualitative agreement with this model, the decrease in the activation energy *W* in the low-temperature linear segment $\sigma(T)$ is accompanied by a transition from electron tunneling to a conventional process of surface capture of charge carriers (Fig. 1, curves *4*, *5*, and Fig. 2, curve *1*). According to [10], this fact is implied by the activation shift of the LF maximum for $\tan\delta(\nu)$ towards the LF-side at –90°C (Fig. 1, curve *5*). Consequently, within the temperature range corresponding to the indepen-
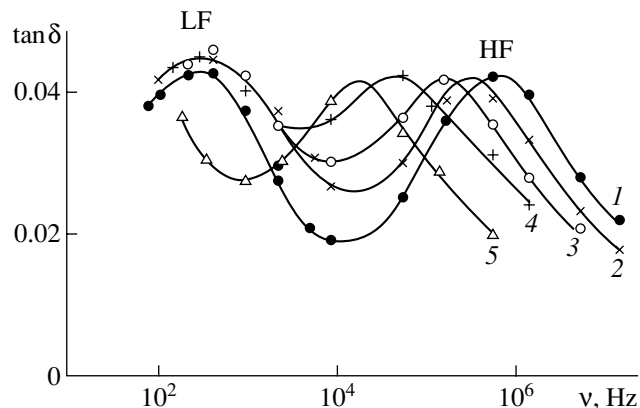
Fig. 1. Frequency dependence of $\tan\delta$ for a mixture of PAQ with paraffin at temperatures (*1*) 20, (*2*) 0, (*3*) –20, (*4*) –60, and (*5*) –90°C. The PAQ concentration, sample thickness, and diameter of electrodes are 10%, 242 μm, and 15 mm, respectively.

Favorskiĭ Institute of Chemistry, Siberian Division,
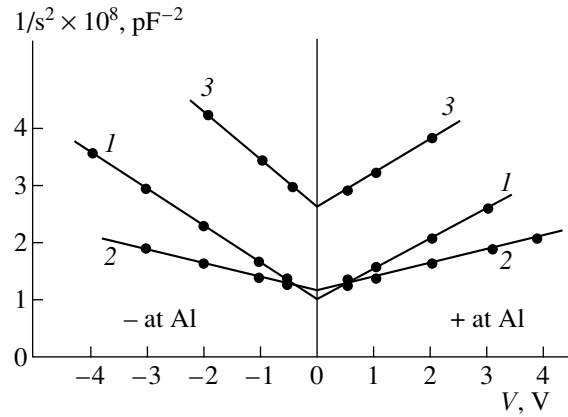*Russian Academy of Sciences, ul. Favorskogo 1,*
Irkutsk, 664033 Russia

Fig. 2. Temperature dependence of (*1*) σ for the PAQ pressed sample and (*2*) ν_{mHF} for the high-frequency maximum of $\tan\delta(\nu)$ according to the data given in Fig. 1. The sample thickness and diameter of electrodes (Ag) are 375 μm and 4.6 mm, respectively.

Fig. 3. Dependence of $1/s^2$–(*V*) according to the data of capacitance–voltage characteristics for the contact of a PAQ pressed sample with Al (the second electrode is made of Ag) in the case of two frequencies of measurement voltage at room temperature: (*1*) $N_i = 1.2 \times 10^{16}$ cm^{-3}; (*1'*) $N_i = 8.6 \times 10^{15}$ cm^{-3} and the frequency is 400 Hz; (*2*) $N_i = 2.8 \times 10^{16}$ cm^{-3}; (*2'*) $N_i = 1.2 \times 10^{16}$ cm^{-3} and the frequency is 400 Hz. Repeated measurements are performed after 25 days: (*3*) $N_i = 1.0 \times 10^{16}$ cm^{-3}; (*3'*) $N_i = 6.6 \times 10^{15}$ cm^{-3} and the frequency is 1 kHz.

dence of $\nu_{mHF}(T)$, the frequency position for the LF maximum of $\tan\delta(\nu)$ is determined by the commensurable characteristic times for surface processes of capturing and recombining charge carriers.

The correlation of values of ν_{mHF} and σ in their temperature dependence indicates the connection of the HF region of the dielectric absorption spectra with the relaxation properties of a percolation cluster. The probable mechanism of the HF relaxation process can be associated with the recharging of deep localized states of charge carriers. These states are similar to the energy levels of deep impurity centers in inorganic semiconductors [11]. In accordance with modern concepts of electronic processes in polymer semiconductors [12], the efficient conjugate fragments of the PAQ chemical structure should be considered as an organic analogue of the deep impurity centers in PAQ. In this case [13], we can expect that the concentration N_i of ionized centers determined by the slope of the capacitance–voltage characteristics for the metal–PAQ contact is consistent with the concentration $n = 2 \times 10^{16}$ cm^{-3} of free charge carriers [6]. This fact is actually observed for the Al–PAQ contact state close to equilibrium (Fig. 3, curves *1*, *1'*, *2*, *2'*). The measurement frequency of 400 Hz is close to the low-frequency limit of the dispersion region connected with the near-electrode space-charge region (Fig. 4).

The percolation theory uses the concept of quasi-equilibrium finite clusters, i.e., fragments of percolation clusters inside which a quasi-equilibrium is established during the period of the existence of the external electric field [4]. The correlation between the values of

σ and ν_{mHF} (Fig. 2) can be explained assuming that the double dielectric dispersion in the PAQ spectrum (Fig. 1, curve *1*) reflects the relaxation properties in the system of surface space-charge regions functionally identical to the family of quasi-equilibrium finite clusters. However, in accordance with the proposed interpretation of the LF- and HF-relaxation processes, the condition of quasi-equilibrium should take into account the interconnected processes of recharging the surface states and levels of bulk deep centers in the space-charge region.
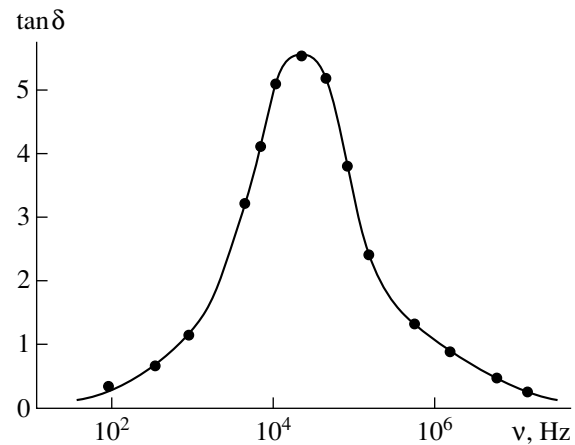
Fig. 4. Frequency dependence of $\tan\delta$ for the contact of a PAQ pressed sample with Al (the second electrode is made of Ag) at room temperature. The sample thickness and the diameter of the electrodes are 546 μm and 1 cm, respectively.

It is worthwhile to note the specific separation of functioning in the double dielectric dispersion: both LF- and HF-relaxation processes are associated with charge carriers of different signs. This fact indicates the connection of the processes under consideration with a phenomenon similar to the compensation of donor and acceptor impurities found in the case of crystalline semiconductors [3]. Following [14], we can consider the adsorbed oxygen to be playing the role of a compensating acceptor impurity for the PAQ surface layer. In our case, the main function of oxygen should be associated with the appearance of vacancies on the donors, which, according to [3], is a necessary condition for the phenomenon of hopping conductivity over localized states to take place.

REFERENCES

1. R. V. Afanas'eva, T. G. Ermakova, and M. G. Voronkov, Dokl. Akad. Nauk **369**, 329 (1999) [Dokl. Phys. **44**, 749 (1999)].

2. V. L. Bonch-Bruevich, I. P. Zvyagin, R. Kaiper, *et al.*, *Electronic Theory of Disordered Semiconductors* (Nauka, Moscow, 1981).

3. B. I. Shklovskiĭ and A. L. Efros, *Electronic Properties of Doped Semiconductors* (Nauka, Moscow, 1982; Springer-Verlag, New York, 1984).

4. I. P. Zvyagin, *Kinetic Phenomena in Disordered Semiconductors* (Mosk. Gos. Univ., Moscow, 1984).

5. R. Rosen and H. A. Pohl, J. Polym. Sci., Part A-1 **4**, 1135 (1966).

6. *Organic Semiconductors*, Ed. by V. A. Kargin (Nauka, Moscow, 1968).

7. R. Colson and R. P. Nagels, Phil. Mag. B **38**, 503 (1978).

8. B. L. Sharma and R. K. Purohit, *Semiconductor Heterojunctions* (Pergamon, Oxford, 1974; Sov. Radio, Moscow, 1979).

9. V. B. Kvaskov, Diélektr. Poluprovodn. **29**, 28 (1986).

10. A. V. Rzhanov, *Electron Processes on Semiconductor Surfaces* (Nauka, Moscow, 1971).

11. A. G. Milnes, *Deep Impurities in Semiconductors* (Wiley, New York, 1973; Mir, Moscow, 1977).

12. A. V. Vannikov, A. D. Grishina, and S. V. Novikov, Usp. Khim. **63** (2), 107 (1994).

13. E. H. Rhoderick, *Metal–Semiconductor Contacts* (Clarendon Press, Oxford, 1988, 2nd ed.; Radio i Svyaz', Moscow, 1982).

14. A. Ya. Vinnikov, A. M. Meshkov, and V. N. Savushkin, Fiz. Tverd. Tela (Leningrad) **22**, 2989 (1980) [Sov. Phys. Solid State **22**, 1745 (1980)].

Translated by T. Galkina

===== PHYSICS =====

Reflection and Absorption Characteristics of Various Physical Objects in a Millimeter Radio-Wave Range

V. I. Zagatin, V. V. Meriakri, G. S. Misezhnikov, E. E. Chigryaĭ,
and Corresponding Member of the RAS V. B. Shteinshleiger

In the last decade, a range of millimeter radio waves (wavelengths from 10 to 1 mm) were widely used in various fields of science and practical applications, e.g., in radio location, radio infrared imaging, radio communication, medicine, introscopy, etc.

In this connection, it is of importance in many cases to know the reflection and absorption characteristics of various physical objects in the millimeter wave range.

In this paper, measurement results for these characteristics at different frequencies covering almost the entire range of millimeter waves are presented.

In the regions related to the wavelengths $\lambda \approx 8$ and 4 mm, the measurements of the reflection and absorption coefficients were carried out in metallic waveguides with increased (compared to the conventional waveguides) cross-sectional dimensions. This provided conditions close to those of the normal incidence of the plane wave onto the surface of an object. The measurements of the material characteristics in the shorter wavelength regions of the millimeter wave range were carried out in quasi-optical beam guides made of nonreflecting lenses [1]. In this case, the reflection and transmission coefficients of samples onto which a practically plane wave had impinged were measured. The measurement errors for the transmission T and reflection R (in power units) did not exceed 2%.

The results obtained for the reflection coefficient modulus R (in percent) and attenuation L (dB) for various objects in the wavelength range from $\lambda \approx 8$ to 1 mm are given in the table. For measurements, the following objects were used: clothes (fabric, natural leather), structural materials (bricks, wood, rubber) and certain other items. The magnitudes of the reflection coeffi-

Reflection coefficient R and attenuation coefficient L for various objects

Object	Sample thickness, mm	$\lambda = 8$ mm			$\lambda = 4$ mm			$\lambda = 1.65$ mm			$\lambda = 1$ mm		
		R, %	L, $\frac{\text{dB}}{\text{mm}}$	I_Σ, dB	R, %	L, $\frac{\text{dB}}{\text{mm}}$	I_Σ, dB	R, %	L, $\frac{\text{dB}}{\text{mm}}$	I_Σ, dB	R, %	L, $\frac{\text{dB}}{\text{mm}}$	I_Σ, dB
Woolen cloth for coats	2–3	4	0.1		4		2	3	0.35				
Woolen cloth for suits	0.5–1	4		0.5	4		0.5	1	0.3–0.6				0.9
Silk cloth	0.2	<1		0.06				<1	2	0.4			1.25
Toilet soap	10	4	>1	>10	<1	>1	>10						
Porous rubber	10	10	0.5	5	31	0.45	4.5						
Cast plastic	10	<1	0.2	2	<1	1.5	>10						
Wood (pine) (vector **E** is perpendicular to fibers)	30	4	0.17		<1	0.33		2.5	0.38				
Natural leather	~1	<1	0.3		<1	0.5		<8	0.5				
Silicate brick	60	7	0.05		10	0.25		8	1.0				
Surface of a human body		40–50			31			22			16		

1028-3358/00/4510-0510$20.00 © 2000 MAIK "Nauka/Interperiodica"

cient from the human epidermis are also given in the table.

It should be noted that the magnitude of the reflection coefficient of an electromagnetic wave from the surface of the human body slightly depends on the particular region of the body for which the measurements were performed (arm, breast, abdomen). This testifies to the fact that the reflection is caused by the epidermis of the human body. As is seen from the data shown in the table, the reflection coefficient from the surface of a human body reduces from $R = 50\%$ to $R = 10\%$ with the shortening of the wavelength from $\lambda \approx 8$ to 1 mm.

The data obtained are important for evaluating the possibility of detecting particular objects on the human body and also certain objects behind building structures.

REFERENCES

1. V. V. Meriakri *et al.*, in *Problems of Modern Radio Engineering and Electronics*, Ed. by V. A. Kotel'nikov (Nauka, Moscow, 1980), p. 164.

Translated by T. Galkina

═══════════════════ **PHYSICS** ═══════════════════

Influence of Growth Conditions in the Case of Molecular-Beam Epitaxy on Photoluminescence Spectra of GaAs/InAs/GaAs Heterostructures with Quantum Dots near Their Initiation Threshold

Corresponding Member of the RAS V. G. Mokerov, Yu. V. Fedorov, A. V. Guk, Yu. V. Khabarov, Kh. S. Pak, and A. V. Danilochkin

Received April 17, 2000

In spite of the unabated interest in the unique properties of quantum dots, i.e., quasi-zero-dimensional objects formed during heteroepitaxial growth under conditions of an essential misalignment of lattice and substrate parameters [1–6] by the Stranski–Krastanov mechanism [7], the mechanism of their formation is not entirely clear. In our opinion, their formation especially concerns the influence of the growth rate and the time of interruption of the InAs-layer growth on the formation of quantum dots in a InAs/GaAs system. For example, in [3], the dimension of quantum dots was shown to be conserved when the growth rate decreased and only their density increased, but negligibly. In this case, according to [6], a long-term interruption of growth stimulating the surface migration of In atoms results in increasing the dimension of quantum dots for small effective thicknesses (~2 monolayers) of deposited InAs.

The purpose of this study is to investigate specifically this problem in the case of the molecular-beam epitaxy of InAs/GaAs heterostructures by means of varying the arsenic pressure P_{As4} in a growth chamber, the growth rate, and the time of interruption of the InAs-layer growth, and to subsequently investigate these properties through photoluminescence.

The heterostructures under investigation, whose cross section is shown in Fig. 1, were grown by molecular beam epitaxy on semi-insulating (001) GaAs substrates at two different arsenic pressures: $P_{As4}^1 = 8 \times 10^{-6}$ and $P_{As4}^2 = 2 \times 10^{-6}$ torr. The InAs layers were deposited at a temperature $T_s = 490°C$, and all the remaining layers were deposited at $T_s = 590°C$. While growing these heterostructures, we first deposited a buffer layer of undoped GaAs 1 μm thick onto the growth surface. InAs with an effective thickness of 2.7 monolayers was

then deposited. After this, the growth was interrupted for a certain time and, then, the following layers were deposited: a layer of undoped GaAs 4 nm thick, a layer of undoped $Al_{0.2}Ga_{0.8}As$ 100 nm thick, and, finally, an upper protective n^+ (5.5×10^{18} cm^{-3}) silicon-doped GaAs layer 6 nm thick. We investigated three regimes of interrupting the growth during InAs formation. The interruption time τ_{int} amounted to 30 s in the first regime and 180 s in the second regime. In the third case, when the so-called submonolayer-epitaxy regime [6, 8] was realized, growth was interrupted for 100 s after the deposition of each 0.3 monolayers of InAs. Thus, the 8-fold interruption of the growth for 100 s was carried out when depositing 2.7 monolayers of InAs. The last

|	
Si = 5.6×10^{18} cm^{-3}	GaAs 6 nm
Undoped layer	$Al_{0.2}Ga_{0.8}As$ 100 nm
	GaAs 4 nm
2.7 monolayers of InAs	
Undoped buffer layer	GaAs 1 μm
Semi-insulating substrate	GaAs (001)

Fig. 1. Cross section of the AlGaAs/GaAs/InAs/GaAs heterostructure with an effective InAs coating of 2.7 monolayers.

Institute of Radio Engineering and Electronics,
Russian Academy of Sciences, Mokhovaya ul. 11,
Moscow, 103907 Russia

regime is the closest to deposition at a reduced growth rate.

The photoluminescence spectra of the heterostructures under investigation were measured at $T = 77$ K. We used an Ar^+ laser with a wavelength $\lambda = 514$ nm and an emission density of up to 100 W/cm^2 as a source of photoluminescence excitation.

In Fig. 2, we show the photoluminescence spectra for four samples identical in structure (Fig. 1), but grown at various arsenic pressures P_{As4} and under various growth interruption conditions. As is seen from Fig. 2a, in the case of the sample grown at $P_{As4} = 8 \times 10^{-6}$ torr and $\tau_{int} = 30$ s, a single relatively narrow line (~15 meV in half-width) is observed in the photoluminescence spectra at $h\nu = 1.440$ eV. Increasing τ_{int} to 180 s at the same pressure $P_{As4} = 8 \times 10^{-6}$ torr leads to a certain narrowing in the original line (to 12 meV) and to the appearance of a new, narrower (~5 meV) and less intense line on the short-wave side from the original line at $h\nu = 1.467$ eV (Fig. 2b, curve 1). Decreasing the arsenic pressure P_{As4} to 2×10^{-6} torr at $\tau_{int} = 180$ s leads to dramatic modifications in the photoluminescence-spectrum shape (see curve 2 in Fig. 2). The entire spectrum is shifted to lower energies $h\nu$ (larger wavelengths λ), and, in this spectrum, a structure consisting of four new lines at $h\nu_1 = 1.295$ eV, $h\nu_2 = 1.314$ eV, $h\nu_3 = 1.358$ eV, and $h\nu_4 = 1.396$ eV appears. Figure 2c shows the photoluminescence spectrum of the sample also grown at a reduced pressure $P_{As4} = 2 \times 10^{-6}$ torr, but in the submonolayer-epitaxy regime (at the 8-fold interruption of the growth for 100 s). In this case, a single wide band (~80 meV) is observed with a peak at 1.394 eV.

In discussing the results presented, we, following authors of [6], proceed from the fact that, in the course of the heteroepitaxy of InAs on GaAs and depending on the growth condition, the formation of three different morphological aggregations of InAs is possible: a thin wetting layer, two-dimensional flat domains, and three-dimensional coherent islands, i.e., the quantum dots. In correspondence with their dimensions, we must observe the most short-wave and narrow photoluminescence line for a thin wetting layer; a somewhat more long-wave line for plane domains; and the widest bands for three-dimensional islands, i.e., quantum dots. Based on this fact, we may propose the following interpretation of the photoluminescence spectra in Fig. 2. The photoluminescence line at $h\nu = 1.440$ eV in Fig. 2a for the sample grown at a high arsenic pressure corresponds to two-dimensional plane InAs domains. Increasing τ_{int} for the same pressure P_{As4} (curve 1 in Fig. 2b) not only does not lead to the formation of larger islands, but, on the contrary, stimulates stabilization of a thin wetting layer (the line at $h\nu = 1.467$ eV), possibly at the expense of redistributing the material of the plane two-dimensional domains. On the other hand, decreasing the arsenic pressure from 8×10^{-6} to $2 \times$
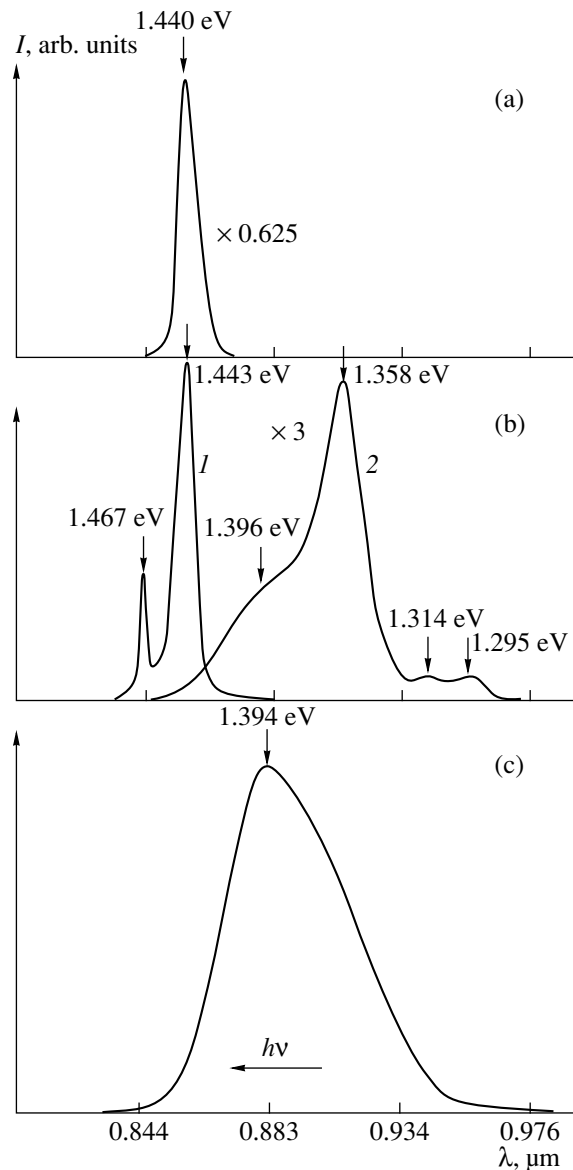
Fig. 2. Photoluminescence spectra for the AlGaAs/GaAs/InAs/GaAs heterostructures under investigation with an effective InAs coating of 2.7 monolayers: (a) photoluminescence spectrum of the sample grown at $P_{As4} = 8 \times 10^{-6}$ torr and $\tau_{int} = 30$ s; (b) photoluminescence spectrum of the sample grown at (1) $P_{As4} = 8 \times 10^{-6}$ torr and $\tau_{int} = 180$ s and (2) $P_{As4} = 2 \times 10^{6}$ torr and $\tau_{int} = 180$ s; and (c) photoluminescence spectrum of the sample grown at $P_{As4} = 2 \times 10^{-6}$ torr in the submonolayer regime of growth.

10^{-6} torr stimulates the formation of three-dimensional islands of quantum dots (curve 2 in Fig. 2b). The existence of four peaks in this spectrum indicates the presence of four groups of three-dimensional islands with a small spread of dimensions (dispersion) within each of these groups. For a more than four-fold decrease in the growth rate under conditions of a low arsenic pressure $P_{As4} = 2 \times 10^{-6}$ torr, a group of islands is formed with a

wide distribution over the corresponding dimensions, as follows from Fig. 2c.

From here, we can make the following conclusions. At a high arsenic pressure $P_{As4} = 8 \times 10^{-6}$ torr in the growth chamber, the formation of InAs plane domains (presumably three-monolayer domains) is predominant. An increase in the interruption time also contributes to the stabilization of a thin wetting layer (presumably of the two-monolayer variety), whereas no three-dimensional islands, i.e., quantum dots, are formed (in contrast to the data from [6]). Such a situation can be explained on the basis of the fact that, for an excess in arsenic, the majority of In atoms react with arsenic atoms at the substrate and their surface migration is limited by the wetting-layer boundaries and by flat domains arranged on it. The migration of In atoms, which is, obviously, more efficient the longer the growth interruption, improves the uniformity of the elastic-stress distribution; that is, it decreases the amplitude of their fluctuations in the layers formed. This leads to the stabilization of the layer-by-layer growth, not manifesting itself in a transition to the three-dimensional quantum dots for an effective thickness of InAs coating of less than 2.7 monolayers.

On the other hand, a reduction in the arsenic pressure, which is known to be a destabilizing factor in layer-by-layer growth and beneficial for the surface segregation of In atoms, evidently leads to an increase in the amplitude of fluctuations of elastic stresses in the deposited InAs layers stimulating the formation of the quantum dots (Fig. 2b, curve *2*, and Fig. 2c). It is of interest to note that, depending on the growth conditions and also on the state of the substrate surface, it is possible that both one (Fig. 2c) and several groups of quantum dots are formed (Fig. 2b, curve *2*). The quantum dots formed differ in mean dimensions; however, this last fact is irreproducible from process to process.

The data obtained indicate the important role played by kinetic parameters in forming quantum dots in the InAs on the GaAs system near the critical thickness of InAs. The surface migration of In atoms depending on the arsenic-flux density, the growth rate, the time of growth interruption, and the state of the substrate surface (including uncontrollable potential barriers limiting the migration) determine the conditions for quantum-dot initiation, their density, the mean dimension (or even several characteristic dimensions), and the distribution in these dimensions.

It should be noted that a somewhat higher value of 2.7 monolayers for the InAs critical thickness, for which quantum dots arise in the samples under investigation, compared to the values of 1.6–1.7 monolayers reported in the literature, can be associated with the higher temperature $T_s = 490°C$ (commonly, $T_s < 480°C$) of layer deposition. In fact, an elevated deposition temperature must favor a more efficient surface migration of In atoms and, correspondingly, a decrease in the amplitude of the elastic-stress fluctuations in the InAs layers. This improves their homogeneity and leads to stabilization of the two-dimensional growth and to a delay in the onset of quantum-dot formation.

ACKNOWLEDGMENTS

REFERENCES

1. D. Leonard, K. Pond, and P. M. Petroff, Phys. Rev. B **50**, 11 687 (1994).

2. J. M. Moison, F. Houzay, F. Barthe, *et al.*, Appl. Phys. Lett. **64**, 196 (1994).

3. G. S. Solomon, J. A. Trezza, and J. S. Harris, Jr., Appl. Phys. Lett. **66**, 3161 (1995).

4. G. S. Solomon, J. A. Trezza, and J. S. Harris, Jr., Appl. Phys. Lett. **66**, 991 (1995).

5. P. D. Wang, N. N. Ledentsov, C. M. Sotomajor Torres, *et al.*, Appl. Phys. Lett. **64**, 1526 (1994).

6. N. N. Ledentsov, V. M. Ustinov, V. A. Shchukin, *et al.*, Fiz. Tekh. Poluprovodn. (St. Petersburg) **32**, 385 (1998) [Semiconductors **32**, 343 (1998)].

7. I. N. Stranski and L. von Krastanov, Akad. Wiss. Let., Mainz, Abh. Math.-Naturwiss. Kl. **146** (1939).

8. Zh. I. Alferov, D. Bimberg, A. Yu. Egorov, *et al.*, Usp. Fiz. Nauk **165**, 163 (1995).

Translated by V. Bukhanov

1/*f* Noise in Oscillatory Modes of Combustion

A. V. Reshetnikov, Corresponding Member of the RAS V. P. Koverda, V. N. Skokov, and A. V. Vinogradov

Received March 15, 2000

Fluctuation processes whose power spectrum varies inversely proportional to the frequency (flicker noise, or 1/*f* noise) are a subject of thorough investigations for many years. First discovered in electric circuits, 1/*f* noise is observed in systems of various nature (geophysical, astrophysical, biological, ecological, etc.). Presently, extensive data concerning the properties of the flicker noise in particular systems (see, e.g., reviews [1, 2]) are accumulating. For example, one of the most known studies involves a model according to which the 1/*f* noise is the consequence of the superposition of independent Lorentz sources having the relaxation-time distribution function $g(\tau) \sim \tau^{-1}$ [1, 2]. Thermal models are also widely discussed in which the thermal conduction mechanisms [3] are considered to be responsible for the 1/*f* noise in solids. Explaining experimental manifestations of 1/*f* noise in particular physical systems can be problematic when using the current models; we run into problems in attempting to explain the origin of the 1/*f* noise in systems of different natures. In spite of long-standing efforts, no commonly accepted picture of this phenomenon has been available until now and the mechanisms leading to fluctuations obeying the 1/*f* spectrum are often unclear. Therefore, the problem of searching for new systems with flicker noise and of constructing new models for this phenomenon remains urgent.

The low-frequency divergence for the spectral density of the fluctuations testifies to the fact that no characteristic time scale for the process with a flicker spectrum exists. This fact makes it possible to assume that the system is in the vicinity of a critical phase transition. Interest in random processes with diverging spectral characteristics has risen sharply in recent years in connection with the discovery of the phenomenon of self-organized criticality [4]. In the case of self-organized criticality, the system arrives at the critical state as a result of its evolution and no fine tuning of the controlling parameters is required. The concept of self-organized criticality is reasonably general; however, it could only be realized experimentally, until recently,

───────────
*Institute of Thermal Physics, Ural Division,
Russian Academy of Sciences, Pervomaĭskaya ul. 91,
Yekaterinburg, 620219 Russia*

using the model system of a "sand pile." In [5–7], a hypothesis was presented to the effect that the self-organization of the critical state can be a consequence of the intersection and the interaction of subcritical and supercritical phase transitions.

In studies [5, 6, 8], fluctuations with 1/*f* spectrum were found for the case of changing the regimes of boiling for nitrogen on a surface of thin films of high-temperature superconductors under the conditions of Joule self-heating. In this case, the overlap and the interaction of two nonequilibrium phase transitions occur: the subcritical transition from bubble boiling to film boiling and the postcritical transition associated with the localization of Joule heat release in a heat domain. In [9], thermal fluctuations with 1/*f* and 1/*f*^{2} spectra were discovered for the film boiling of water on a vertically oriented wire heater. The similarity between the process under investigation and the self-organized criticality phenomenon was also noted. In order to explain the experimental results, we propose a mathematical model [5–7]. This model describes nonequilibrium phase transitions in a lumped system which represents the system of two nonlinear stochastic equations:

$$\frac{dx}{dt} = -xy^2 + y + \Gamma_1(t),$$
$$\frac{dy}{dt} = -yx^2 + \gamma x + \Gamma_2(t), \tag{1}$$

where x and y are the interacting order parameters, $\Gamma_1(t)$ and $\Gamma_2(t)$ are the Gaussian δ-correlated noises, and the parameter $\gamma > 1$ takes the presence of external fluxes into account. This system, describing the dynamics of intersecting subcritical and postcritical phase transitions, transforms white noise into two stochastic processes with spectral densities proportional to 1/*f* and 1/*f*^{2}. It is possible to suggest various sets of nonlinear stochastic equations, including potential sets [10] similar to (1), which can predict that fluctuations with diverging spectral characteristics do exist in the case of two intersecting and interacting phase transitions. The intersection and the interaction of two nonequilibrium phase transitions is a reasonably frequent phenomenon. For this reason, 1/*f* noise can be expected in a wide class of processes accompanied by phase transitions. A classical example of a nonequilibrium phase transi-
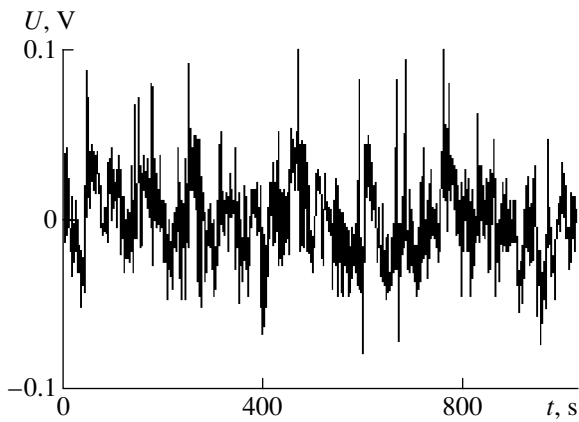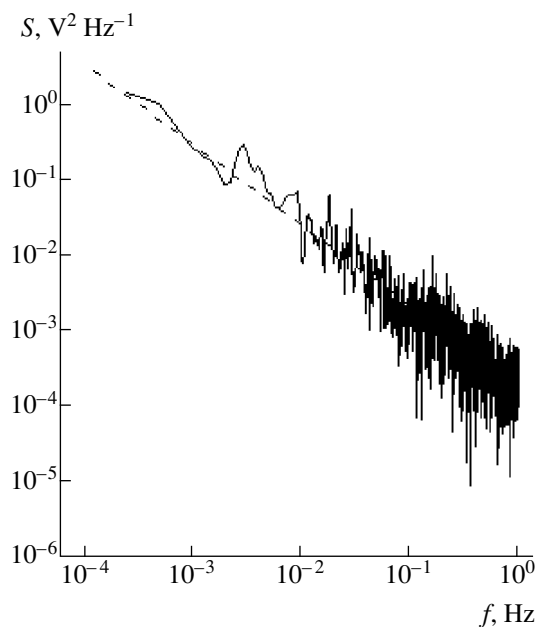
Fig. 1.

Fig. 2.

tion is represented by combustion processes. The propagation of the combustion front in a quiescent medium is described for the simplest case by two dynamic variables, i.e., by temperature and the concentration of a combustible substance, which can be considered the order parameters. When certain conditions (the ratio between the coefficients of thermal conduction and diffusion) are fulfilled, various self-oscillation modes of travelling are observed for the combustion waves [11]. In the case of the combustion of volatile substances, the chemical reaction of vapor oxidation can be accompanied by boiling of the condensed phase. In this case, we have the superposition of two transitions, i.e., the chemical reaction of oxidation and the boiling. The role of an external noise is played by random acts of boiling. The interaction of these two transitions may result in peculiar features of combustion-front dynamics.

In this study, we present the results of our experimental investigation devoted to flame-front fluctuations in the combustion of a flat porous wick impregnated with ethyl alcohol.

To provide for the boiling of a condensed phase in a combustion of vapors, it is necessary that the flame front not cover the entire wick. The experiments carried out show that such a condition is satisfied by the use of a flat wick clamped by metal plates. In this case, the flame propagates along a thin horizontal wick surface and stops near its ends. At the wick ends, no combustion takes place, owing to an oxygen deficit. The oxygen deficit results from the presence of small gaps between the wick and the metal plates. In combustion, alcohol impregnating the wick ends is heated due to the thermal conduction and its explosive boiling occurs. Such boiling can be sometimes recognized by characteristic snaps. The acts of boiling are random. When boiling, a portion of the vapors is ejected and ignites. This was observed in the form of flame splashes at the wick ends.

The dimensions of the wick were approximately 2 cm by 1 mm. Two platinum wires 20 μm in diameter were placed in the flame zone. A direct transport current of ~50 mA was passed through these wires. The voltage drop across the wires was detected with S9-8 digital oscilloscopes connected to a computer. Depending on the displacement of the wire probes, we can judge the combustion-front fluctuations in various parts of the flame and the mutual correlation between such fluctuations. In order to prevent the effect of random air flows on the flame dynamics, the burning wick was placed in a glass box.

In Fig. 1, we show one of the oscillograms for the voltage drop across the wire probe arranged along the burning wick surface at a distance of about 2 mm. Near zero, the distribution function for the oscillation amplitudes is well approximated by the Gaussian normal distribution. However, in the region of large ejections, deviations from the Gaussian dependence are essential. In the case of the simultaneous recording oscillograms from two wires, we discovered a spatial correlation between oscillations even in the case where the probes were widely spaced. This testifies to the fact that the source of stochastic oscillation is localized near the combustion front.

From the measured oscillograms, the spectral densities of fluctuations were found using the Fourier-transform method. For widening the frequency range, which was determined by the oscilloscope buffer memory (2048 points) for a single oscillogram, the measurements were carried out at various time samplings. Figure 2 shows the spectrum of oscillations for the voltage drop across the probe arranged parallel to the wick's surface. The dashed line in Fig. 2 corresponds to the dependence $S(f) \sim f^{-0.98}$; i.e., the $1/f$ behavior of the spectrum is observed. Figure 2 also shows that such a

dependence extends over four decimal orders of frequency.

It should be noted that, when using wicks of another shape, in particular, cylindrical wicks, the flicker noise is only occasionally observed. This is likely associated with the fact that, in this case, it is more difficult to provide the conditions of local boiling ahead of the flame front.

Thus, the boiling of a fuel ahead of the combustion front can result in stochastic oscillations of the reaction front with the spectral density inversely proportional to the frequency, which affirms the critical behavior of the system. Such behavior stems from the interaction of two processes, i.e., a chemical reaction and explosive boiling. The boiling is the typical first-order phase transition. The exponential character of the heat release in the combustion reaction yields grounds for considering this process a postcritical nonequilibrium phase transition. In other words, the intersection and the interaction of two phase transitions may lead to the self-organization of the critical state of the system. This fact presents fresh insight into the nature of self-organized criticality, the spatial distribution of the system being optional.

The results of this study testify to the fact that flicker noise is not necessarily a result of observations of natural phenomena; it can be detected in simple, intentionally posed laboratory experiments.

REFERENCES

1. Sh. M. Kogan, Usp. Fiz. Nauk **145**, 285 (1985) [Sov. Phys. Usp. **28**, 170 (1985)].
2. G. P. Zhigal'skiĭ, Usp. Fiz. Nauk **167**, 623 (1997) [Phys. Usp. **40**, 599 (1997)].
3. R. F. Voss and J. Clarke, Phys. Rev. B **13**, 556 (1976).
4. P. Bak, C. Tang, and K. Wiesenfeld, Phys. Rev. A **38**, 364 (1988).
5. V. P. Koverda, V. N. Skokov, and V. P. Skripov, Zh. Éksp. Teor. Fiz. **113**, 1748 (1998) [JETP **86**, 953 (1998)].
6. V. P. Koverda and V. N. Skokov, Physica A (Amsterdam) **262**, 376 (1999).
7. V. P. Koverda and V. N. Skokov, Dokl. Akad. Nauk **366**, 752 (1999) [Dokl. Phys. **44**, 350 (1999)].
8. V. P. Koverda, V. N. Skokov, and V. P. Skripov, Pis'ma Zh. Éksp. Teor. Fiz. **63**, 739 (1996) [JETP Lett. **63**, 775 (1996)].
9. V. N. Skokov, V. P. Koverda, and A. V. Reshetnikov, Pis'ma Zh. Éksp. Teor. Fiz. **69**, 590 (1999) [JETP Lett. **69**, 636 (1999)].
10. V. N. Skokov and V. P. Koverda, Pis'ma Zh. Tekh. Fiz. **25**, (9) (1999) [Tech. Phys. Lett. **25**, 341 (1999)].
11. A. G. Merzhanov and É. N. Rumanov, Usp. Fiz. Nauk **151**, 553 (1987) [Sov. Phys. Usp. **30**, 293 (1987)].

Translated by V. Bukhanov

═══ PHYSICS ═══

Experimental Evidence in Favor of the Unified Field Theory

Corresponding Member of the RAS O. I. Sumbaev

Two surprising facts were previously considered [1]. First, the standard tabular masses $M_i \pm \sigma M_i$ of fundamental particles correspond best, i.e., within the least mean-square deviation

$$S_\varepsilon = \frac{\sum_i (M_i - D^* n_i)^2}{N},\qquad(1)$$

to the integer one-dimensional sequence (n_i are integer numbers) with period D^* surprisingly close to the tripled electron mass [2]:

$$\delta = \frac{D^* - 3m_e}{3m_e} = -(6.3 \pm 6.5) \times 10^{-2}.\qquad(2)$$

Second, the mass differences for pairs of fundamental particles (see Fig. 1) whose masses are known within an error of less than 2 MeV are multiply repeated and equal the unified value $\bar{E} \simeq 440$ MeV, which satisfies the relationship

$$\frac{m_e}{\bar{E}} = 1.151 \times 10^{-3} \simeq \frac{\alpha}{2\pi} = 1.159 \times 10^{-3}.\qquad(3)$$

Here, $\alpha \simeq 1/137$; i.e., the ratio of the electron mass to the aforementioned value coincides to an accuracy of 1% with the fine structure constant divided by 2π [3].

The surprising and paradoxical nature of these facts, i.e., their contradiction of the accepted paradigms of physics, disappears if

(1) multiple experimental observations of the Sukhoruchkin effect assert that the electron mass m_e
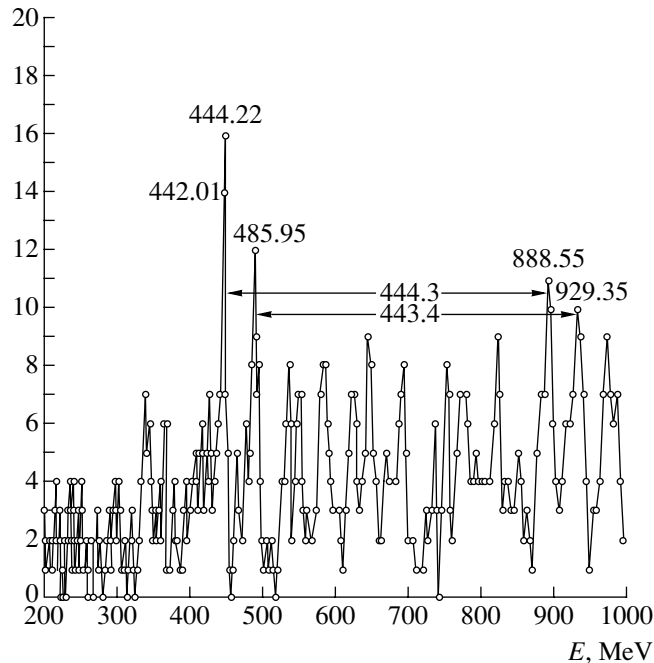
Ideohistogram of the density of possible mass differences $\Delta M_{ki} = M_k - M_i$ between leptons and hadrons (for masses known within an accuracy of $\sigma M_i \le 2$ MeV (Data Booklet, ed. AIP, 1992). The ideohistogram step (the channel width) is $\Delta E = 0.005E$. Numbers above the maxima represent the positions (expressed in MeV) of the channel centers.

Konstantinov Institute of Nuclear Physics, Russian Academy of Sciences, Gatchina, St. Petersburg, 188350 Russia

has a value or integer-multiple equal to the observed singularities [4]

or if (2) Einstein's vision of a unified universal theory of interaction [5] anticipates the possibility of reducing all known interactions to one unified interaction.

The evident nontrivial and controversial nature of this situation ecourages the author to publish his preprint [1] on a wider scale.

Indeed, the situation is changing rapidly and even today, i.e., in the six years after the preprint was published, more experimental evidence in favor of the existence of the Sukhoruchkin effect, i.e., the fact observed in [6], is being obtained. It is also quite important that attempts to develop the unified (in the spirit of Einstein [5]) theory of fundamental particles have been published (see [7] and, especially, [8]).

ACKNOWLEDGMENTS

REFERENCES

1. O. I. Sumbaev, Preprint No. 1882, PIYaF (St. Petersburg Institute of Nuclear Physics, Russian Academy of Sciences, Gatchina, 1993), p. 8.

2. R. Frosch, Nuovo Cimento A **104**, 913 (1991).

3. Sukhoruchkin, LNPI Res. Rep. 1990–1991 (St. Petersburg, 1992), p. 92.

4. O. I. Sumbaev, Preprint No. 1551, LIYaF (Leningrad Institute of Nuclear Physics, Academy of Sciences of the USSR, Leningrad, 1989); Preprint No. 1637, LIYaF (Leningrad Institute of Nuclear Physics, Academy of Sciences of the USSR, Leningrad, 1990); Preprint No. 1811, PIYaF (St. Petersburg Institute of Nuclear Physics, Russian Academy of Sciences, Gatchina, 1992).

5. A. Einstein, in *Collection of Scientific Papers* (Nauka, Moscow, 1965), p. 689.

6. O. I. Sumbaev, Preprint No. 2296, PIYaF (St. Petersburg Institute of Nuclear Physics, Russian Academy of Sciences, Gatchina, 1999).

7. F. A. Gareev, in *Proceedings of the II International Workshop on Nuclear and Physical Research Planned for UKP-2-1, October 7–9, Almaty, 1998*; Preprint No. 13-98, IYaF AN Republic of Kazakhstan (Institute of Nuclear Physics, Kazakhstan Academy of Science, Almaty, 1998), pp. 115–148.

8. S. B. Alemanov, http://theory.da.ru, 1999.

Translated by V. Devitsyn

Change in Structure of a Detonation Wave
in 2',2',2'-Trinitroethyl-4,4,4-Trinitrobutyrate with Initial
Density Increase

A. V. Utkin, S. V. Pershin, and Academician **V. E. Fortov**

Received June 5, 2000

According to classical concepts [1], a steady-state detonation wave consists of a shock wave and the zone of chemical reaction following this wave. In this zone, the pressure falls and the substance expands, i.e., the von Neumann spike is formed. The validity of this model is confirmed by numerous experiments, and its ability to describe detonation in the majority of explosives is beyond question. However, in high-density hexagen and octagen, the authors of [2] registered a pressure increase instead of the von Neumann spike in the reaction zone. The assumption that a steady-state detonation wave can propagate without the von Neuman spike raises doubts concerning the correspondence of the final state of the explosion products to the Chapman–Jouguet point and the selection rules of the detonation velocity. The validity of these concepts is determined by the reliability of experimental data fixing features of the detonation conversions in condensed explosives. In particular, it is of interest to study the character of the change in the structure of a detonation wave with an increase in the initial density of the explosives used. This paper is devoted to the study of the above-mentioned change.

As the object of investigation, we choose 2',2',2'-trinitroethyl-4,4,4-trinitrobutyrate $C_6H_6N_6O_{14}$ (TNETB), a powerful explosive with a low-negative (–4.15%) oxygen balance and a monocrystal density of 1.839 g/cm^3 [3, 4]. The TNETB sensitivity to mechanical actions is at a level of hexagen sensitivity, but the heat of the explosive conversion is in excess of that of the hexagen. The layout of the experiments is shown in Fig. 1. Detonation was initiated by a shock wave with an amplitude larger than 4 GPa, which was formed by a plane-wave generator (*1*). The diameter of the charges was 30 mm; their length ranged from 40 to 80 mm, which ensured the attainment of a steady-state regime of detonation. The wave profiles were recorded on a VISAR laser interferometer with a time resolution of ~3 ns and an

accuracy of velocity measurement of ±5 m/s independent of the value of the absolute velocity [5]. The probing radiation was reflected from a 100- to 400-μm-thick aluminum foil (*2*) placed between the charge end and water window (*3*). The experimental data present velocities registered for the foil surface adjoining the water window. They reflect all of the structural details of the reaction zone in the steady-state detonation wave.

The results of the experiments are presented in Fig. 2. The initial charge density ρ_0, thickness of the aluminum foil h_{Al}, and ratio of the charge diameter and charge length $\varnothing/l$ are presented in the table for each experiment, and the fact of registration of the von Neumann spike or the velocity increase in the reaction zone is also noted by indicating the characteristic time. At an initial density of 1.48 g/cm^3 (experiment 1), a velocity drop of approximately 300 m/s, caused by the presence of the von Neumann spike in the explosive, whose duration attains approximately 50 ns, is observed after the shock. The rise in the velocity 50 ns after the shock is related to the wave circulation in the 200-μm-thick foil situated between the water window and the explosive. The use of a 400-μm-thick foil (experiment 2) increases the circulation time, thus allowing us to refine the duration of the von Neumann spike and evaluate the character of its decay as far as it propagates along the foil. An increase in ρ_0 to 1.51 g/cm^3 (experiment 3) leads to a decrease in the spike duration by ~10 ns and a reduction of its amplitude to 200 m/s. However, even at $\rho_0 = $
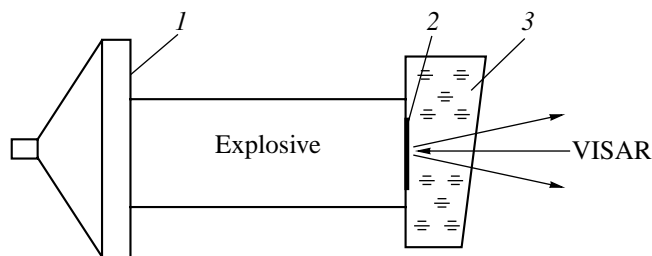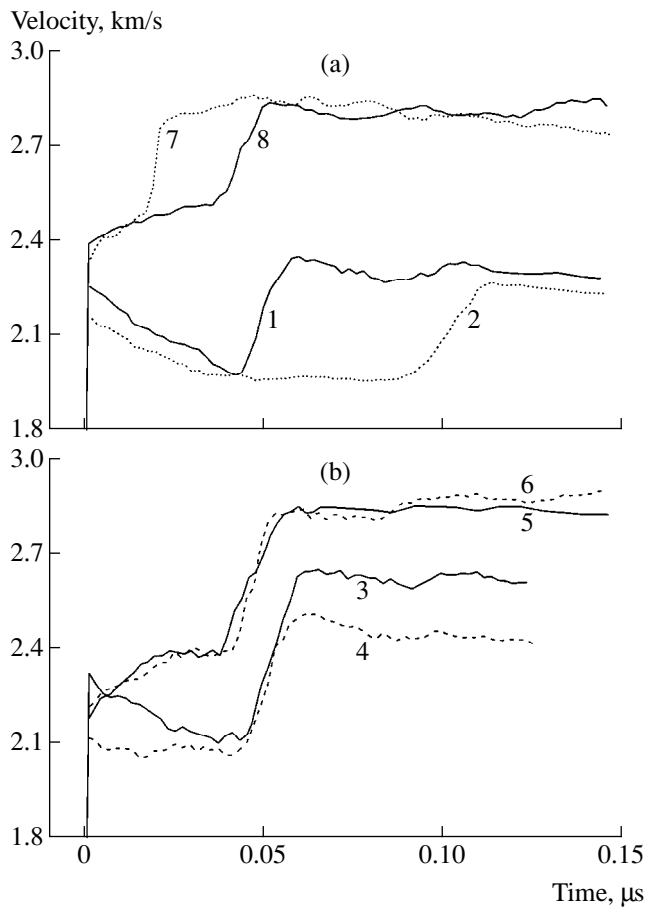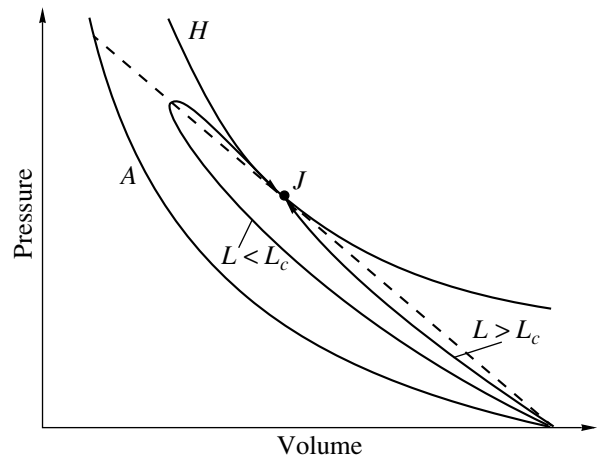

Fig. 1. Layout of the experiment: (*1*) plane-wave generator; (*2*) aluminum foil; and (*3*) water window.

*Institute of Problems of Chemical Physics, Russian
Academy of Sciences, Chernogolovka, Moscow oblast,
Russia*

Velocity, km/s

Fig. 2. Velocity of the boundary between the foil and water-window.

Fig. 3. Phase trajectories in the pressure–volume plane. *A* and *H* are the Hugoniot adiabat and the detonation adiabat, respectively; *J* is the Chapmán–Jouguet point; the dashed line is the Michelson straight line.

the charge length (experiments 5, 6). This fact is proof of the presence of a steady-state detonation regime in all experiments conducted. Note that the mass velocity corresponding to the final state of the explosion products (in the presence of the von Neumann spike, this is the Chapmán–Jouguet point) increases with the initial density. This is not the case in the vicinity of $\rho_0 = 1.56$ g/cm^3 (Fig. 2b), where an anomalous character of the velocity variation is observed: it is lower by approximately 50 m/s at a density of 1.56 g/cm^3 compared to that at a density of 1.51 g/cm^3. This can be explained by the presence of a transition to an uncompressed detonation regime at the moment of the von Neumann spike disappearance.

Thus, the experimental data obtained agree with the assumption that the steady-state detonation can exist without the von Neumann spike. Nevertheless, the probability that the reaction time is shorter than 4 ns and that the applied technique does not resolve the von Neumann spike cannot be excluded. It is, therefore, difficult to understand the qualitative change in the wave structure, whereas a monotonic pressure rise in the

1.56 g/cm^3, velocity profile 4 is subjected to qualitative changes: the von Neuman spike disappears and a domain of constant parameters arises behind the shock. Upon further increase of the initial explosive density, an ~100 m/s increase in the velocity is recorded immediately at the time of ~30 ns after the shock. Note that a good reproducibility of the structure of the reaction zone is observed at an invariable charge configuration (experiments 7, 8), as well as at a twofold increase in

Parameters of the experimental assembly

N	ρ_0, g/cm^3	h_{Al}, μm	$\varnothing/l$, mm/mm	Remarks
1	1.48	200	30/42	Von Neuman spike, 50 ns
2	1.48	400	30/42	Von Neuman spike, 50 ns
3	1.51	200	30/42	Von Neuman spike, 40 ns
4	1.56	200	30/42	Plateau
5	1.61	200	30/40	Rise, 30 ns
6	1.61	200	30/80	Rise, 30 ns
7	1.71	100	30/38	Rise, >30 ns
8	1.71	200	30/38	Rise, 30 ns

reaction zone can be easily explained within the framework of known theoretical approaches allowing for the width of the detonation wave front [6–8]. In this case, a dimensionless number L appears in the problem. This number characterizes the ratio of the front viscous width to the characteristic length of the reaction zone. At small L, the steady-state detonation regime takes place, which does not differ qualitatively from the classical case. The corresponding phase trajectory in the pressure-specific volume plane is shown in Fig. 3: only the amplitude of the von Neumann spike decreases and part of the explosive proves to have been reacted in the front of the compression wave. However, there exists a critical value L_c such that if $L > L_c$ then a qualitative change in the detonation front occurs: the final state on the detonation adiabat is attained as a result of a monotonic pressure rise (Fig. 3). In the general case, the uncompressed regime is realized and the detonation velocity is determined by kinetics of the chemical reaction, not by thermodynamics and gas dynamics alone, as is the case in classical detonation theory.

REFERENCES

1. Ya. B. Zel'dovich, Zh. Éksp. Teor. Fiz. **10**, 542 (1940).
2. V. K. Ashaev, G. S. Doronin, and A. D. Levin, Fiz. Goreniya Vzryva, No. 1, 95 (1988).
3. *Power Condensed Systems. Concise Encyclopedia,* Ed. by B. P. Zhukov (Yanus-K, Moscow, 1999).
4. D. Price, Chem. Rev. **59**, 801 (1959).
5. M. I. Belovolov, V. I. Vovchenko, G. I. Kanel', *et al.*, Zh. Tekh. Fiz. **57**, 918 (1987) [Sov. Phys. Tech. Phys. **32**, 557 (1987)].
6. J. O. Hirshfelder and C. F. Curtiss, J. Chem. Phys. **28**, 1130 (1958).
7. I. V. Zverev and N. N. Smirnov, *Gas Dynamics of Combustion* (Mosk. Gos. Univ., Moscow, 1987).
8. W. Fickett, *Introduction to Detonation Theory* (Univ. of California Press, Berkeley, 1985; Mir, Moscow, 1989).

Translated by V. Devitsyn

=== **PHYSICS** ===

Optical and Electrical Properties of the InAs/GaAs Modulation-Doped Superlattices for InAs-Layer Thicknesses below and near the Quantum-Dot-Formation Threshold

Corresponding Member of the RAS V. G. Mokerov, Yu. V. Fedorov, A. V. Guk, Kh. S. Pak, Yu. V. Khabarov, and A. V. Danilochkin

In recent years, great interest has been allotted to investigating self-organized ensembles of quantum dots, i.e., the quasi-zero-dimensional objects (with sizes of ~10–20 nm) formed in the process of heteroepitaxial growth. These objects arise in the case where there is a mismatch between parameters of a crystal lattice and substrate [1–6] by the Stranski–Krastanov mechanism [7]. According to this mechanism, for a certain critical thickness, a system can execute a phase transition from the two-dimensional layer-by-layer growth to the formation of three-dimensional coherent islands, i.e., the quantum dots on the surface of a thin wetting layer. To date, a wide set of investigations have been carried out to study the mechanisms of nucleation and formation of quantum dots (qd), their morphology, and their structural properties [1–5]. The optical properties of quantum dots are being investigated [6] with particular intensity. As was shown by the authors of [6], the photoluminescence method makes it possible to fix the appearance of quantum dots and to study their properties using the occurrence of a supplementary long-wave band in the photoluminescence spectrum. Interesting results have also been obtained for developing quantum-dot injection heterolasers [8, 9].

At the same time, it should be noted that the majority of the data cited in publications refers to undoped heterostructures in which the quantum dots are not populated by electrons, whereas the optical and electrical properties of doped structures containing quantum dots are mentioned to a much lesser extent.

The goal of this paper is to study the above-mentioned problem by investigating the optical and electrical properties of modulation-doped superlattices of InAs/GaAs with layer thicknesses below and near the quantum-dot formation threshold.

We used modulation-doped heterostructures grown by molecular-beam epitaxy on GaAs (001) semi-insu-lating substrates as the samples under investigation. These structures involve a GaAs undoped buffer layer, an InAs/GaAs superlattice, an $Al_{0.2}Ga_{0.8}As$ undoped spacer layer, an $Al_{0.2}Ga_{0.8}As$ doped layer, and a GaAs thin protective layer (Fig. 1). In the investigated series of the samples, the effective thickness d_{In} of the InAs layers varied from 0.33 to 2.7 monolayers (Fig. 1). In this case, the thickness of the GaAs layer was varied proportionally in order to retain an average composition of the superlattice equivalent to that of the $In_{0.16}Ga_{0.84}As$ solid solution. The number of superlattice periods was regulated, so that the superlattice attained a total thickness of approximately 14 nm. The thicknesses of the InAs and GaAs components of the superlattice in various samples, and also the number of superlattice periods in each of these samples, are indicated in the caption to Fig. 1. All the superlattices were grown at a temperature $T_s = 490°C$, while the remaining layers were grown at $T_s = 590°C$. The growth proceeded at a pressure of 8×10^{-6} torr in an ambient arsenic. After depositing each InAs layer, the growth was interrupted for 30 s. For comparison, a heterostructure was also grown in which an $In_{0.16}Ga_{0.84}As$ solid solution of the same thickness was formed instead of the InAs/GaAs superlattice mentioned previously.

The optical and electrical properties of the grown heterostructures were investigated by measuring the photoluminescence spectra at $T = 77$ K and by determining the mobility μ_{2D} and the electron concentration n_{2D} at $T = 77$ and 300 K on the basis of the Hall method.

In Fig. 2, we show the photoluminescence spectra for a sample of the $In_{0.16}Ga_{0.84}As$ solid solution (Fig. 2a) and for seven superlattice samples (Figs. 2b–2h). In the table, the results of the Hall measurements for μ_{2D} and n_{2D} are given. For comparison, in Fig. 2b (curve *2*), we also show the photoluminescence spectrum of the superlattice with undoped AlGaAs.

It follows from the table that all the samples have comparable electron concentrations $n_{2D} \simeq (6–10) \times 10^{11}$ cm^{-2}. However, the mobilities μ_{2D} of the electrons in the samples are substantially different, changing

Institute of Radio Engineering and Electronics,
Russian Academy of Sciences, ul. Mokhovaya 18,
Moscow, 103907 Russia

GaAs	n^+	6 nm	$T_s = 590\,°C$
$Al_{0.2}Ga_{0.8}As$		35 nm	$T_s = 590\,°C$

δ-Si, 5×10^{12} cm^{-2}

$Al_{0.2}Ga_{0.8}As$		10 nm	$T_s = 590\,°C$
GaAs	d_{Ga}		$T_s = 490\,°C$
InAs	d_{In}		$T_s = 490\,°C$

Superlattice, N periods

GaAs	d_{Ga}		$T_s = 490\,°C$
InAs	d_{In}		$T_s = 490\,°C$
GaAs	1-μm buffer		$T_s = 590\,°C$
GaAs	Substrate (001)		

Fig. 1. Cross section for the AlGaAs/InAs(n_2 monolayer)/GaAs(n_1MC)/GaAs(n_1 monolayer)/GaAs modulation-doped superlattices. d_{Ga} is the GaAs-layer thickness, d_{In} is the InAs-layer thickness in each superlattice period, and N is the number of periods in the superlattice.

from sample to sample within the range 6326–32896 cm^2/(V s).

As can be seen from Fig. 2, the photoluminescence spectra for the modulation-doped solid solution (Fig. 2a) and for six modulation-doped superlattices with monolayer thicknesses $d_{In} < 2$ (Figs. 2b–2g) have a similar shape and are disposed in the same spectral region. In these samples, we observed two peaks in the

photoluminescence: the low-energy peak of energy $h\nu_1$ (within the range 1.356 to 1.375 eV) and intensity I_1 and the high-energy peak of energy $h\nu_2$ (within the range 1.406 to 1.434 eV) and intensity I_2, so that $I_1 > I_2$ in all cases.

However, when the thickness of the InAs layer attains 2.7 monolayers, a radical transformation in the photoluminescence spectrum shape takes place. In the

Results of the Hall measurements for the mobility μ_{2D} and the concentration n_{2D} of two-dimensional electrons in the modulation-doped samples of the $In_{0.16}Ga_{0.84}As$ homogeneous solid solution and the InAs/GaAs superlattices at $T = 77$ and 300 K

Sample number	d_{In} (in units of the monolayer thickness)	μ_{2D}, cm^2/(V s) (77 K)	n_{2D}, 10^{11} cm^{-2} (77 K)	μ_{2D}, cm^2/(V s) (300 K)	n_{2D}, 10^{11} cm^{-2} (300 K)
1172	Homogeneous solid solution	17670	9	6000	9.6
1178	0.33	32896	10.3	7747	9.96
1171	0.67	6620	8.5	2830	9.6
1169	1.0	8560	6.46	4164	6.2
1181	1.33	10696	8.63	5436	9.64
1170	1.58	6610	6.6	3480	6.6
1206	2.0	20900	9.85	5370	8.2
1179	2.7	6326	7.86	4059	7.42

long-wave spectral region, a new broad and intense band arises with its peak at $h\nu_{qd} = 1.265$ eV (Fig. 2h). As was shown in [6], such modifications of the spectrum are associated with the phase transition from the two-dimensional layer-by-layer growth mode to that of the three-dimensional growth mode corresponding to the formation of quantum dots.

In this connection, it is reasonable to consider separately the characteristics of a modulation-doped superlattice of InAs layers with thicknesses $d_{In} < 2.0$ monolayers, for which the two-dimensional layer-by-layer growth is presumed to be realized, and the characteristics of the modulation-doped superlattice with $d_{In} = 2.7$ monolayers, where the growth mode corresponding to the formation of InAs quantum dots in the GaAs matrix is realized.

1. The photoluminescence spectra and electron mobility in a modulation-doped superlattice with thicknesses of InAs layers lower than 2.0 monolayers (below the quantum-dot formation threshold). In order to interpret the optical properties of the modulation-doped superlattice with $d_{In} < 2.0$ monolayers, we base our assumptions on the fact that the presence of two peaks in the photoluminescence spectra of the N–AlGaAs/InAs/GaAs modulation-doped quantum well (i.e., the solid solution) is a consequence of the population of two subbands of the two-dimensional electron gas in the InGaAs quantum well [10, 11]. These peaks correspond to the optical transitions from the lower e_1 and upper e_2 subbands to the hole subbands. In the case of undoped (empty) quantum wells, we can observe only a single photoluminescence peak caused, as is well known, by optical transitions between the lowest (unfilled) electron and hole subbands (Fig. 2b, curve *2*). Based on the similarity between the photoluminescence spectra of a modulation-doped solid solution (Fig. 2a) and a modulation-doped superlattice (Figs. 2b–2g), we can assume that, in the latter case, the $h\nu_1$ and $h\nu_2$ peaks are of the same nature as those in the former. In other words, two electron subbands are also populated in this case and the energy range $h\Delta\nu_{12} = h\nu_2 - h\nu_1$ determines the energy gap between them. Thus, in spite of the difference in the "construction" of these two types of heterostructures (layered and homogeneous), their subband structures are similar. This fact is evidently caused by the strong overlapping of the wave functions of neighboring InAs layers in the superlattice owing to the efficient tunnel coupling through the GaAs barriers.

However, in spite of the general similarity between the photoluminescence spectra in Figs. 2a–2g, there are also certain distinctions between them. For example, the sharpest and most intense peaks are observed for the modulation-doped superlattice with $d_{In} = 0.33$ monolayers (Fig. 2b). It is of interest that the intensity and sharpness of the photoluminescence peaks drop abruptly when d_{In} merely increases to 0.67 monolayers (Fig. 2c). As can be seen from Figs. 2c–2g, such a situa-
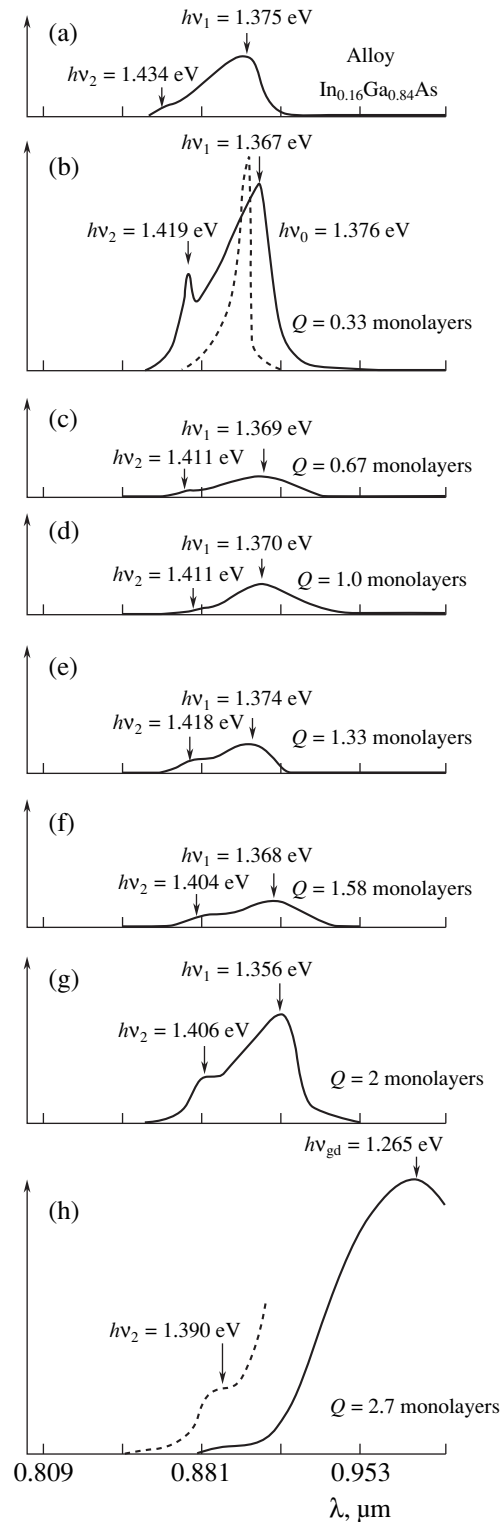
Fig. 2. Photoluminescence spectra for the AlGaAs/(InAs/GaAs)/GaAs modulation-doped superlattice and the $In_{0.16}Ga_{0.84}As$ modulation-doped homogeneous solid solution at a temperature $T = 77$ K: (a) spectrum of the homogeneous solid solution; (b)–(h) spectra of a modulation-doped superlattice with thickness d_{In} (in units of the monolayer thickness): (b) $d_{In} = 0.33$, $N = 24$; (c) $d_{In} = 0.67$, $N = 12$; (d) $d_{In} = 1$, $N = 8$; (e) $d_{In} = 1.33$, $N = 6$; (f) $d_{In} = 1.58$, $N = 5$; (g) $d_{In} = 2$, $N = 4$; and (h) $d_{In} = 2.7$, $N = 3$.
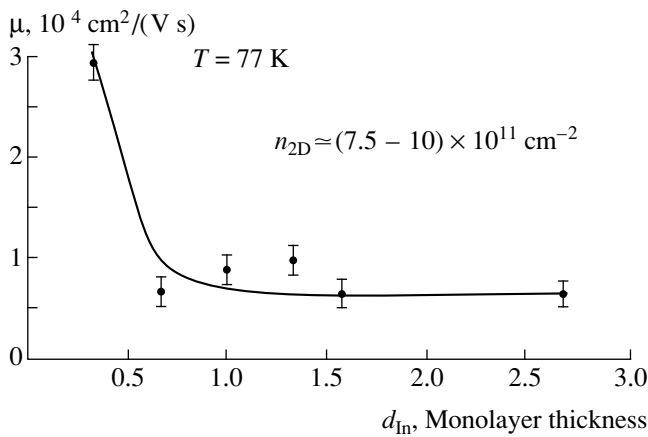
Fig. 3. Dependence of the electron mobility in the modulation-doped superlattices under investigation on the effective thickness of the InAs layer in the superlattice at $T = 77$ K.
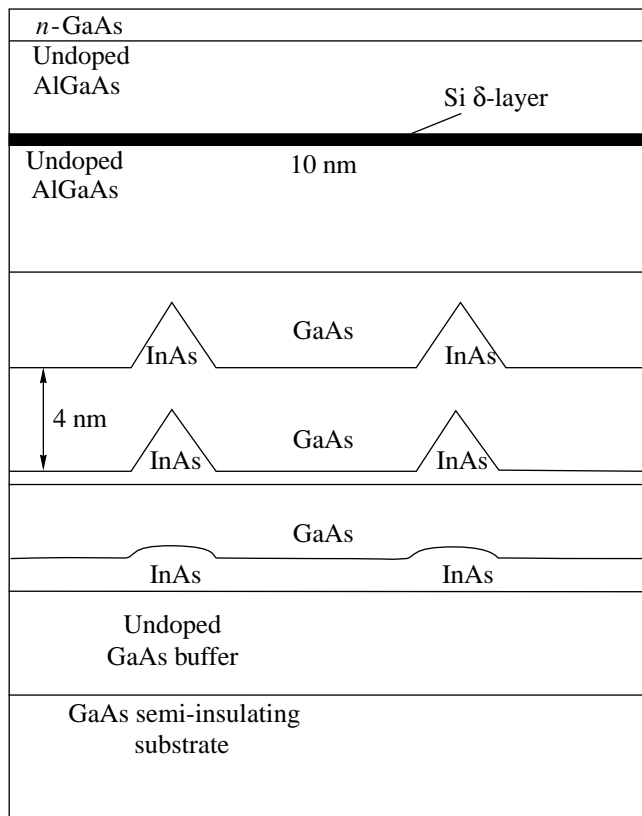
Fig. 4. Cross section of the assumed heterostructure with vertically coupled quantum dots.

tion is also retained for other samples having thicknesses of InAs layers within the range up to 1.58 monolayers. A certain increase in photoluminescence intensity manifests itself in the case of $d_{In} = 2.0$ monolayers (Fig. 2g). However, sharp peaks, such as in Fig. 2b, are not observed in this case. To clarify the reasons for the variations observed in the shape of the photoluminescence spectra when changing d_{In}, we analyze the dependence of the electron mobility μ_{2D} in the modulation-doped superlattice on the thickness d_{In} (see Fig. 3). It follows from Fig. 3 that (similarly to the dependence of the photoluminescence intensity on d_{In}) the highest mobility $\mu_{2D}^{max} = 32\ 896$ cm^2/(V s) is observed in the sample with $d_{In} = 0.33$ monolayers and, then, drops abruptly with increasing d_{In}. Already for $d_{In} = 0.67$ monolayers, the mobility becomes equal to 6620 cm^2/(V s). Furthermore, up to the value of $d_{In} = 1.58$ monolayers, the mobility varies insignificantly. Note that the superlattice sample No. 1206 ($d_{In} = 2.0$ monolayers), for which we observe elevated values for both the photoluminescence intensity and mobility μ_{2D}, was grown on the substrates made of the other ingot. For this reason, we do not accentuate the deviation exhibited in this sample from the regular characteristics exhibited in the others.

On the basis of the above-mentioned facts, we can assume the following. For a minimum submonolayer InAs covering ($d_{In} = 0.33$ monolayers), when the amplitude of the elastic-stress fluctuation is yet far from critical owing to the small thickness of deposited InAs, an almost ideal layer-by-layer growth takes place, thus forming the most perfect crystal lattice. In this lattice, in contrast to the situation in the solid solution, indium atoms are disposed in a certain order and the processes associated with electron scattering and radiationless recombination must be minimized. Therefore, we here observe the sharpest and most intense photoluminescence peaks and the maximum value for the electron mobility. At the same time, an increase in the InAs effective thickness must enhance the elastic stresses and their fluctuations, which results in fluctuations of the relief and the necessity of introducing additional mechanisms of electron scattering and radiationless recombination. We assume that the decrease in μ_{2D}, the reduction of the intensity, and the sharpness of the photoluminescence peaks in the case of increasing the thickness of the InAs covering are related to an additional scattering of charge carriers at the fluctuations of potential and to an increasing contribution of the radiationless recombination caused by the fluctuations of elastic stresses and the layer relief induced by them. Here, we deal with the unexpected fact that these effects take place even at a sufficiently small quantity of deposited InAs. Indeed, they are observed for a submonolayer covering ($d_{In} = 0.67$ monolayers), whereas the almost normal layer-by-layer growth is commonly assumed for this case in other publications.

2. The properties of a modulation-doped superlattice for thickness of InAs covering $d_{In} = 2.7$ monolayers (near the quantum-dot formation threshold). As was already noted, we ascribe the photoluminescence broad long-wave band at $h\nu = 1.265$ eV in the modulation-doped-superlattice sample with $d_{In} = 2.7$ monolayers to the appearance of quantum dots. We also relate the weak short-wave peak at $h\nu = 1.390$ eV to a

thin wetting layer. However, it is necessary to note that while investigating a similar heterostructure in which only one InAs layer with an effective thickness d_{In} = 2.7 monolayers was grown instead of the InAs/GaAs superlattice, no additional photoluminescence long-wave band testifying to the presence of quantum dots was found. It follows from this fact that, although no quantum dots are formed in the InAs lower layer of the modulation-doped superlattice, the elastic stresses arising from it stimulate quantum-dot nucleation in the subsequent layers of the superlattice. The assumed cross section of the modulation-doped superlattice with quantum dots investigated by us is shown in Fig. 4.

ACKNOWLEDGMENTS

REFERENCES

1. D. Leonard, K. Pond, and P. M. Petroff, Phys. Rev. B **50**, 11 687 (1994).

2. J. M. Moison, F. Houzay, F. Barthe, *et al.*, Appl. Phys. Lett. **64**, 196 (1994).

3. G. S. Solomon, J. A. Trezza, and J. S. Harris, Jr., Appl. Phys. Lett. **66**, 3161 (1995).

4. G. S. Solomon, J. A. Trezza, and J. S. Harris, Jr., Appl. Phys. Lett. **66**, 991 (1995).

5. P. D. Wang, N. N. Ledentsov, C. M. Sotomajor Torres, *et al.*, Appl. Phys. Lett. **64**, 1529 (1994).

6. N. N. Ledentsov, V. M. Ustinov, V. A. Shchukin, *et al.*, Fiz. Tekh. Poluprovodn. (St. Petersburg) **32**, 385 (1998) [Semiconductors **32**, 343 (1998)].

7. I. N. Stranski and L. Von Krastanov, Akad. Wiss. Let., Mainz, Abh. Math.-Naturwiss. Kl. **146** (1939).

8. J. A. Lott, N. N. Ledentson, V. M. Ustinov, *et al.*, Electron. Lett. **33**, 1150 (1997).

9. A. E. Zhukov, A. Yu. Egorov, A. R. Kovsh, *et al.*, Fiz. Tekh. Poluprovodn. (St. Petersburg) **31**, 483 (1997) [Semiconductors **31**, 411 (1997)].

10. Y. K. Yuan, K. Mohammed, M. A. A. Pudensi, *et al.*, Appl. Phys. Lett. **45**, 739 (1984).

11. A. V. Guk, V. É. Kaminskiĭ, V. G. Mokerov, *et al.*, Fiz. Tekh. Poluprovodn. (St. Petersburg) **31**, 1367 (1997) [Semiconductors **31**, 1178 (1997)].

Translated by V. Bukhanov

=========== **TECHNICAL PHYSICS** ===========

Relaxation Behavior of an Acoustic Elastic Modulus for SVM Fibers

S. L. Bazhenov, A. K. Rogozinskiĭ, and Corresponding Member of the RAS A. A. Berlin

Received February 15, 2000

Under tension, polymers often demonstrate creep, i.e., gradual elongation with time. This creep is caused by inelastic processes occurring in the material. For a constant sample length, these processes manifest themselves as a gradual decrease in stretching force. In this case, we say that the sample is tested in the regime of relaxing (i.e., decreasing) stress. If the stretching force is constant and the sample length increases, then the tests occur in the creep regime. Relaxation behavior is quite intrinsic to aramid SVM fibers (SVM is a trademark).

A characteristic feature of SVM fibers is an increase in the elastic modulus with deformation [1]. The elasticity modulus rises rather noticeably from the initial value of 110 to 120 GPa to approximately 200 to 210 GPa at a strain of 3%. An increase in the elastic modulus is observed in the case of both tension with a constant rate and creep under a constant load [2, 3]. The rise of the elastic modulus is reversible and gradually decreases to the initial value after unloading. This reversibility testifies to the fact that the rise of the modulus does not depend on the orientation irreversible at temperatures much lower than the glass-transition temperature T_g [4].

There are several explanations for the rise of the elastic modulus of polymers with strain. For example, this effect can be associated with the nonlinear elasticity of fibers [5]. However, since elastic processes proceed instantaneously, nonlinear elasticity cannot explain the gradual rise of the modulus in the presence of creep. Therefore, a theoretical model was proposed according to which the polymer chain contains defects having a lowered rigidity. The rise of the modulus in the case of creep is explained by the transition of defect fragments in a polymer chain in the more rigid straightened state [3, 4, 6]. This transition has an activation barrier, and it takes time to overcome it. The goal of the present study is to investigate the behavior of the elastic modulus of SVM fibers in the case of different methods of loading.

Institute of Chemical Physics,
Russian Academy of Sciences, Vorob'evskoe sh.,
Moscow, 117312 Russia

We have investigated samples of SVM threads with a linear density of 58 tex, which consisted of 300 elementary fibers with a diameter close to 13 microns. The length of the samples was 600 to 800 mm. The samples had cone-shaped ends at both the input and the output of the sonic signal.

We studied stress relaxation and fiber creep using various experimental equipment. Stress relaxation was investigated with the help of an Instron 1122 universal testing machine, whereas creep was investigated by means of nonstandard equipment. The upper end of the thread was immobile, whereas a certain load was attached to the lower mobile end, and the sample elongation was measured. In both cases, longitudinal ultrasound pulses with a frequency of 250 kHz and a repetition frequency of 0.9 kHz were passed through the sample. The elastic modulus E was determined according to the speed c of the ultrasound [7]:

$$E = \rho c^2, \tag{1}$$

where ρ is the fiber density. The speed of the ultrasound was determined as the ratio of the sample length to the time of pulse passage.

Before loading, the fibers were dried for 20 min at 110°C. Then, they were trained by loading up to a 2-GPa stress and annealed at a temperature of 150°C over 1.5 hours. The sample length increased after training by approximately 0.5%, and the elastic modulus grew from 120 to 125–128 GPa. For subsequent loading/unloading cycles, we observed no irreversible changes in either the strain or the elastic modulus. Thus, training made it possible to exclude inelastic effects.

1. Creep. Figure 1 shows strain of SVM fibers as a function of time in the presence of creep under a stress of 1.6 GPa. As is seen, the fiber length gradually increases with time, while the creep velocity decreases. Curve *2* shows that the fiber elastic modulus E rises simultaneously with an increase in the fiber length. Curves *1* and *2* are similar in shape. This fact indicates the unambiguous connection between the length and the elastic modulus of the fibers.

2. Stress relaxation. Figure 2 illustrates the behavior of the thread after it had been stretched to the stress of 1.6 GPa and in then the clamps of the tensile testing

machine were stopped. For 25 min, the stretching stress corresponding to curve *1* dropped by approximately 15%. In contrast to the stress, the elastic modulus gradually increased (see curve *2*). It is worth mentioning that this unusual behavior of the elastic modulus at a fixed sample length was observed, in this case, for the first time.

3. Recovery. Figure 3 illustrates the dependence of the elastic modulus on the fiber strain ε for different loading schemes. Crosses show the behavior of fibers after a sharp reduction in the load. The thread crept under a stress of 2.25 GPa over 1.5 hours, after which the stress decreased to 0.45 GPa. After reducing the load, the behavior of the thread became unusual. The thread length gradually decreased, and the 1.8-kg piece hanging on the thread rose. Apparently, the internal energy is stored in the fibers in the case of creep under loading. This energy performs the work of lifting the weight after a sharp reduction in the load. The gradual decrease in the elastic modulus (1) occurs simultaneously with the reduction of the thread length. The direction of the process with time is indicated in Fig. 3 by the arrow.

The experimental dots in curve *2* of Fig. 3 are obtained according to a similar loading scheme. This distinction from curve *1* consists in the fact that, before reducing the load to 0.45 GPa, the thread crept for a shorter duration time under a stress of 2.25 GPa. In this experimental run, we varied the creep time under the stress of 2.25 GPa. Figure 3 illustrates the behavior of the thread in the case of the usual creep corresponding to the case of Fig. 1 (the thread was not kept under the large stress). The direction of the process in the case of creep is opposite to that observed after a strong decrease in loading. The dependence of the modulus on the fiber length in all three cases is described by a unified curve. Thus, there exists an unambiguous connection between the fiber length and the elastic modulus, which is independent of the loading prehistory. Note that this statement is true only in the case of the same stretching load.

4. The relaxation at the constant length. The loading scheme corresponded to curve *1* in Fig. 3; however, both thread ends were fixed after the decrease in the load. Figure 4 illustrates the change in the stretching stress (curve *1*) and the acoustic modulus (curve *2*) for fibers observed after the load had been decreased. In this case, we observed a gradual elevation of the stress with time. After 15 min, the stress increased from 270 to 310 MPa. The rise of the elastic modulus was observed simultaneously with the above-mentioned increase in stress. Evidently, the increase in stress is associated with the constant fiber length.

The behavior of the fibers can be explained assuming the existence of defects in the molecular-chain structure. We can consider the structure of these defects to be similar to a loop. Under loading, these defects (loops) straighten; therefore, the rigidity of the polymer
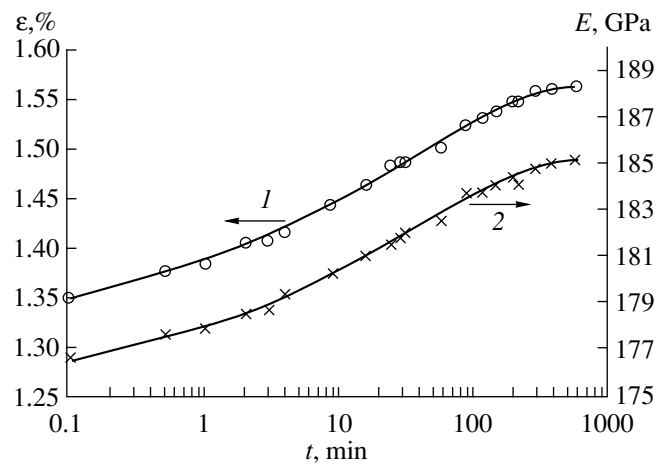
Fig. 1. Behavior of fibers in the case of creep under a stress of 1.6 GPa: (*1*) fiber strain ε; (*2*) acoustic elastic modulus E.
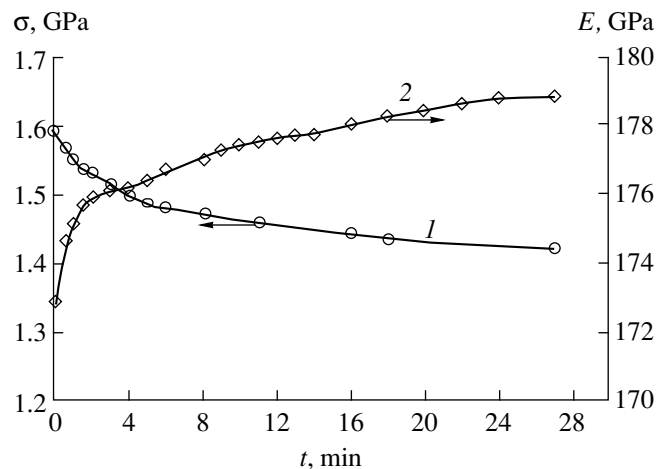
Fig. 2. Behavior of fibers in the regime of stress relaxation in the case of immobile clamps of a tensile testing machine: (*1*) stretching stress σ; (*2*) acoustic elastic modulus E.
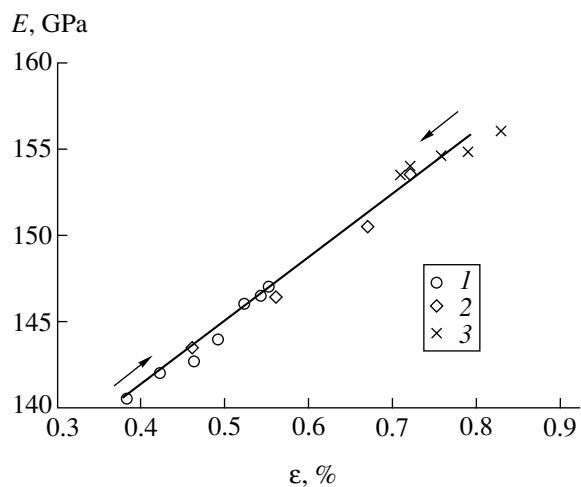
Fig. 3. Correlation between the elastic modulus E and strain ε for different methods of loading.
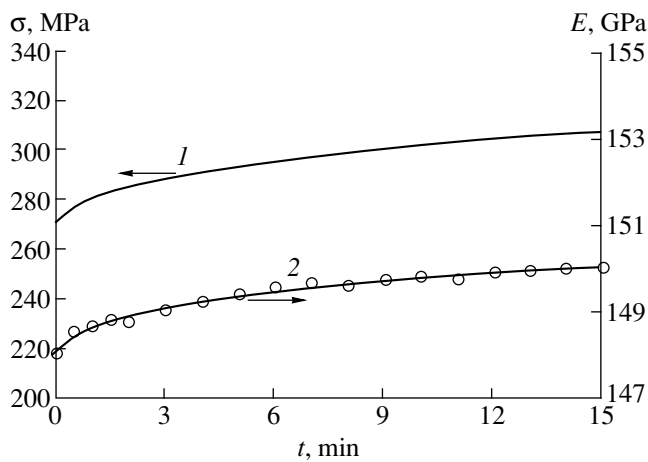
Fig. 4. Behavior of fibers after the load has been decreased from 1.6 to 0.27 GPa. The fiber length was constant: (*1*) stress σ; (*2*) acoustic elastic modulus.

chain is enhanced. The transition has an activation barrier, which takes time to overcome. Figure 3 testifies to the reversibility of the transition. Apparently, there is a certain equilibrium concentration of defects dependent on the stress and temperature. An increase in load stimulates the straightening of the defects. Conversely, a decrease in load stimulates reverse transitions and the elastic modulus reduces. The gradual rise of stress after the load has been decreased (with immobile testing-machine clamps) is also explained by the reversibility of the transitions, namely, by the increase in the concentration of short and soft defects.

In spite of the increase in the concentration of soft defects after the reduction of the load, Fig. 4 demonstrates a rise of the elastic modulus. This fact proves that, apart from the transitions, there exists a second mechanism governing the change in the modulus. This mechanism consists in the nonlinear elasticity of the fibers [3, 5]. It is worth noting that the result of the combined action of the two mechanisms (i.e., the variation of the defect concentration and the existence of the nonlinear elasticity) depends on the loading scheme:

(i) In the case of creep, the stress is constant and the effect of nonlinear elasticity is not manifested. Therefore, the change in the modulus is determined only by transitions into a more rigid state. This explains the rise of the elastic modulus and fiber length with time.

(ii) After a sharp decrease in the load, reverse transitions are initiated and the defect concentration is elevated. If the load is constant, then the elastic modulus and fiber length gradually decrease.

(iii) In the stress relaxation regime, the mechanisms of nonlinear elasticity and the transitions act in opposite directions. A decrease in stress results in the lowering of the elastic modulus due to nonlinear elasticity. Contrarily, a decrease in the concentration of soft

defects elevates the elastic modulus of a polymer. Since the combined action of these effects leads to an increase in the elastic modulus (see Fig. 2), the transitions of the defects into the rigid state prevail over the nonlinear elasticity.

(iv) After a decrease in load at a fixed sample length, the stress and elastic modulus increase simultaneously. As in the preceding item, the nonlinear elasticity and molecular transitions act in opposite directions. The gradual rise in stress results in an increase in the fiber modulus due to nonlinear elasticity. The increase in the concentration of soft defects leads to a drop in elastic modulus. The combined result consists in the rise of the elastic modulus. In contrast to the preceding item, the effect of the nonlinear elasticity in this case is stronger than that of the relaxation transitions.

Relaxation phenomena in polymers are usually described by various models similar to the Maxwell classical model. This model is composed of a sequentially connected spring and a damper, which makes it possible to describe both the elasticity and relaxation behavior of a polymer [8]. Owing to the existence of a spectrum of relaxation times, more complicated models composed of a set of springs and dampers are also used. In the most general mathematical form, these models can be described by the Volterra integral equation. Nevertheless, even this equation is not capable of describing the increase in the stress or elastic modulus with time. As a consequence, the kernel of this equation must be significantly modified in order to involve functions ascending with time. Thus, after a decrease in load, the relaxation of the polymer fibers can manifest itself in a paradoxical manner as an increase in both stress and elastic modulus.

REFERENCES

1. A. M. Stalevich and L. E. Poot, Khim. Volokna, No. 6, 36 (1980).
2. A. K. Rogozinskiĭ, S. L. Bazhenov, and É. S. Zelenskiĭ, Vysokomol. Soedin., Ser. B **32**, 437 (1990).
3. A. K. Rogozinsky and S. L. Bazhenov, Polymer **33**, 1391 (1992).
4. É. F. Oleĭnik, O. B. Salamatina, S. N. Rudnev, and S. V. Shenogin, Vysokomol. Soedin., Ser. A **35**, 1819 (1993).
5. M. I. Bessonov and A. P. Rudakov, Vysokomol. Soedin., Ser. B **13**, 542 (1971).
6. A. I. Slutsker and O. Mirzoev, Vysokomol. Soedin., Ser. A **40**, 828 (1998).
7. L. D. Landau and E. M. Lifshitz, *Course of Theoretical Physics*, Vol. 7: *Theory of Elasticity* (Nauka, Moscow, 1982; Pergamon, New York, 1986).
8. G. L. Slonimskiĭ, in *Encyclopedia of Polymers* (Moscow, 1977), Vol. 3.

Translated by G. Merzon

═══════════════════ **TECHNICAL PHYSICS** ═══════════════════

Highly Ionized Turbulent Lithium Plasma

A. V. Nedospasov*, E. V. Mudretskaya*, and A. V. Zhmendak**

Presented by Academician V.E. Fortov December 21, 1999

The generation of low-temperature highly ionized plasma in heavy-current electrode discharges is usually associated with discharges in hydrogen. In other gases, the attainment of the necessary electron temperature is hampered by the energy loss of plasma through its radiation. A new possibility for the study of virtually completely ionized plasma in lithium vapors was indicated and realized in [1, 2]. The properties intrinsic to lithium were used, e.g., the low ionization energy of lithium atoms and the extremely high excitation and ionization energies of Li^+ helium-like ions. Plasma with a density of 10^{15}–10^{16} cm^{-3} and an electron temperature $T_e = 2$–3 eV, which exhibited almost complete ionization of lithium atoms, was obtained. Moreover, the energy loss for ionization and radiation in the plasma were relatively low.

In this case and under steady-state conditions, the energy balance for electrons can be written out in a well known form [3]:

$$\frac{2e^2 n \tau_e}{m_e} E^2 = -\frac{1}{r}\frac{\partial}{\partial r}\left(3.16\frac{n T_e \tau_e}{m_e} r \frac{\partial T_e}{\partial r}\right) + \frac{3m_e}{m_i}\frac{n}{\tau_e}(T_e - T_i). \tag{1}$$

For preliminary estimates, we take $n_e = 10^{15}$ cm^{-3} and $T_e = 3$ eV. The time scale of the electron–ion energy exchange for these parameters is approximately 3×10^{-6} s. Consequently, in discharges with a duration longer than 10^{-4} s, electron and ion temperatures are almost equal and the Joule heat is predominantly transferred outward, i.e., to the tube walls, owing to the electron thermal conductivity. Near the walls, this heat is spent to the new ionization of atoms produced in the process of recombination and for the compensation of other energy loss on the walls. The energy balance is independent of the plasma density. In the case of a high degree of ionization, the plasma concentration enters only into the boundary conditions. A rough estimate of the term $d/dr \approx 1/a$ in equation (1) yields the following expression for the electric field in a tube with radius a:

$$\frac{eEa}{T_0} \approx 1, \tag{2}$$

where T_0 is the temperature at the axis. From the Spitzer formula for the conductivity of a completely ionized plasma, the density of the maintaining current turns out to be on the order of several hundred A/m^2. It is also possible to obtain the dependence of the resistance of the discharge column on the current intensity:

$$R = C\frac{l}{a^2}\left(\frac{I}{a}\right)^{-3/5}. \tag{3}$$

Here, l is the column length and C is a certain factor on the order of 1.

In this study, we describe a new experimental setup (called Robotron) developed in the Kiev scientific-industrial company Eleĭ-2 and the first results obtained with the help of this setup.

Experimental setup. The principle structure of the experimental setup and the diagram of its electric-power supply are shown in Fig. 1. The discharges are initiated in a well evacuated quartz tube with an inner diameter of 25 mm. Two cathodes are placed at the tube ends. One of these is the cathode of the basic discharge. This cathode has the shape of a hollow cylinder rounded at its edge. The surface of the other cathode is made of lithium deposited on a vanadium substrate and serves for the injection of the lithium plasma into the tube. The tubular anodes are arranged near the lithium injector. All the electrodes are made of vanadium.

Both cathodes are supplied with special auxiliary electrodes initiating the appearance of cathode spots in the case of feeding the electrodes by a high-voltage pulse with a duration of several microseconds. The cathode spots arising under the action of this pulse give rise to a heavy-current stage of discharges. The discharge in the lithium injector is excited first. The onset of the basic discharge along the entire tube is controlled by a delay within several hundred microseconds.

The discharge device shown in Fig. 1 was placed into an evacuated quartz tube 120 mm in diameter. Two

─────────────

* *Institute of High Temperatures Scientific Association*
  (IVTAN), Russian Academy of Sciences,
  Izhorskaya ul. 13/19, Moscow, 127412 Russia
** *NPO Eleĭ-2, ul. Lyuteranskaya 25,*
  Kiev, 252024 Ukraine
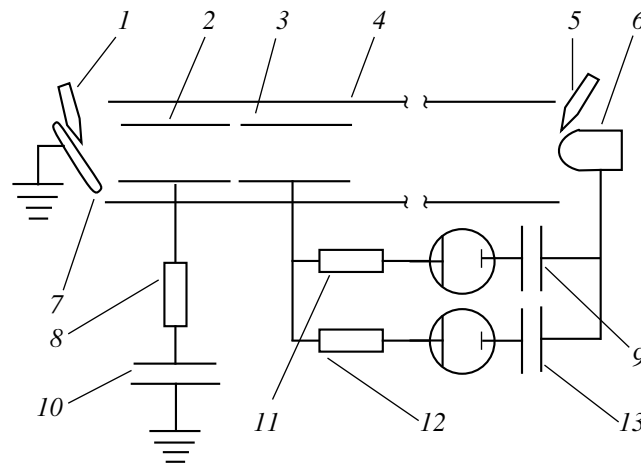
Fig. 1. Discharge tube and its electric power-supply circuit: (*1*) ignition of the lithium-plasma source; (*2*) anode of the lithium-plasma source; (*3*) the basic-discharge anode; (*4*) quartz tube; (*5*) ignition of the basic discharge; (*6*) the basic-discharge cathode; (*7*) cathode of the lithium plasma source; (*8*) ballast resistor of the lithium-plasma source; (*9*) capacitor banks of the first-discharge source; (*10*) capacitor banks of the lithium-plasma source; (*11*) and (*12*) ballast resistors; (*13*) capacitor banks of the second-discharge source.

banks of capacitors feeding the basic discharge had independent switching-in with a controllable delay. The highest energy of both discharge banks was 2.4 kJ. Fine tuning of voltages and ballast resistors made it possible to vary the parameters of both the basic discharge and the lithium plasma injection within wide limits.

A specific feature of the discharges is the absence in them of a constant concentration of lithium atoms. The plasma pressure in the discharge is much higher than the pressure of saturated lithium vapors at the wall temperature. The current intensity is measured by the Rogowski loops. The difference of potentials across the electrodes is measured according to the current through the resistor, with the galvanic decoupling realized by means of an optical pair consisting of a photodiode and light-emitting diode. The information is recorded by an analog-to-digital converter with a maximum readout frequency of 500 kHz. While simultaneously recording several channels, the readout time increases correspondingly.

In Fig. 2, the initial stage of discharges is shown as an example. The basic current arises with a delay of 300 μs from the onset of lithium plasma injection. Usually, strong oscillations of the voltage across the discharge appear. In similar discharges in argon, no marked oscillations were observed. The spectral analysis of the discharges shows the presence of lines of atomic and ionized lithium, the spectrum of atomic vanadium, and the lines of the Balmer series in hydrogen.

Current–voltage characteristics. The spectrum of strong oscillations of the voltage lies within the range (up to the frequency of 250 kHz) accessible for detection. The autocorrelation function for these oscillations has a narrow peak with a width corresponding to a min-

imum recording time of 2.5 μs. As a rule, the voltage recording frequency had a period of 12.5 μs. Furthermore, such a signal was averaged over five points. In the case of the determination of the current–voltage characteristic for the discharge column in itself, we subtracted the sum of the near-electrode voltage drops, which was taken to be equal to 30 V from the measured voltage.

The experiments showed that, after the basic discharge had been ignited and the stage of the quasi-steady mode in the presence of strong oscillations had been established, the discharge resistance increases with decreasing the current to $I \approx 100$ A in accordance with formula (3). Furthermore, the resistance rises abruptly owing to the onset of the recombination.
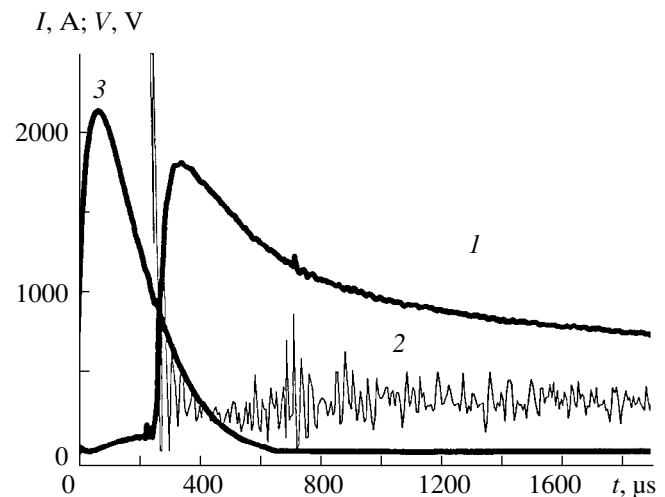
Fig. 2. Time dependence of the discharge characteristics: (*1*) discharge current intensity; (*2*) voltage drop across the discharge; (*3*) electric-current intensity in the lithium-plasma source.

In Fig. 3, we show that the discharge resistance is proportional to the power law of the current intensity with the exponent of –3/5, which is typical of turbulent discharge. A similar dependence also existed in discharges described in [1] characterized by the discharge tube radius $a = 0.8$ cm. Such a power law has a high reproducibility with a spread not exceeding 10%. The slope of the straight line in Fig. 3 corresponds to the relation $eEa/T_0 = 1.43$ in formula (2). The suppression of the voltage oscillations across the discharge decreases the discharge resistance by several times and makes its current dependence more complicated than that in Fig. 3.

On the nature of the turbulence observed. At a glance, it is unclear why it is the strong turbulence that agrees well with estimate (2) taking into account only the electron thermal conductivity in the energy balance. We can suggest the following explanation for this fact. The turbulence increases the radial transport in the plasma. In this case, the radiation intensity for the atomic-lithium line increases abruptly near the walls. The plasma concentration near the walls is maintained by the new ionization of plasma recombined at the wall, while the necessary energy is delivered by the electron thermal conductivity. Thus, the turbulence requires the increase in the radial heat flux.

A priori, the most probable reason for the turbulence observed is the current-convective kink instability (see, for example, reviews [3, 4]). Borrowing the criterion for initiation of screw instability in arc discharges at atmospheric pressure from [4] and using the transport coefficients from [5], we obtain the relationship

$$\mathrm{Ra} \simeq 60 \frac{\tau_e}{\tau_i} \left(\frac{eEa}{T_0} \right)^2 r_e a^2 n, \qquad (4)$$

where $r_e = e^2/m_e c^2$ is the electron classical radius; τ_e^{-1} and τ_i^{-1} are the collision frequencies for electrons and ions, respectively; and n is the plasma concentration. According to (4), convection arises for $n_e > 2 \times 10^{15}$ cm^{-3}.

This criterion corresponds to the conditions where the perturbation for all the quantities at the walls can be ignored. In our case, these rigorous boundary conditions are not fulfilled. Therefore, instability must arise for lower concentrations. We can assume that the voltage oscillations across the tube are induced by the formation and breakup of the screw form of the discharge and by a change in its internal inductance. The reason for the breakup of the screw form can be a deficiency in the radial heat flux for an extra-large injection of plasma onto the walls. As was noted in [2], the thermal conductivity is able to remove only a limited quantity of heat, which corresponds to the condition $Ea/T_0 \leq 1.43$. The straight line in Fig. 3 shows that the resistance of the turbulent discharge is restricted by this value.
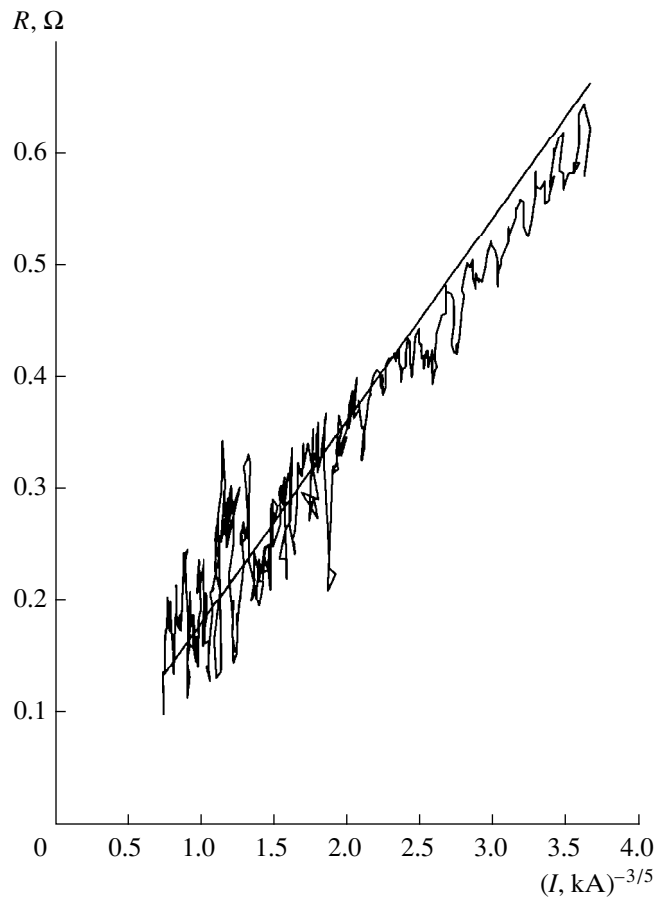
Fig. 3. Dependence of the discharge resistance R on the current intensity ($I^{-3/5}$). The straight line corresponds to the ratio $eEa/T_0 = 1.43$.

The measurement results for the longitudinal magnetic field outside of the discharge tube became a direct confirmation of the appearance of the screw form of the discharge. The longitudinal magnetic-field component H_z was measured by a Hall probe installed at a distance of 6.5 cm from the tube axis near its middle section. The measurements allowed us to detect oscillations of the H_z-component which are associated with those of the discharge current I. The amplitude of the H_z-component attained several Oersteds. Thus, the oscillations of the longitudinal magnetic field in the discharge were on the order of hundreds of Oersteds. This value for the current of ~1 kA does not contradict the estimate of a possible screw pitch $\lambda \simeq \pi a$ [4]. The average value of H_z decreases with time proportionally to the discharge current that confirms the origin of this component. The oscillations of the H_z-component correlate with those of the voltage across the discharge.

REFERENCES

1. A. V. Nedospasov, G. V. Sergienko, N. M. Zykova, *et al.*, J. Nucl. Mater. **266–269**, 618 (1999).

2. E. V. Mudretskaya, A. V. Nedospasov, S. A. Perevoznikov, and A. V. Zhmendak, in *Proceedings of XXIV ICPIG* (Warsaw, 1999, Vol. 4), p. 49.

3. A. V. Nedospasov, Usp. Fiz. Nauk **116**, 643 (1975) [Sov. Phys. Usp. **18**, 588 (1975)].

4. A. V. Nedospasov and V. D. Khait, *Principles of Physical Processes in Low-Temperature Plasma Devices* (Énergoatomizdat, Moscow, 1991).

5. S. I. Braginskiĭ, in *Reviews of Plasma Physics*, Ed. by M. A. Leontovich (Gosatomizdat, Moscow, 1963; Consultants Bureau, New York, 1963), Vol. 1, p. 183.

Translated by V. Bukhanov

===== **TECHNICAL PHYSICS** =====

Solid Solution Domains in Equilibrium Phase Diagrams: Our Concepts and Reality

Yu. I. Ustinovshchikov

Presented by Academician O.A. Bannykh January 13, 2000

Received January 19, 2000

According to the model of interatomic pair interaction, there are two possible types of interaction between components of binary metallic substitutional alloys: the attraction between the A and B atoms, resulting eventually in the formation of chemical compound A_mB_n (the mixing energy $E_{mix} = u_{AA} + u_{AB} - 2u_{AB}$ is negative), and the repulsion between A and B atoms, giving rise to a mixture of crystals formed by pure components (the mixing energy is positive). In thermodynamics, these two types of interatomic interactions are related to the tendency of a system to ordering (the sign of deviations from the Raoult law is negative) and to phase separation (the sign of deviations is positive), respectively. These two types of interatomic interactions correspond to two basic types of equilibrium phase diagrams: for the case $E_{mix} < 0$, the phase diagrams consist of the regions where chemical compounds are formed; for the case $E_{mix} > 0$, the phase diagrams consist of the regions corresponding to the mechanical mixture of crystals formed by components of the alloy.

However, there exists a large number of equilibrium phase diagrams involving domains (bounded and unbounded) in which, as expected, solid solutions are formed. The presence of the solid solution domains in the phase diagrams means that these solid solutions are equilibrium phases. If the solid solution is an equilibrium phase at temperatures for which the diffusion of components is sufficient for its decomposition, it is possible to say that such a solid solution is ideal. Such a conclusion is in striking contrast with thermodynamic data which suggest that the overwhelming majority of solid solutions are nonideal and exhibit either positive or negative deviations from the Raoult law. As a consequence, they demonstrate the tendency either to phase separation or to ordering, which should certainly lead to the decomposition of the solid solution when the system approaches equilibrium.

Physicotechnical Institute, Ural Division,
Russian Academy of Sciences, ul. Kirova 132,
Izhevsk, 426000 Russia

In fact, numerous experimental data demonstrate that solid solutions are nonideal. For example, in alloys Fe–Cr at 1100–1300°C [1, 2], Fe–V at 1220–1420°C [3], Fe–Mn at 1170–1590°C [4], Fe–Co up to 1200°C [5], and in many others, either positive or negative deviations from ideality are observed. These deviations mean that the structure of a solid solution in these systems cannot be fixed upon approaching the system to equilibrium. Thus, the question arises as to why solid-solution domains are usually shown in equilibrium phase diagrams when it is known that these solid solutions are nonideal and, therefore, must decompose upon approaching the system to the equilibrium? Apparently, the concept of the existence of the solid-solution domains in the equilibrium phase diagrams appeared based on numerous experimental results obtained by differential thermal and X-ray phase analyses. It is well known that these methods, used routinely for constructing equilibrium phase diagrams, are not able to reveal a stage of the decomposition process such as cluster formation; therefore, these methods do not make any distinction between the cluster-containing structure and the structure of homogeneous solid solutions.

It is well known that clusters are formed at the initial stages of the decomposition process either as a consequence of the tendency of alloys to phase separation or as a consequence of the tendency of nonstoichiometric compositions to ordering [6]. The clusters can be intermediate products of the decomposition process both on the way to the formation of the mixture of crystals formed by pure components (tendency to phase separation) and on the way to the formation of particles of chemical compound A_mB_n in nonstoichiometric compositions (tendency to ordering). The clusters can also be final products of the decomposition process arising when the concentration of the second component in the alloy is not sufficiently high for forming an equilibrium phase (either the A_mB_n particles or a mixture of crystals of pure components) [6]. The clusters are easily identified by structural methods (transmission electron and field-ion microscopy); their chemical composition can be determined by using electron energy loss spectrom-
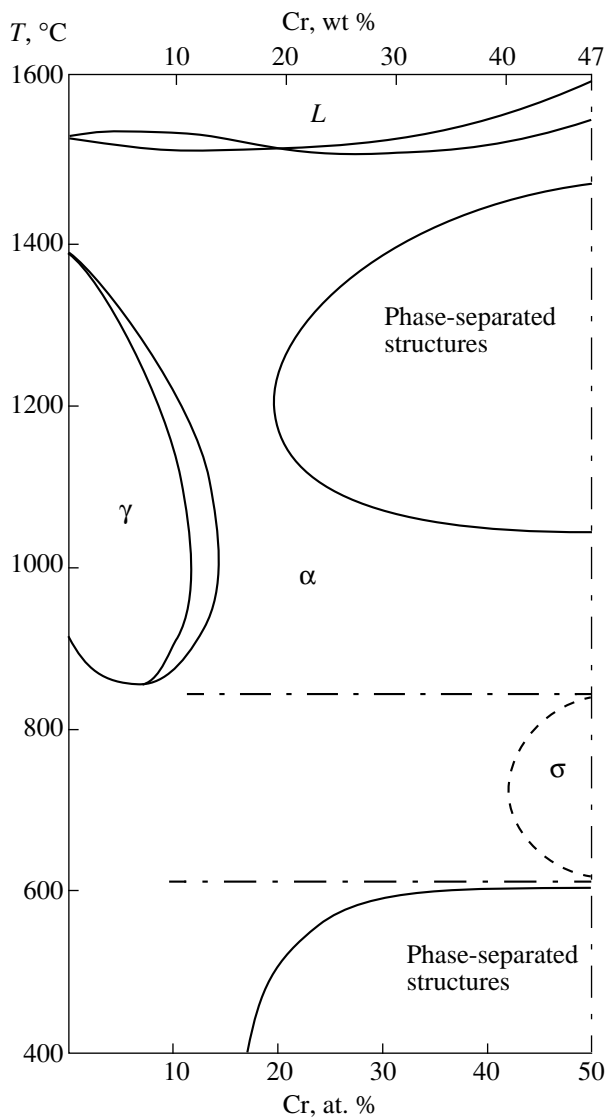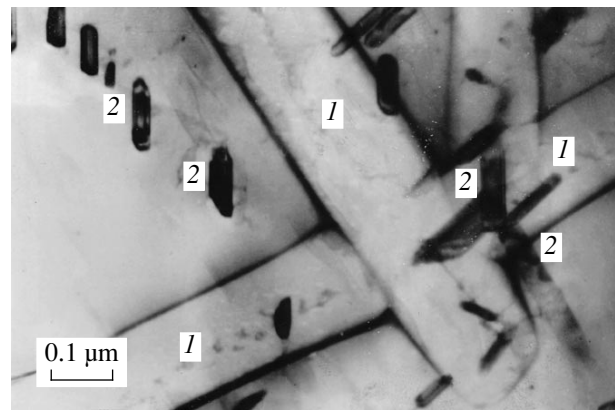
Fig. 1. Iron-reach region of the iron–chromium equilibrium phase diagram. The dot-and-dash curves indicate the lines of the second-order phase separation–ordering phase transitions [10].

Fig. 2. Electron domains formed in the Fe–47% Cr alloy after the initial thermal treatment favoring the phase-separated structure (quenching from 1200°C, 1 hour in water) and the subsequent thermal treatment ensuring the transfer to the ordering region (700°C, 4 hours cooling in water). Notation: (*1*) electron domains; and (*2*) undissolved particles of the phase-separated structures.

etry in the electron microscope and also by the use of an atomic probe. However, it is not possible to use some separate structural data to find what tendency, to ordering or to phase separation, is responsible for the formation of clusters. To make a definite conclusion, we need a comprehensive investigation, for example, one such as that reported in [7, 8].

Here, we present several examples supporting the fact that the solid solutions in the phase diagrams are not equilibrium phases and decompose owing to their tendency to phase separation. The Fe–Cr alloys are known [9] to form a continuous sequence of solid solutions within the entire range of concentrations and temperatures, except those compositions which are close to equiatomic; for these, the formation of the σ phase is characteristic at 440–830°C. However, the precision

electron-microscopy investigations of the structure of Fe–(20–47)% Cr in the range of their solid solutions show that, at 1100–1450°C and also at temperatures below 600°C, these alloys undergo phase separation with the formation of chromium-enriched clusters of various morphology inside the chromium-depleted matrix, the particles of pure chromium are also identified in these alloys at 1200–1400°C [10]. The results of these investigations are shown in the form of a phase diagram (Fig. 1). In this phase diagram, we also indicate the lines of the second-order phase transformations of the phase separation–ordering type. At these lines, the tendency of the alloy to phase separation changes to the tendency to ordering. The phase separation–ordering phase transitions were revealed in Fe–Cr alloys owing to the formation of the so-called electron domains in their structure (Fig. 2). Similar to magnetic domains, these domains are observed employing the defocusing technique; they are regions with electron structure different from that of the matrix [10].

It is usually assumed that the Fe–Co alloys form a continuous sequence of solid solutions above 730°C. Below this temperature, B2 type ordering [9] takes place in these alloys. Through a routine X-ray structural analysis [11], it was shown that the $(110)_\alpha$ line bifurcates into the (110) line of the bcc iron and the (111) line of the fcc cobalt at a temperature above 730°C; that is, the phase separation into components occurs in these alloys and the temperature of 730°C is nothing but the line of the phase separation–ordering phase transition.

Generalizing numerous experimental and theoretical results concerning the decomposition of the Fe–Ni alloys in the Invar (30–40% Ni) range of compositions, a certain region was found in the phase diagram where

the phase separation of solid solutions into clusters enriched (50%) and depleted (25%) by nickel (Fig. 3) [12] occurs at high temperatures.

It was shown [13] that the solid-solution domain in the Fe–Ti phase diagram [9] is the domain where the tendency to phase separation manifests itself at all points. Depending on the alloy composition, this tendency leads either to the tweed structure or to the modulated periodic structure. It was found that, in the Fe−5.0% Ti alloy, for example, the titanium content in enriched and depleted clusters differs approximately by a factor of 10 (according to the results of atomic-probe analysis). Similar results (the coexistence of the phase-diagram domains where the tendency to phase separation manifests itself and those in which the tendency to ordering takes place) were also observed in the Fe–Al, Fe–Si, and Al–Li systems and in many nickel-based alloys [14]. The authors of [14] considered such behavior of the systems mentioned above in terms of instability of disordered or ordered phases with respect to the phase separation, ordering, or disordering. Such a purely phenomenological approach beyond the framework of chemical thermodynamics is not able to clarify the true causes of the change in the chemical orientation of the components in the same system with the variation of the composition or temperature. We attempted to find these causes by X-ray electron spectroscopy. It was shown that the X-ray electron spectra of the Fe–50% Co-alloy valence band at temperatures below 730°C, when the tendency to ordering was revealed, and above 730°C, when the tendency to phase separation takes place, were different. At $T > 730$°C, the shape of the X-ray electron spectrum of the valence band becomes similar to a superposition of the valence bands of pure iron and cobalt.

The above discussion leads us to the following conclusions.

The usual assumption of the existence of the domains corresponding to equilibrium solid solution in the equilibrium phase diagrams is not confirmed by the structural experimental data. If we do not take into account the highly diluted solid solutions obeying the Henry law and the solid solutions at very high temperatures, at which their thermal energy is essentially higher than the energy of a chemical bond between the atoms of the components composing the alloy, we can argue that the so-called domains of existence for equilibrium solid solutions are, in fact, the regions where $E_{mix} > 0$ and that the phase separation of the alloy into clusters and, eventually, into a mixture of crystals of pure components occurs.

The experimental determination of deviations in the behavior of solid solutions from the Raoult law usually undertaken at high temperatures characterizes the state of alloys only in the measured point of the phase dia-
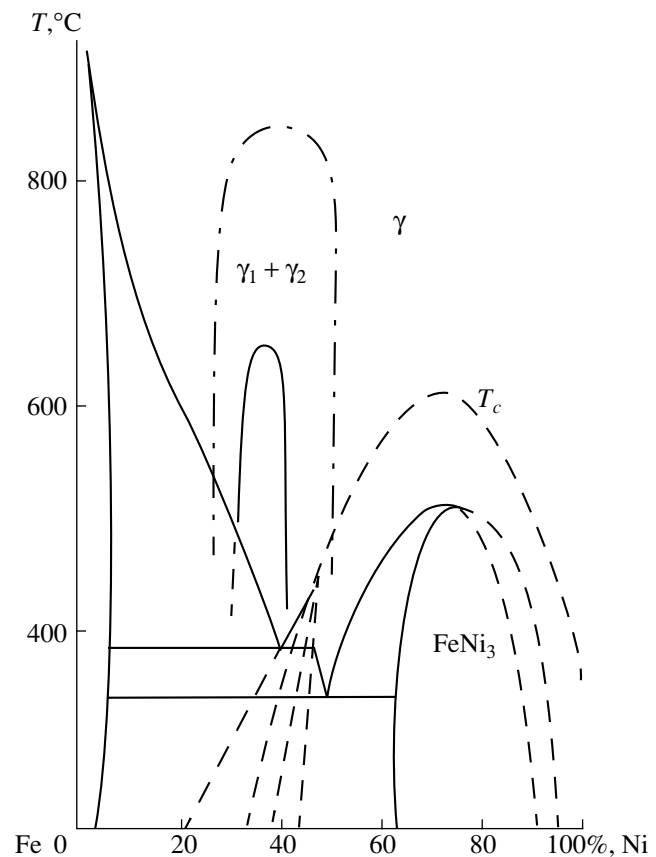
Fig. 3. Equilibrium phase diagram of Fe–Ni alloy. The high-temperature phase separation $\gamma \longrightarrow \gamma_1 + \gamma_2$ is denoted by a solid line for the case of thermal treatment and by the dot-and-dash line for the case of irradiation [12].

gram. From these data, it is impossible to come to definite conclusions concerning the sign of the deviations within all the other regions of the phase diagram as is often presently done.

In the phase diagrams, the coexistence of the domains where the ordering occurs (with the following formation of a chemical compound) with the regions where the phase separation takes place makes it possible to consider these systems as being able to change the sign of the chemical orientation of the components with respect to each other depending on variations in composition and temperature.

REFERENCES

1. E. Z. Vintaĭkin, Dokl. Akad. Nauk SSSR **118**, 977 (1958).

2. Y. Jeannin, C. Mannerskantz, and F. D. Richardson, Trans. Met. Soc. AIME **227**, 300 (1963).

3. K. M. Myles and A. T. Aldred, J. Phys. Chem. **68**, 64 (1964).

4. P. Roy and R. Hultgren, Trans. Met. Soc. AIME **233**, 1811 (1965).

5. A. S. Normanton, P. E. Bloomfield, F. R. Sale, and B. B. Argent, Met. Sci. **9**, 510 (1975).

6. Yu. I. Ustinovshchikov, *Precipitation of the Second Phase in Solid Solutions* (Nauka, Moscow, 1988).

7. Yu. I. Ustinovshchikov and B. E. Pushkarev, Metally, No. 2, 52 (1999).

8. Yu. I. Ustinovshchikov and I. A. Igumnov, Fiz. Met. Metalloved. **86** (2), 74 (1998).

9. O. Kubaschewski, *Iron-Binary Phase Diagrams* (Springer, Berlin, 1982; Metallurgiya, Moscow, 1985).

10. Yu. I. Ustinovshchikov and B. E. Pushkarev, Materialovedenie, No. 12, 28 (1999).

11. Yu. I. Ustinovshchikov and S. E. Treshcheva, Metally, No. 3, 62 (1999).

12. K. C. Russel and F. A. Garner, Metall. Trans. A **23**, 1963 (1992).

13. I. A. Igumnov, Author's Abstract of Candidate's Dissertation (Izhevsk, 1999).

14. H. Chen, KEK Proc. **94** (9), 62 (1995).

Translated by V. Bukhanov

================= **MECHANICS** =================

Method of Resonance Overcompression in a Bubble Liquid by a Moderate Aperiodic Action

Academician R. I. Nigmatulin, A. A. Gubaĭdullin, and O. Sh. Beregova

Received July 3, 2000

Several years ago, the phenomenon of sonoluminescence, that is, the luminescence of gas bubbles in an acoustic field, was discovered [1, 2]. This phenomenon is of interest not only from the scientific point of view; it also has a number of important applications for practice. For example, the appearance of such a direction in chemical technology as sonochemistry is associated with the discovery of sonoluminescence. By virtue of the appearance of high temperatures in bubbles, the acoustic field can initiate certain chemical reactions which are impossible under other conditions. But the most impressive fact is that a nuclear-fusion reaction can be initiated in bubbles at superhigh temperatures. Deuterium bubbles in heavy water at overcompressions can release thermonuclear energy ("bubble nuclear fusion"), but a routine ultrasound is not sufficient to make this take place.

In recent years, a number of studies [3–11] were devoted to the theoretical description of the behavior of an individual gas bubble vibrating in a liquid under a wave-field action provided that the pressure and temperature in the gas can reach extremely high values. The principal idea of the new approach [7], referred to as the "basketball" mode, is the coordination of the process of varying the pressure in a liquid with the forced vibrations of a bubble and the use of a nonlinear resonance during an aperiodic action of an external field of a moderate-amplitude pressure. To realize this idea, we formulated and solved the problem of spherically symmetric vibrations of a gas bubble in a compressible liquid [8–10]. On the basis of the analytical solution obtained, we developed an efficient computer code for the mathematical simulation of the bubble collapse with allowance for various dissipative mechanisms, such as viscosity, heat conduction, radiation, ionization, wave processes around and inside the bubble, and heat-and-mass exchange between the bubble and the ambient liquid under overcompressions of the bubble.

The investigation of the processes taking place in an individual collapsing bubble is obviously an important and necessary stage; however, the above applications are associated with a bubble liquid, i.e., a mixture of

carrier liquid with a large quantity of bubbles dispersed in it.

In this study, we propose a method for processing a limited volume of the bubble liquid by an aperiodic moderate-amplitude wave action, as a result of which waves arise with amplitudes exceeding that of the initiating action by several orders of magnitude. This method is illustrated by the results obtained from a direct numerical simulation.

We consider a cylindrical volume of bubble liquid, which has the length L bounded by solid walls and a mobile piston (Fig. 1).

The basketball mode for the excitation of the gas–liquid-mixture is realized by means of specifying the following boundary condition at the piston:

$$p_p = \begin{cases} p_{max}, & v_p \geq 0 \\ p_{min}, & v_p < 0, \end{cases}$$

where p_p and v_p are the pressure and velocity of the medium at the piston. In such a situation, the waves traveling from the piston to the wall, the waves reflected from the wall and traveling back to the piston reflected from it, etc. propagate in the bubble mixture.

For the numerical investigation of the problem formulated, we use the model of the dynamic behavior of a bubble liquid and the method of its computer realization outlined in [12].

In Fig. 2, we show the time dependences for the pressure at the piston, the piston velocity, and the gas pressure in bubbles in the middle of the volume ($x = L/2$) calculated for the case of the basketball and wave ($p_p = p_{max}$) modes of excitation of the hydrogen–glycerin bubble mixture with the parameters $a_0 = 1$ mm,

Institute of Theoretical and Applied Mechanics
(Tyumen Branch), Siberian Division, Russian Academy
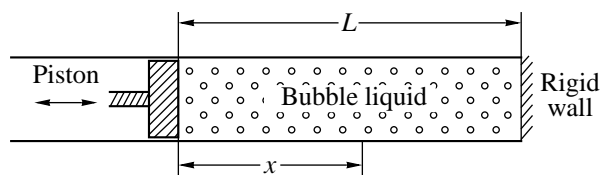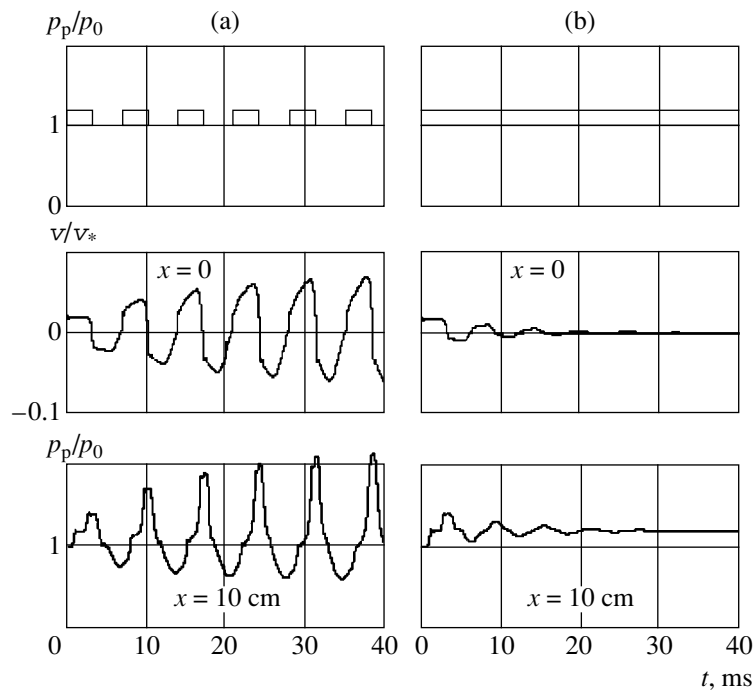*of Sciences, Tumen, Russia*

Fig. 1. Schematic of the piston excitation for a bubble liquid.

Fig. 2. Profiles of liquid and gas pressures and piston velocities for (a) basketball mode and (b) steady-state mode of bubble-liquid excitation.

$\alpha_0 = 2\%$, $T_0 = 293$ K, $L = 20$ cm, $p_0 = 10^5$ Pa, $p_{max} = 1.2p_0$, $p_{min} = p_0$, and $v_* = \sqrt{p_0/\rho_1}$, where a, α, ρ, T, and p are the radius and volume content of the bubbles, the density, temperature, and pressure, respectively. The subscripts l and g denote the liquid and gas parameters, and 0 implies the initial values of the parameters.

It can be seen (Fig. 2) that the maximum gas pressure in the bubbles grows for the basketball mode of the piston motion during each subsequent travel of a wave, whereas for a constant pressure at the piston (a step-like wave), the gas pressure in the bubbles tends to the pressure at the piston.

Figure 2 confirms the fundamental possibility for excitation of overcompression in a bubble mixture by means of an aperiodic moderate-amplitude action.

The mechanical system under consideration exhibits a resonance. Comparing the eigenfrequencies of this vibrating system and those of the bubble vibrations in the mixture, it is possible to estimate the system parameters for which the excitation mode is resonant.

The eigenfrequency ω_S of the system for the wave excitation can be estimated as

$$\omega_S = \frac{2\pi}{T}, \quad T = \frac{L}{D_S} + \frac{L}{D_R},$$

where D_S and D_R are the velocities for the wave traveling from the piston and the wave reflected from the wall, respectively. Their values can be calculated in the

equilibrium approximation from the formulas

$$D_S = \sqrt{\frac{p_{max}}{\alpha_0\rho_1}}, \quad D_R = \sqrt{\frac{p_R}{\alpha_S\rho_1}},$$

$$p_R = \frac{p_{max}^2}{p_0}, \quad \alpha_S = \frac{\alpha_0 p_0}{p_{max}},$$

where α_S is the volume gas content behind the incident wave and p_R is the pressure behind the wave reflected from the wall.

The eigenfrequency ω_R of the bubble vibrations in the mixture can be determined from the formula

$$\omega_R = \frac{1}{a}\sqrt{\frac{3\gamma p_{max}}{(1-\varphi)\rho_1}}, \quad \varphi = \frac{1.1\alpha_0^{1/3} - \alpha_0}{1 - \alpha_0},$$

where γ is the gas adiabatic index and φ is the correction taking into account the fact that the bubbles are not single.

Equalizing the frequencies ω_S and ω_R, we can find the resonance values of the parameters. As can be seen from the formulas, one of the parameters (a_0, α_0, L, p_{max}) is determined by the resonance condition from the given values of the remaining parameters (for the chosen liquid and gas).

In Fig. 3, we display the calculated oscillograms for pressure in the liquid, pressure and temperature in the gas bubbles, the radius, and the volume content of the bubbles situated in the middle of the volume ($x = L/2$) for the resonance excitation of a water–air gas–liquid
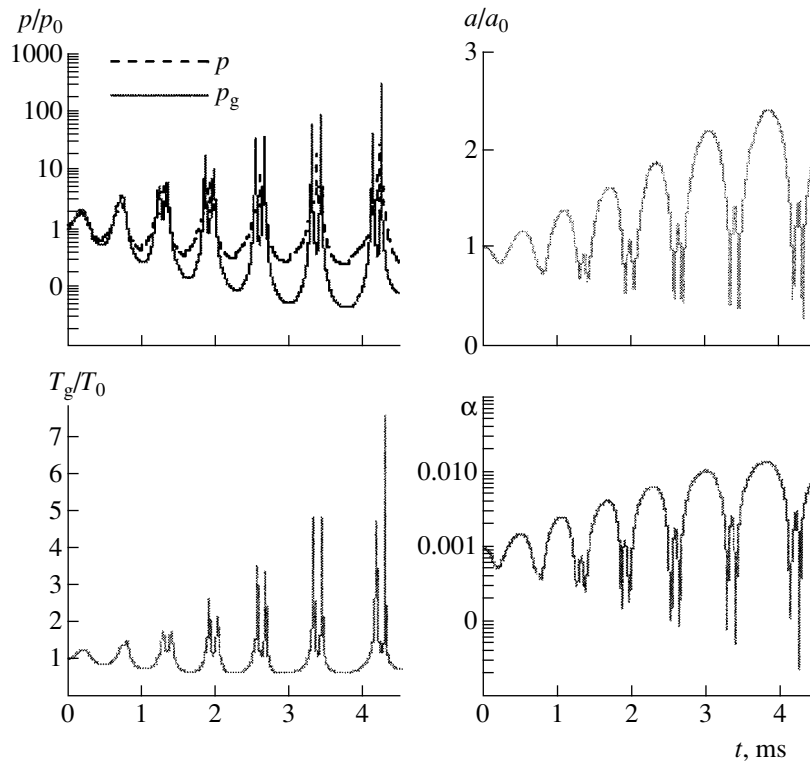
Fig. 3. Profiles of liquid and gas pressures, radius, temperature, and volume concentration of bubbles in the case of the resonance excitation.

mixture with the parameters $a_0 = 1$ mm, $\alpha_0 = 0.1\%$, $T_0 = 293$ K, $L = 5$ cm, $p_0 = 0.1$ MPa, and $p_{\max} = 1.5 p_0$. It can be seen that, in this case, the pressure amplitude is two orders of magnitude higher than that of the initiating pulse, whose amplitude is only 0.05 MPa. As this takes place, the gas temperature increases to a value higher than 2000 K for a short time. The time dependences for the bubble radius a, radial velocity w, and volume concentration α show that the amplitudes of their vibrations increase with time.

The wave properties of the bubble liquid have been relatively well studied. The behavior of shock waves depends on the choice of carrier liquid phase (its density and viscosity), but is to a greater extent determined by the dispersed phase, even when it is small not only in mass, but also in volume. The gas properties in bubbles, their size, and the character of the interphase heat exchange can radically influence the structure of the shock wave.

The numerical analysis carried out showed that with decreasing the radius of the bubbles the response of the bubble mixture is enhanced in the resonance-excitation mode. This fact agrees with the conclusion obtained in [10] for an individual bubble.

Thus, we have proposed the method of the resonance excitation of a bounded volume of a bubble liquid by an aperiodic moderate-amplitude action, as a result of which extremely high pressures and tempera-

tures can be achieved for a gas in bubbles. This fact is qualitatively illustrated by the profiles of the pressure, temperature, bubble radius, etc. calculated in terms of the single-velocity two-temperature model with two pressures in the bubble mixture with an incompressible liquid phase. In order to obtain more exact quantitative information associated with particular applications, e.g., with the problem of bubble nuclear fusion, it is necessary to develop more complicated models of bubble liquids, which take into account various dissipative mechanisms, such as the compressibility of the liquids, radiation, ionization, wave processes around and inside individual bubbles, etc.

REFERENCES

1. K. S. Suslik, Sci. Am., No. 2, 80 (1989).

2. D. F. Gaitan, L. A. Crum, C. C. Church, and R. A. Roy, J. Acoust. Soc. Am. **91**, 3166 (1992).

3. V. Kamath, A. Prosperetti, and F. N. Egolfopulos, J. Acoust. Soc. Am. **94**, 248 (1993).

4. L. A. Crum and R. A. Roy, Sonolumin. Sci. **266** (14), 233 (1994).

5. C. C. Wu and P. H. Roberts, Phys. Rev. Lett. **70**, 3424 (1993).

6. R. I. Nigmatulin, I. Sh. Akhatov, N. K. Vakhitova, and R. T. Lahey, Chem. Eng. Commun. **168**, 145 (1998).

7. R. I. Nigmatulin, V. Sh. Shagapov, N. K. Vakhitova, and R. T. Lekhi, Jr., Dokl. Akad. Nauk **341**, 37 (1995) [Phys. Dokl. **40**, 122 (1995)].

8. R. I. Nigmatulin, I. Sh. Akhatov, and N. K. Vakhitova, Dokl. Akad. Nauk **348**, 768 (1996) [Phys. Dokl. **41**, 276 (1996)].

9. I. Sh. Akhatov, N. K. Vakhitova, G. Ya. Galeeva, *et al.*, Prikl. Mat. Mekh. **61**, 952 (1997).

10. R. I. Nigmatulin, I. Sh. Akhatov, and N. K. Vakhitova, Prikl. Mekh. Tekh. Fiz. **40** (2), 111 (1999).

11. A. A. Aganin and M. A. Il'gamov, Prikl. Mekh. Tekh. Fiz. **40** (2), 101 (1999).

12. A. A. Gubaĭdullin, A. I. Ivandaev, and R. I. Nigmatulin, Prikl. Mekh. Tekh. Fiz., No. 2, 78 (1978).

Translated by V. Bukhanov

<center>════════════════ **MECHANICS** ════════════════</center>

An Efficient Numerical–Analytical Solution to Variational Problems in Mechanics

L. D. Akulenko and S. V. Nesterov

Presented by Academician D.M. Klimov December 22, 1999

1. A basically new numerical–analytical method of solving nonlinear boundary value problems for Euler–Lagrange equations is presented. This method is based on the application of the dependence of deficient initial data on the interval length and the specific introduction of a small parameter. In addition to conventional approaches associated with the determination and reduction of residuals of the solution (integral residuals or those at finite points), we also propose to find and use the residual (with respect to the argument) of an approximate solution. Both residuals in their combination testify to the existence of the solution and define its accuracy. Such an approach enables us to construct a recursion algorithm with a high computational efficiency, namely, simplicity, effectiveness, accelerated (quadratic) convergence, and immunity to both malfunctions and an accumulation of rounding-off errors. The advantages of this approach are significant in the case of bulk high-precision calculations of multiparametric problems (parametric synthesis of mechanical systems). This method is also fairly efficient when studying problems of the Sturm–Liouville type for determining the eigenfrequencies and oscillation modes of highly inhomogeneous distributed systems, including solving generalized boundary value problems [1].

For definiteness, we consider a classical variational problem of the form [2]

$$\int_0^l F(x, y, z)dx \rightarrow \min_y, \quad z = y', \quad (1)$$
$$\varphi(x, y, z)|_{x = 0, l} = 0, \quad (y, z) \in G.$$

Here, F and φ are sufficiently smooth functions of scalar arguments x, y, and z and G is an open bounded domain. Function φ determines the nonlinear boundary conditions at $x = 0, l$. In addition to separated boundary conditions (1), we can deal with mixed boundary con-

Institute of Problems in Mechanics,
Russian Academy of Sciences, pr. Vernadskogo 101,
build. 1, Moscow, 117526 Russia

ditions. In particular, at $x = 0, l$, the equalities $y = 0$ or $z = 0$ can take place, which are usually met in solving applied problems.

Assuming that the necessary Legendre condition is satisfied, we formulate the boundary value problem for the Euler–Lagrange equation [2]:

$$y' = z, \quad z' = f(x, y, z), \quad 0 \leq x \leq l,$$
$$\varphi(x, y, z)|_{x = 0, l} = 0, \quad (2)$$
$$f \equiv (F'_y - F''_{xz} - zF''_{yz})/F''_{z^2}, \quad F''_{z^2} \neq 0, \quad (y, z) \in G.$$

The function f in (2) is considered to be sufficiently smooth. We need to construct a set $\{y_i(x)\}$ of smooth solutions and select an optimum solution to bring the functional (1) to the minimum. Note that the functions F, f, and φ may depend on the vector of the system's parameters and that a family of solutions should be constructed (parametric synthesis, see Section 4). For brevity, we present the procedure of solving the problem with the boundary conditions $y(0) = y(l) = 0$; subsequent possible generalizations will require obvious modification.

2. We assume that the deficient value of $y'(0) = p$ is known and equal to p_0. It can be determined on the basis of the variational approach by using appropriate trial functions. We construct numerically the solution to the Cauchy problem for system (2), $y_0 = Y(x, p_0)$, $z_0 = Z(x, p_0)$, and require that $(y_0, z_0) \in G$ together with a certain vicinity. We calculate a root (zero) of the function Y, which is the nearest to l, and introduce a small parameter ε inherent in the problem

$$\xi = \text{argmin}_i |l - \xi_i|, \quad \xi_i = \text{Arg}_x Y(x, p_0),$$
$$\varepsilon = 1 - \xi/l, \quad 0 \leq |\varepsilon| \ll 1. \quad (3)$$

This parameter characterizes the closeness of the estimate p_0 to p and the accuracy of the desired solution to the boundary value problem (2). For $\varepsilon < 0$ (i.e., $\xi > l$), the function f is extended smoothly for $l < x \leq \xi$. The determination of the value $\xi = \xi(p_0)$ (3) is necessary for the reliable inference of the existence of the solution. It is calculated rather easily through the process of integrating the Cauchy problem. The root ξ is considered to

be nondegenerate, $Z(\xi, p_0) \neq 0$, indicating its uniqueness at sufficiently small $|\varepsilon| > 0$. As a result of the smoothness of Y and Z with respect to p_0, the closeness of p_0 to p implies the smallness of parameter ε. The inverse statement is generally incorrect because of the presence of focal points [e.g., $y'' = -(\pi/l)^2 y$]. Furthermore, we consider the general situation and assume that, in the ε-vicinity of the point $x = l$, there are no focal points; i.e., while varying p_0, a similar displacement of the point $x \approx l$ occurs (and vice versa). This implies that the parameter $p = p(l)$ strongly depends on l: the derivative $p'(l) \sim 1$ with respect to the small parameter ε is $c_1|\varepsilon| \leq |p - p_0| \leq c_2|\varepsilon|$, where $c_{1,2} > 0$; the constructive condition is contained in (5).

In addition to the initial boundary value problem (2) for the unknown y, we consider the adjoint problem for the sensitivity function $s = \dfrac{\partial y}{\partial l}$. We have

$$u' = w, \quad w' = f_y' u + f_z' w,$$
$$u(0) = 0, \quad w(0) = 1; \qquad (4)$$
$$s = ku, \quad k(l) = p'(l), \quad s(l) = -z(l).$$

Relationships (4) are variational equations for y. We calculate the unknown quantity k using the boundary condition for s and derive $k(l) = -z(l)/u(l)$ under the assumption $u(l) \neq 0$. Note that the functions y, s, and u depend on the parameter l.

Let the expression $p = p_0 + \varepsilon lk + \varepsilon^2 \dots$ be the basis for the recursion algorithm similar to the Newton's tangent method (of the first order) [3] for determining the desired quantity $p = p(l)$ within the required accuracy with respect to ε. The following operations are executed at the initial stage:

(i) the estimate p_0 for the quantity $p(l) = z(0)$ is found;

(ii) the Cauchy problem (2) is integrated at $y(0) = 0$ and $z(0) = p_0$; i.e., the functions $y_0(x) = Y(x, p_0)$ and $z_0(x) = Z(x, p_0)$ are calculated;

(iii) in the calculation procedure according to (3), the root (zero) $\xi = \xi_0$ of the function $y_0(x)$, which is nearest to $x = l$, and the small parameter $\varepsilon = \varepsilon_0$ are determined;

(iv) the Cauchy problem (4) is integrated simultaneously with (2); and

(v) the estimate k_0 is calculated for $k(l) = p'(l)$: $k_0 = -z_0(\xi_0)/u_0(\xi_0)$.

3. At the first step of the iterative algorithm, the values of the desired quantities are refined by operations (i)–(v). Note that, in operation (i), the approximation p_1 of the parameter p is determined as $p_1 = p_0 + \varepsilon_0 lk_0$, where all quantities are known.

Furthermore, operations (ii)–(iv) are performed on the basis of the refined value p_1:

The functions $y_1(x) = Y(x, p_1)$ and $z_1(x) = Z(x, p_1)$ are calculated.

The root ξ_1 of the function $y_1(x)$ is determined in the ε_0^2-vicinity of $x = l$, and the parameter $\varepsilon_1 = 1 - \xi_1/l$ is calculated.

Function $u_1(x)$ is found simultaneously with y_1.

The refined estimate $k_1 = -z_1(\xi_1)/u_1(\xi_1)$ is calculated.

Subsequent iterations are then performed by induction and approximations of arbitrarily high orders are determined. Indeed, according to (i)–(v), on the basis of values of the nth approximation, namely, p_n, ξ_n, ε_n, k_n, and $y_n(x)$, $z_n(x)$, $u_n(x)$, we derive the solution of the $(n + 1)$th approximation:

$$p_{n+1} = p_n + \varepsilon_n lk_n,$$
$$\xi_{n+1} = \mathrm{argmin}|l - \mathrm{Arg}_x Y(x, p_{n+1})|,$$
$$\varepsilon_{n+1} = 1 - \xi_{n+1}/l,$$
$$k_{n+1} = -z_{n+1}(\xi_{n+1})/u_{n+1}(\xi_{n+1}), \qquad (5)$$
$$z_{n+1}(\xi_{n+1}) \neq 0, \quad u_{n+1}(\xi_{n+1}) \neq 0;$$
$$y_{n+1}(x) = Y(x, p_{n+1}), \quad z_{n+1}(x) = Z(x, p_{n+1}),$$
$$u_{n+1}(x) = U(x, p_{n+1}).$$

Here, $Y(x, p_{n+1})$, $Z(x, p_{n+1})$, and $U(x, p_{n+1})$ are obtained as a result of the simultaneous solving of Cauchy problem (2), (4) under the conditions $y(0) = u(0) = 0$, $z(0) = p_{n+1}$, and $w(0) = 1$.

Next, we estimate the rate of the convergence of algorithm (5). We assume that the estimate p_0 is close to the exact value $p(l) = z(0)$ and the initial parameter ε (3) is sufficiently small. Then, using methods of the perturbation theory, we can prove that for p_n, the inequalities $c_1|\varepsilon_n| \leq |p - p_n| \leq c_2|\varepsilon_n|$ are valid ($c_{1,2} > 0$, $n = 0, 1, 2, \dots$). For the small parameter ε_n, we obtain the estimate $|\varepsilon_n| \leq d\varepsilon_{n-1}^2 \leq d^{-1}(d\varepsilon)^{\theta(n)}$, where $\theta(n) = 2^n$ ($n \geq 1$). This estimate corresponds to the accelerated convergence of the algorithm for a sufficiently small $|\varepsilon| > 0$. The constants $c_{1,2}$ and d are determined constructively on the basis of the method of successive approximations and estimates for z and s. The functions $y_n(x)$, $z_n(x)$, and $u_n(x)$ converge with an increased rate to the desired solution to problems (2) and (4) over the uniform metric for all x within the range $0 \leq x \leq l$.

The proof of the existence and uniqueness of the desired solution $(y(x), z(x)) \in G$ and the estimate of the radius of convergence for the parameter ε are carried out by methods of the perturbation theory on the basis of the Schauder–Banach theorems for the compression operator [3]. For this purpose, the initial boundary value problem (2), containing no small parameters in the explicit form, is reduced to the standard-type per-

turbed problem by transforming the argument in the spirit of the Lyapunov–Poincaré approach [4, 5]:

$$\eta' = \zeta, \quad \zeta' = (1-\varepsilon)^{-2} f((1-\varepsilon)^{-1}\theta, \eta, (1-\varepsilon)\zeta),$$
$$\eta(0) = \eta(\xi) = 0; \tag{6}$$
$$\theta = \xi x / l, \quad 0 \le \theta \le \xi, \quad y(x) \equiv \eta(\theta, \varepsilon).$$

Here, the value $\xi = \xi_0$ is fixed according to (3) and ε is a small parameter. Assuming $\varepsilon = 0$, we arrive at an unperturbed boundary value problem with the known solution $\eta_0 = Y(\theta, p_0)$. Substituting $\eta = \eta_0 + \delta\eta$, $\delta\eta \sim \varepsilon$ and performing identical transformations, we reduce problem (6) to the quasi-linear form. The unknown quantity $\delta\eta$ is constructed by successive approximations in terms of powers of ε, the algorithm of the solution being substantiated in a standard manner [5]. However, this approach is inefficient for numerical calculation because of the comparatively slow convergence ($\varepsilon_n \sim \varepsilon^n$). A more significant difficulty is associated with the rapid complicating of derived expressions and accumulating of rounding-off errors with increasing the iteration number. Such drawbacks are almost absent in the recursion algorithm (5) presented above. This algorithm converges very rapidly, and only parameter $p(l)$ needs to be corrected. All defining equations and functions have the same form, and they do not become more complicated.

The computational practice confirms the high efficiency of the accelerated-convergence algorithm. For example, at $\varepsilon \sim 0.1$–0.01, the relative error 10^{-N} ($N = 4$–8) is attained in two to three iterations: $n \approx 1.4\ln N \approx 2$–$3$. The shooting method and the method of successive approximations require, respectively, $n \approx 3.3N \approx 13$–$26$ and $N \approx 4$–8 iterations (without the difficulties mentioned above). The applicability of the quasi-linearization method [3, 6] is hindered in the presence of internal focal points and envelopes of the trajectory family; this method is substantiated for a short interval of changing the argument (property of the monotonicity [3, 6], see Section 4.1).

4. We now consider examples of particular significance.

4.1. Problem (2) at $f = \alpha\exp(\beta y)$, where α, $\beta = \text{const} > 0$, is of interest for its relevance in magnetic hydrodynamics [3, 6]. By substitutions $x_* = \sqrt{\alpha\beta}\, x$ and $y_*(x_*) = \beta y(x)$, we reduce this problem to the case of $\alpha = \beta = 1$. The equation is integrated analytically. Then the system of two transcendental equations with respect to p (or ω) and δ needs to be solved:

$$\exp(-y/2) = (\sqrt{2}\omega)^{-1}\cos(\omega x + \delta),$$
$$l = (2/\omega)\arccos\sqrt{2}\omega, \quad p = -2(1/2 - \omega^2)^{1/2}. \tag{7}$$

Parameter ω can be found from (7) numerically or graphically, and the desired quantity $p(l) \in [-\sqrt{2}, 0]$ is
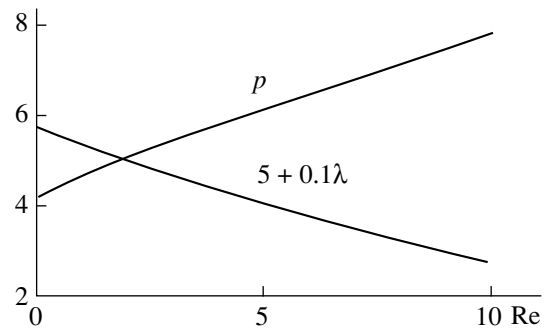
Velocity gradient p and its derivative λ at confuser walls as functions of the Reynolds number.

expressed in terms of $\omega(l)$. We use algorithm (5) for $l = 1$, taking a rough estimate $p_0 = -0.37$ [the exact estimate is $p(1) = -0.4636$] from the variational principle for the trial function $y_0 = -0.12\sin\pi x$; the parameter ε_0 is ~ 0.2. The second iteration yields the solution with a residual of 10^{-7}; the convergence and accuracy of computations for other $l \sim 1$ are almost the same.

4.2. We consider variational problems of mechanics which satisfy the Fermat principle (brachistochrone [2], sound channel [7], etc.). In (1), we have $F = (1 + z^2)^{1/2}/v(x, y)$, where the velocity $v > 0$ is determined by the force field or properties of the medium. For the practically important case $v(y)$, $y(x_{0,f}) = y^{0,f}$, we obtain the solution in the form of an improper quadrature:

$$x - x_0 = \pm\int_{y^0}^{y} [c^2 - v^2(s)]^{-1/2} v(s)ds, \quad y(x_f) = y^f. \tag{8}$$

The dependence of x on y is ambiguous; the unknown variable c should be determined, which is, to a certain extent, computationally difficult. Moreover, limitations are often imposed on the trajectory, e.g., $y(x) \ge 0$. Therefore, the explicit formula (8) is the "apparent" solution, so that the use of algorithm (3)–(5) is a simpler operation. For the function $v = v_0(1 + ay)$, the curve $y(x)$ is the arc of a circle with the center on the abscissa axis, which is shifted by $-a^{-1}$ [6]. For $x_0 = 0$, $x_f = 1$, we derive $p = p(y^0, y^f, a)$; more specifically, $p(0, 0, a) = a/2$. For the test values $a = 1$ and $p_0 = 0.45$ (the exact value of p is 0.5), the first iteration yields the residual $|p - p_1| = O(10^{-7})$; a similar calculation accuracy is attained after the first iteration for other values of the parameters a and $y^{0,f}$.

4.3. Next, we examine the plane problem for a flow of viscous fluid in a confuser (Hamel problem [8]). This problem admits variational formulation (1) under additional isoperimetric conditions of the constant fluid

flow rate. The boundary value problem is reduced to the form

$$y'' + a^2 y - b y^2 = \lambda, \quad y(0) = y(1) = 0,$$
$$y(x) \equiv 2\beta V(\theta), \quad x = 1/2(\theta + \beta),$$
$$q' = y - 1, \quad q(0) = q(1) = 0; \tag{9}$$
$$V_r(\theta, r) = -QV(\theta)/r, \quad Q = \text{const},$$

where $V_r(\theta, r)$ is the radial velocity; θ is the polar angle, $Q > 0$, $r > 0$; 2β is the angle between the confuser walls; $a = 4\beta$; $b = 2\beta\text{Re}$; and Re is the Reynolds number. Equations (9) are integrated in elliptic functions; the roots of a system of two transcendental equations with respect to the gradient $p = y'(0)$ and the Lagrange factor $\lambda = y''(0)$ should be determined. At present, the results of studies for two limiting cases $\text{Re} \ll 1$ and $\text{Re} \gg 1$ are known [8], the satisfactory accuracy being attained at $b \sim 10^3$–10^4 (i.e., $\text{Re} \sim 10^4$–10^5). Time-consuming calculations are required for the practically important moderate numbers $\text{Re} \sim 1$–10^2. This is why numerical results are insufficiently represented in the literature.

The technique developed makes it possible to obtain a high-precision solution with a residual of 10^{-6} to 10^{-7} for the Reynolds numbers indicated above. Shown in the figure for $\beta = 1$ are the quantities $p(\text{Re})$ and $\lambda(\text{Re})$, which determine the desired functions $y(x, \text{Re})$ and $q(x, \text{Re})$ as the solution to the Cauchy problem (9). It follows from the calculations (and this is consistent with concepts of mechanics) that the velocity gradient near confuser walls $p = y'(0) = |y'(1)|$ increases, whereas the velocity at the confuser axis ($x = 1/2$) decreases, with increasing Re.

REFERENCES

1. L. D. Akulenko and S. V. Nesterov, Dokl. Akad. Nauk **363**, 323 (1998) [Dokl. Phys. **43**, 714 (1998)].

2. N. I. Akhiezer, *Lectures on Calculus of Variations* (Gostekhizdat, Moscow, 1955).

3. L. Collatz, *Funktionalanalysis und Numerische Mathematik* (Springer-Verlag, Berlin, 1964; Mir, Moscow, 1968).

4. H. Poincaré, in *Selected Papers* (Nauka, Moscow, 1971, 1972), Vols. 1, 2.

5. I. G. Malkin, *Certain Problems in Theory of Nonlinear Oscillations* (Gostekhizdat, Moscow, 1956).

6. R. E. Bellman and R. E. Kalaba, *Quasi-Linearization and Nonlinear Boundary Value Problems* (American Elsevier, New York, 1965; Mir, Moscow, 1968).

7. L. M. Brekhovskikh, *Waves in Layered Media* (Akad. Nauk SSSR, Moscow, 1957; Academic, New York, 1960).

8. N. E. Kochin, I. A. Kibel', and N. V. Roze, in *Theoretical Hydromechanics* (Fizmatgiz, Moscow, 1963), Part 2.

Translated by A. Seferov

===== **MECHANICS** =====

A Mixed Problem of Dynamics

S. A. Zegzhda and M. P. Yushkov

Presented by Academician D.E. Okhotsimskiĭ November 25, 1999

It is well known that the theory of synthesis of mechanisms was founded by P.L. Chebyshev, who formulated and solved the problem of designing such machines whose particular points execute *a priori* given motions. Among such devices, we may recall, for example, mechanisms with stoppings of certain links in prescribed positions. We generalize this Chebyshev problem by requiring the motions of certain points of a mechanism to be the solutions to given differential equations of the nth order ($n \geq 0$). We assume that the mechanism is supplied by control forces whose number is equal to the number of equations involved. In [1–4], the authors proposed using the generalized principle of least constraint in the case of equations of the nth order ($n \geq 3$). However, it has been found that this approach can lead to paradoxical results [5, 6]. In this study, we use a new approach to the generalized Chebyshev problem. The approach is based on composing a closed set of differential equations with respect to the generalized coordinates and control forces. The consideration begins with the case of $n \geq 3$.

1. Formulation of the problem. Let the motion of a mechanical system under the action of the given generalized forces Q_σ be described in the generalized coordinates q^σ by the Lagrangian equations of the second kind:

$$\frac{d}{dt}\frac{\partial T}{\partial \dot{q}^\sigma} - \frac{\partial T}{\partial q^\sigma} = Q_\sigma, \quad T = \frac{M}{2} g_{\alpha\beta} \dot{q}^\alpha \dot{q}^\beta,$$

$$\sigma = 1, 2, \dots s, \quad \alpha, \beta = 0, 2, \dots, s, \qquad (1)$$

$$q^0 = t, \quad \dot{q}^0 = 1,$$

where M is the mass of the entire system. Henceforth, we assume that the summation is performed over the repeated subscripts.

We need to determine what time-dependent forces R_σ should be added to the forces Q_σ in order for the mo-

tion to satisfy the following set of differential equations:

$$f_n^\kappa \equiv a_{n\sigma}^\kappa(t, q, \dot{q}, \dots, \overset{(n-1)}{q})\overset{(n)}{q}{}^\sigma + a_{n0}^\kappa(t, q, \dot{q}, \dots, \overset{(n-1)}{q}) = 0,$$

$$\sigma = 1, 2, \dots, s, \quad \kappa = 1, 2, \dots k, \qquad (2)$$

$$k \leq s, \quad n \geq 3.$$

In the formulation of such a problem, attributes for both direct and inverse problems of dynamics are present. In fact, on one hand, the motion of the system can be found for the known forces Q_σ. On the other hand, the supplementary forces R_σ providing a motion for which Eq. (2) is fulfilled are sought as functions of time. For this reason, S.S. Grigoryan has proposed to call the formulated problem the *mixed problem of dynamics*. The application of the forces $R_\sigma(t)$ is realized owing to the control forces $\Lambda_\kappa(t)$. For $t = t_0$, we have

$$\Lambda_\kappa(t_0) = \Lambda_\kappa^0,$$

$$\dot{\Lambda}_\kappa(t_0) = \dot{\Lambda}_\kappa^0, \dots, \overset{(n-3)}{\Lambda}_\kappa(t_0) = \overset{(n-3)}{\Lambda}_\kappa^0, \qquad (3)$$

$$\kappa = 1, 2, \dots, k.$$

Let the forces R_σ and Λ_κ be related by the expressions

$$R_\sigma(t) = \Lambda_\kappa(t) b_\sigma^\kappa(t, q, \dot{q}),$$

$$\sigma = 1, 2, \dots, s, \quad \kappa = 1, 2, \dots, k,$$

with motion within the range $t_0 \leq t \leq t_*$ such that

$$\det[a_{n\sigma}^\mu b_\tau^\kappa g^{\sigma\tau}] \neq 0, \quad \sigma, \tau = 1, 2, \dots, s, \qquad (4)$$

$$\kappa, \mu = 1, 2, \dots, k.$$

Here, $g^{\sigma\tau}$ are elements of the matrix reciprocal with respect to the matrix having elements $g_{\sigma\tau}$.

We can show that, under the assumptions made and according to the initial data,

$$q^\sigma(t_0) = q_0^\sigma, \quad \dot{q}^\sigma(t_0) = \dot{q}_0^\sigma, \quad \sigma = 1, 2, \dots, s, \quad (5)$$

given that we can unambiguously find, in the indicated interval of time, such forces $\Lambda_\kappa(t)$ ($\kappa = 1, 2, \dots, k$) for which the motion satisfies equations (2).

St. Petersburg State University, Universitetskaya nab. 7/9, St. Petersburg, 199164 Russia

Adding the forces R_σ to the forces Q_σ and introducing a tangent space makes it possible to write out the set of Eqs. (1) in the form of a single vector equation [5]:

$$M\mathbf{W} = \mathbf{Y} + \Lambda_\kappa \mathbf{b}^\kappa, \quad \kappa = 1, 2, ..., k, \qquad (6)$$

in which

$$\mathbf{Y} = Q_\sigma \mathbf{e}^\sigma, \quad \mathbf{b}^\kappa = b_\sigma^\kappa \mathbf{e}^\sigma,$$

$$\mathbf{W} = (g_{\sigma\tau}\ddot{q}^\tau + \Gamma_{\sigma,\alpha\beta}\dot{q}^\alpha\dot{q}^\beta)\mathbf{e}^\sigma = (\ddot{q}^\sigma + \Gamma_{\alpha\beta}^\sigma \dot{q}^\alpha \dot{q}^\beta)\mathbf{e}_\sigma,$$

$$\Gamma_{\alpha\beta}^\sigma = g^{\sigma\tau}\Gamma_{\tau,\alpha\beta} = \frac{1}{2}g^{\sigma\tau}\left(\frac{\partial g_{\tau\beta}}{\partial q^\alpha} + \frac{\partial g_{\tau\alpha}}{\partial q^\beta} - \frac{\partial g_{\alpha\beta}}{\partial q^\tau}\right), \qquad (7)$$

$$\sigma, \tau = 1, 2, ..., s, \quad \alpha, \beta = 0, 1, ..., s, \quad \kappa = 1, 2, ..., k.$$

Here, $\mathbf{e}_\sigma$ and $\mathbf{e}^\sigma$ are the vectors of the principal basis and the mutual basis of the tangent space, respectively.

2. Composing a close set of differential equations with respect to the functions $q^\sigma(t)$ and $\Lambda_\kappa(t)$. It follows from expressions (6) and (7) that

$$\ddot{q}^\sigma = F_2^\sigma(t, q, \dot{q}, \Lambda),$$

$$F_2^\sigma = -\Gamma_{\alpha\beta}^\sigma \dot{q}^\alpha \dot{q}^\beta + (Q_\tau + \Lambda_\kappa b_\tau^\kappa)\frac{g^{\sigma\tau}}{M}, \qquad (8)$$

$$\sigma, \tau = 1, 2, ..., s, \quad \alpha, \beta = 0, 1, ..., s, \quad \kappa = 1, 2, ..., k.$$

Initially, we consider the case with $n = 3$. Using formulas (7) and taking into account that

$$\dot{\mathbf{e}}_\tau = \Gamma_{\tau\alpha}^\alpha \dot{q}^\alpha \mathbf{e}_\sigma, \quad \sigma, \tau = 1, 2, ..., s,$$

$$\alpha = 0, 1, ..., s$$

we write out the set of Eqs. (2) in the vector form:

$$\mathbf{a}_3^\kappa \cdot \dot{\mathbf{W}} = \chi_3^\kappa(t, q, \dot{q}, \ddot{q}), \quad \mathbf{a}_3^\kappa = a_{3\sigma}^\kappa \mathbf{e}^\sigma,$$

$$\chi_3^\kappa = -a_{30}^\kappa + a_{3\sigma}^\kappa\left(\frac{d}{dt}(\Gamma_{\alpha\beta}^\sigma \dot{q}^\alpha \dot{q}^\beta)\right.$$

$$\left. + (\ddot{q}^\tau + \Gamma_{\alpha\beta}^\tau \dot{q}^\alpha \dot{q}^\beta)\Gamma_{\tau\alpha}^\sigma \dot{q}^\alpha\right), \qquad (9)$$

$$\sigma, \tau = 1, 2, ..., s, \quad \alpha, \beta = 0, 1, ..., s, \quad \kappa = 1, 2, ..., k.$$

Differentiating Eq. (6) with respect to time, we obtain

$$M\dot{\mathbf{W}} = \dot{\mathbf{Y}} + \dot{\Lambda}_\kappa \mathbf{b}^\kappa + \Lambda_\kappa \dot{\mathbf{b}}^\kappa, \qquad (10)$$

where

$$\dot{\mathbf{Y}} = (\dot{Q}_\tau - Q_\sigma \Gamma_{\tau\alpha}^\sigma \dot{q}^\alpha)\mathbf{e}^\tau,$$

$$\dot{\mathbf{b}}^\kappa = (\dot{b}_\tau^\kappa - b_\sigma^\kappa \Gamma_{\tau\alpha}^\sigma \dot{q}^\alpha)\mathbf{e}^\tau,$$

$$\sigma, \tau = 1, 2, ..., s, \quad \alpha = 0, 1, ..., s, \quad \kappa = 1, 2, ..., k.$$

Taking the scalar product of Eq. (10) and the vectors $\mathbf{a}_3^\mu$, we find, with allowance for expressions (9),

$$\dot{\Lambda}_\kappa h_3^{\kappa\mu} = B_3^\mu(t, q, \dot{q}, \ddot{q}, \Lambda),$$

$$B_3^\mu = M\chi_3^\mu - \dot{\mathbf{Y}} \cdot \mathbf{a}_3^\mu - \Lambda_\kappa \dot{\mathbf{b}}^\kappa \cdot \mathbf{a}_3^\mu,$$

$$h_3^{\kappa\mu} = \mathbf{a}_3^\mu \cdot \mathbf{b}^\kappa = a_{3\sigma}^\mu b_\tau^\kappa g^{\sigma\tau},$$

$$\sigma, \tau = 1, 2, ..., s, \quad \kappa, \mu = 1, 2, ..., k.$$

By assumption, condition (4) is considered to be fulfilled. Hence, it follows that

$$\dot{\Lambda}_\kappa = h_{\kappa\mu}^3(t, q, \dot{q}, \ddot{q})B_3^\mu(t, q, \dot{q}, \ddot{q}, \Lambda), \qquad (11)$$

$$\kappa, \mu = 1, 2, ..., k.$$

Here, $h_{\kappa\mu}^3$ are the elements of the matrix reciprocal with respect to the matrix having elements $h_3^{\kappa\mu}$. Formulas (8) allow us to exclude the derivatives $\ddot{q}^\sigma$ from the functions $h_{\kappa\mu}^3$ and B_3^μ and to present the right-hand sides of equations (11) in the form

$$\dot{\Lambda}_\kappa = C_\kappa^3(t, q, \dot{q}, \Lambda), \quad \kappa = 1, 2, ..., k. \qquad (12)$$

For an arbitrary n, there appear the functions $h_{\kappa\mu}^n$ and B_n^μ, from which the exclusion of the derivatives $\ddot{q}^\sigma, ..., \overset{(n-1)}{q}^\sigma$ is required. From expressions (8), it follows that

$$\dddot{q}^\sigma = \frac{\partial F_2^\sigma}{\partial t} + \frac{\partial F_2^\sigma}{\partial q^\tau}\dot{q}^\tau + \frac{\partial F_2^\sigma}{\partial \dot{q}^\tau}\ddot{q}^\tau + \frac{\partial F_2^\sigma}{\partial \Lambda_\kappa}\dot{\Lambda}_\kappa, \qquad (13)$$

$$\sigma, \tau = 1, 2, ..., s, \quad \kappa = 1, 2, ..., k.$$

Formulas (8) make it possible to eliminate the derivatives $\ddot{q}^\tau$ from expressions (13) and write them out in the form

$$\dddot{q}^\sigma = F_3^\sigma(t, q, \dot{q}, \Lambda, \dot{\Lambda}), \quad \sigma = 1, 2, ..., s.$$

Using a similar line of reasoning, we obtain

$$\overset{(n-1)}{q}^\sigma = F_{n-1}^\sigma(t, q, \dot{q}, \Lambda, \dot{\Lambda}, ..., \overset{(n-3)}{\Lambda}),$$

$$\sigma = 1, 2, ..., s.$$

Thus, we have, in the general case,

$$\overset{(n-2)}{\Lambda}_\kappa = C_\kappa^n(t, q, \dot{q}, \Lambda, \dot{\Lambda}, ..., \overset{(n-3)}{\Lambda}), \qquad (14)$$

$$\kappa = 1, 2, ..., k, \quad n \geq 3.$$

A specific example of these equations is set (12).

Equations (8) and (14) form the set of equations closed with respect to the functions $q^\sigma(t)$ and $\Lambda_\kappa(t)$. For

initial data (3) and (5), this set has a unique solution which proves the statement.

Note that if the differential equation which the motion must obey depends nonlinearly on higher derivatives $\overset{(n-1)}{q}\vphantom{q}^{\sigma}$, then, differentiating this equation with respect to time, we arrive at an equation depending linearly on the derivatives $\overset{(n)}{q}\vphantom{q}^{\sigma}$. Consequently, the theory proposed can also be used for cases of nonlinear constraints of highest orders.

3. Mixed problem of dynamics and the principle of least constraint. The solution constructed for the mixed problem of dynamics depends substantially on the set of vectors $\mathbf{b}^{\kappa}$ over which the desired force $\mathbf{R}(t)$ is decomposed. We consider a particular case when the coefficients $a_{n\sigma}^{\kappa}$ in Eq. (2) are the functions of only the variables t, q, $\dot{q}$. In this case, it follows from Eqs. (9) that

$$\mathbf{a}_3^{\kappa} \cdot \mathbf{W} = \mathbf{a}_3^{\kappa} \cdot \mathbf{W}\big|_{t=t_0} + \int_{t_0}^{t}(\chi_3^{\kappa} + \dot{\mathbf{a}}_3^{\kappa} \cdot \mathbf{W})dt, \tag{15}$$

$$\kappa = 1, 2, \ldots, k.$$

For fixed values of the variables t, q, and $\dot{q}$, this system of equations in the acceleration space $\mathbf{W}$ presets the set of accelerations $\mathbf{W}$, which is admitted by Eqs. (2) at $n = 3$. This set represents the $(s - k)$-dimensional plane in the acceleration space for both $n = 3$ and arbitrary n. To fulfill the program of motion (2), the end of the vector $\mathbf{W}$ must lie in this plane. As follows from Eq. (6), the vector $\mathbf{W}$ can be obtained by adding the desired vector $\dfrac{\Lambda_{\kappa}\mathbf{b}^{\kappa}}{M}$ to the vector $\dfrac{\mathbf{Y}}{M}$. If the control is such that $\mathbf{b}^{\kappa} = \mathbf{a}_n^{\kappa}$, $\kappa = 1, 2, \ldots, k$, and $k < s$, the modulus of the vector $\dfrac{\Lambda_{\kappa}\mathbf{b}^{\kappa}}{M}$ is equal to the shortest distance between the point $\dfrac{\mathbf{Y}}{M}$ and the given plane. Thus, for $b_{\sigma}^{\kappa} = a_{n\sigma}^{\kappa}$, $\sigma = 1, 2, \ldots, s$, $\kappa = 1, 2, \ldots, k$, and $k < s$ control is realized in accordance with the principle of least constraint according to which measure of constraint must be least in the case under study:

$$Z_g = \frac{\tau^4}{4}M\left(\mathbf{W} - \frac{\mathbf{Y}}{M}\right)^2.$$

Here, τ is the infinitely small time interval entering into the formulation of this principle.

We now consider the case when the equations for the motion program are given in the form of a set of differential equations of the zero, first, and second orders; in the last case, they are linearly dependent on acceleration. Differentiating these equations three times, two times, or one time, respectively, we arrive at a set of equations which can be written in form (2) for $n = 3$. In this case, the right-hand sides of Eqs. (15) can be represented in the form of functions of the variables t, q, and $\dot{q}$ [5]. Therefore, the components Λ_{κ} of the vector $\dfrac{\Lambda_{\kappa}\mathbf{b}^{\kappa}}{M}$ connecting the point $\dfrac{\mathbf{Y}}{M}$ with the $(s - k)$-dimensional plane given by Eqs. (15) can also be found as functions of the same variables. Consequently, having given initial data (5) coordinated with the program of motion, we can also determine the initial values Λ_{κ}^0 of the control forces.

Thus, the set of Eqs. (8) and (12) can also be used for determining the control forces $\Lambda_{\kappa}(t)$ in the case when the program of motion is given in the form of constraint equations on the order of $n < 3$. The control for which the principle of least constraint holds true we refer to as *perfect*. Note that this definition of the perfect control for constraints on the order of $n < 3$ can be written in the form of the d'Alembert–Lagrange principle [5].

REFERENCES

1. M. A. Chuev, Izv. Vyssh. Uchebn. Zaved., Mashinostr., No. 8, 165 (1974).

2. N. N. Polyakhov, S. A. Zegzhda, and M. P. Yushkov, Dokl. Akad. Nauk SSSR **269**, 1328 (1983).

3. N. N. Polyakhov, S. A. Zegzhda, and M. P. Yushkov, Vestn. Leningr. Univ., No. 1, 73 (1984).

4. P. I. Ostromenskiĭ and A. I. Rodionov, Nauchn. Vest. NGTU, No. 3, 121 (1997).

5. S. A. Zegzhda, N. G. Filippov, and M. P. Yushkov, Vest. St. Petersburg. Univ., Ser. 1 **3** (15), 75 (1998).

6. S. A. Zegzhda, N. G. Filippov, and M. P. Yushkov, Vest. St. Petersburg. Univ., Ser. 1, No. 4 (22), 89 (1998).

Translated by V. Bukhanov

================= **MECHANICS** =================

Application of Differential Constraints to the Analysis of Turbulence Models

V. N. Grebenev and B. B. Ilyushin

Presented by Academician Yu.I. Shokin January 14, 2000

To separate out classes of solutions to systems of differential equations, Yanenko [1, 2] proposed the method of differential constraints, providing an opportunity to find gradient-type relations involving the desired functions while being consistent with the initial system. He demonstrated that this approach can be used to construct and justify the closure procedure for moment equations in the theory of turbulence.

The available models of turbulence using the second-order closure (for example, the K–ϵ model) include gradient-type parameterizations of the third moments, which are based on a phenomenological approach. When turbulent pulsations in a flow are highly anisotropic (for example, in a stratified flow), these models turn out to be insufficient and the models involving the closure of higher order are used. The method of closure of higher-order moments, which ensures physically reasonable (satisfying the Schwartz inequality) behavior of statistical moments of turbulent pulsations, is formulated in [3]. Its efficiency for different types of turbulent flows is also shown. This method includes obtaining approximate algebraic parameterizations for higher-order moments. We note that no rigorous justification of the proposed approach can be found in the literature. This problem is discussed in the present paper. Discussion is based on the classical problem of the theory of free turbulent flows concerning the development of a shear-free mixing layer.

In this paper, we prove the existence of a parametric family of self-similar solutions and determine the differential constraints for the formulated approximate model with the third-order closure for the shear-free mixing layer. It is established that the algebraic expression for triple correlations (the differential constraint of the model) coincides with the tensor invariant model obtained in [4].

1. Model of turbulent transfer in the mixing layer. The following system of averaged equations is

Institute of Computer Science, Siberian Division,
Russian Academy of Sciences, pr. Akademika Lavrent'eva 6,
Novosibirsk, 600090 Russia

used to describe a shear-free mixing layer between flows having different scales of turbulence:

$$\frac{\partial e_h}{\partial t} = -\frac{\partial \langle e_h w \rangle}{\partial z} - \frac{c_1}{\tau}\left[e_h - \frac{2}{3}E\right] - \frac{2}{3}\epsilon,$$

$$\frac{\partial \epsilon}{\partial t} = \frac{\partial}{\partial z}\left[c_d \tau \langle w^2 \rangle \frac{\partial \epsilon}{\partial z}\right] + \frac{c_{\epsilon_1}}{\tau}\beta g \langle w\theta \rangle - c_{\epsilon_2}\frac{\epsilon}{\tau},$$

$$\frac{\partial \langle w^2 \rangle}{\partial t} = -\frac{\partial \langle w^3 \rangle}{\partial z} + 2\beta g \langle w\theta \rangle$$

$$- \frac{c_1}{\tau}\left[\langle w^2 \rangle - \frac{2}{3}E\right] - \frac{2}{3}\epsilon.$$

Without shear of the average velocity, the horizontal components are assumed to be equal and $e_h = (\langle u^2 \rangle + \langle v^2 \rangle)/2$. According to our notation, w is the fluctuation of the vertical velocity component, $\langle w^2 \rangle$ is the second-order single-point correlation of the fluctuations of the vertical velocity component, $\tau = E/\epsilon$ is the time scale of turbulence, E is the kinetic energy of turbulence, ϵ is the spectral flux of the kinetic energy in the turbulent flow, $\beta = 1/\Theta$ is the coefficient of volume expansion, Θ and θ are the average and fluctuating potential temperatures, g is the acceleration of gravity, c with subscripts are the coefficients of the model, and the angular brackets $\langle \cdot \rangle$ denote averaging. The system is supplemented by the transport equation for triple correlation of vertical velocity fluctuations

$$\frac{\partial \langle w^3 \rangle}{\partial t} = -\frac{\partial C}{\partial z} - 3\langle w^2 \rangle \frac{\partial \langle w^2 \rangle}{\partial z}$$

$$+ 3\beta g \langle w^2\theta \rangle - c_2\frac{\langle w^3 \rangle}{\tau}.$$

For the forth-order cumulant C, the triple correlation $\langle w^2\theta \rangle$ and the vertical heat flux $\langle w\theta \rangle$ algebraic parameterizations are written as [5]

$$C = -\frac{\tau}{c_3}\left[6\langle w^3 \rangle \frac{\partial \langle w^2 \rangle}{\partial z} + 4\langle w^2 \rangle \frac{\partial \langle w^3 \rangle}{\partial z}\right],$$

$$\langle w^2\theta\rangle = -\frac{\tau}{c_4}\left[\langle w^3\rangle\frac{\partial\Theta}{\partial z} - 2\beta g\langle w\theta^2\rangle\right],$$

$$\langle w\theta^2\rangle = -\frac{\tau}{c_5}\langle w^2\rangle\frac{\partial\langle\theta^2\rangle}{\partial z},$$

$$\langle w\theta\rangle = -\frac{\tau}{c_{\theta_1}}\langle w^2\rangle\frac{\partial\Theta}{\partial z} \equiv -\frac{\tau N^2}{\beta g c_{\theta_1}}\langle w^2\rangle,$$

$$N^2 = \beta g\frac{\partial\Theta}{\partial z},$$

$$\langle\theta^2\rangle = -\frac{\tau}{c_r}\langle w\theta\rangle\frac{\partial\Theta}{\partial z} = -\frac{\tau N^2}{\beta g r}\langle w\theta\rangle$$

$$= \left(\frac{\tau N^2}{\beta g}\right)^2\frac{\langle w^2\rangle}{c_{\theta_1}r},$$

where $r = \tau/\tau_\theta$, τ_θ is the time scale for the fluctuating component of the potential temperature and N is the Brunt–Väisälä frequency. In the approximation of balance between the exchange mechanism and dissipation, the equation for the kinetic energy of turbulence in the horizontal direction is reduced to the following algebraic equation:

$$-c_1\left[e_h - \frac{2}{3}\left(e_h + \frac{\langle w^2\rangle}{2}\right)\right] = \frac{2}{3}\left(e_h + \frac{\langle w^2\rangle}{2}\right).$$

As a result,

$$e_h = \frac{c_1-1}{c_1+2}\langle w^2\rangle, \quad E = \frac{3c_1}{2(c_1+2)}\langle w^2\rangle,$$

$$\tau = \frac{3c_1}{2(c_1+2)}\frac{\langle w^2\rangle}{\epsilon}.$$

Using the expressions derived for an unstratified fluid, we can rewrite the equations as follows:

$$\frac{\partial\langle w^2\rangle}{\partial t} = -\frac{\partial\langle w^3\rangle}{\partial z} - \frac{c_1}{c_1+2}\frac{\langle w^2\rangle}{\tau},$$

$$\frac{\partial\epsilon}{\partial t} = \frac{\partial}{\partial z}\left[c_d\tau\langle w^2\rangle\frac{\partial\epsilon}{\partial z}\right] - c_{\epsilon_2}\frac{\epsilon}{\tau},$$

$$\frac{\partial\langle w^3\rangle}{\partial t} = \frac{\partial}{\partial z}\left[\frac{\tau}{c_3}\left(6\langle w^3\rangle\frac{\partial\langle w^2\rangle}{\partial z} + 4\langle w^2\rangle\frac{\partial\langle w^3\rangle}{\partial z}\right)\right]$$

$$- 3\langle w^2\rangle\frac{\partial\langle w^2\rangle}{\partial z} - c_2\frac{\langle w^3\rangle}{\tau}.$$

The second term is dominant in the model of cumulant C [5]. Thus, the model equations take the form

$$\frac{\partial\langle w^2\rangle}{\partial t} = -\frac{\partial\langle w^3\rangle}{\partial z} - \frac{c_1}{c_1+2}\frac{\langle w^2\rangle}{\tau}, \quad (1.1)$$

$$\frac{\partial\langle w^3\rangle}{\partial t} = \frac{\partial}{\partial z}\left[\frac{\tau}{c_3}4\langle w^2\rangle\frac{\partial\langle w^3\rangle}{\partial z}\right]$$

$$- 3\langle w^2\rangle\frac{\partial\langle w^2\rangle}{\partial z} - c_2\frac{\langle w^3\rangle}{\tau}, \quad (1.2)$$

$$\frac{\partial\epsilon}{\partial t} = \frac{\partial}{\partial z}\left[c_d\tau\langle w^2\rangle\frac{\partial\epsilon}{\partial z}\right] - c_{\epsilon_2}\frac{\epsilon}{\tau}. \quad (1.3)$$

2. Nonlinear eigenvalue problem. Self-similar variables should be chosen taking into account that a midpoint of the profile, for instance, z_0, shifts toward less intense turbulence with the growth of t. This feature of the process and the imperfect self-similarity [6] of the problem under consideration imply that distributions of the turbulence energy, of second- and third-order correlations of longitudinal velocity fluctuations, and the characteristic half-width L take the form [7]

$$\epsilon_a = \frac{d^{3\mu+\nu}h(\xi)}{m^{\nu/\mu+3}(t+t_0)^{3\mu+\nu}},$$

$$\langle w_a^2\rangle = \frac{d^{2\mu}f(\xi)}{m^2(t+t_0)^{2\mu}}, \quad \langle w_a^3\rangle = \frac{d^{3\mu}q(\xi)}{m^3(t+t_0)^{3\mu}}, \quad (2.1)$$

$$\xi = \frac{z-z_0}{L}, \quad L = \frac{\lambda}{d^\nu}(t+t_0)^\nu,$$

$$z_0 = \lambda_0 L + \lambda_1, \quad t_0 > 0,$$

where m, d, λ, and λ_i are positive quantities and parameters μ and ν should be determined simultaneously with f, h, and q. Considering a nonlinear eigenvalue problem for profiles f, h, and q, we choose the Dirichlet boundary conditions. The system of equations is reduced to the form free of independent variable ξ, and the order of the equations decreases. The complete analysis of behavior of integral curves corresponding to the derived system is rather complicated. For the simpler K–ϵ model, this problem was partly solved in [8].

3. Existence of a self-similar solution. Solutions to the nonlinear eigenvalue problem are sought as steady states of a certain evolutionary system. We shall start to derive it from the analysis of $\tilde\tau = \langle w^2\rangle/\epsilon$. Calculating the derivative with respect to variable t, we find

$$\frac{\partial\tilde\tau}{\partial t} = \frac{1}{\epsilon}\frac{\partial\langle w^2\rangle}{\partial t} - \frac{\langle w^2\rangle}{\epsilon^2}\frac{\partial\epsilon}{\partial t}$$

$$= -\frac{1}{\epsilon}\frac{\partial\langle w^3\rangle}{\partial z} - \alpha - \delta\tilde\tau^2\frac{\partial^2\langle w^2\rangle}{\partial z^2} + \delta\langle w^2\rangle\tilde\tau\frac{\partial^2\tilde\tau}{\partial z^2}$$

$$- \delta\frac{\tilde\tau^2}{\langle w^2\rangle}\left(\frac{\partial\langle w^2\rangle}{\partial z}\right)^2 + \rho.$$

Thus, the equation for $\tilde{\tau}$ takes the form

$$\frac{\partial \tilde{\tau}}{\partial t} = \delta \langle w^2 \rangle \tilde{\tau} \frac{\partial^2 \tilde{\tau}}{\partial z^2} - \frac{\tilde{\tau}}{\langle w^2 \rangle} \left[\frac{\partial \langle w^3 \rangle}{\partial z} \right.$$

$$\left. + \delta \tilde{\tau} \langle w^2 \rangle \frac{\partial^2 \langle w^2 \rangle}{\partial z^2} + \delta \tilde{\tau} \left(\frac{\partial \langle w^2 \rangle}{\partial z} \right)^2 \right] - \alpha + \rho.$$

Parameters of the model (α, κ, γ, δ, and ρ) are positive constants which are combinations of constants of model (1.1)–(1.3). Taking into account the structure of (2.1), we introduce the following self-similar processing [9] of $\langle w^2 \rangle$, $\langle w^3 \rangle$, ϵ, and $\tilde{\tau}$:

$$\varpi(\xi, \theta) = (t + t_0)^{2\mu} \langle w^2(z, t) \rangle,$$

$$\chi(\xi, \theta) = (t + t_0)^{3\mu} \langle w^3(z, t) \rangle,$$

$$u(\xi, \theta) = (t + t_0)^{2\mu + 1} \epsilon(z, t),$$

$$w(\xi, \theta) = (t + t_0)^{-1} \tilde{\tau}(z, t),$$

where, without loss of generality, d, m, λ, and λ_i are set equal to unity and $\theta = \ln(t + t_0)$ is the new evolutionary variable. This leads to the following system of equations for u, w, and χ:

$$\frac{\partial u}{\partial \theta} = \delta \frac{\partial}{\partial \xi} \left(w^2 u \frac{\partial u}{\partial \xi} \right) + (1 - \mu)(\xi + 1) \frac{\partial u}{\partial \xi}$$

$$+ (2\mu + 1)u - \rho \frac{u}{w}, \tag{3.1}$$

$$\frac{\partial w}{\partial \theta} = \delta \varpi w \frac{\partial^2 w}{\partial \xi^2} + (1 - \mu)(\xi + 1) \frac{\partial w}{\partial \xi}$$

$$- \frac{w}{\varpi} \left[\frac{\partial \chi}{\partial \xi} + \delta \varpi w \frac{\partial^2 \varpi}{\partial \xi^2} + \delta w \left(\frac{\partial \varpi}{\partial \xi} \right)^2 \right] - w - \alpha + \rho, \tag{3.2}$$

$$\frac{\partial \chi}{\partial \theta} = \kappa \frac{\partial}{\partial \xi} \left(w^2 u \frac{\partial \chi}{\partial \xi} \right) - 3 \varpi \frac{\partial \varpi}{\partial \xi}$$

$$+ (1 - \mu)(\xi + 1) \frac{\partial \chi}{\partial \xi} - \gamma \frac{\chi}{w} + 3\mu \chi. \tag{3.3}$$

The equation for ϖ has the form

$$\frac{\partial \varpi}{\partial \theta} = -\frac{\partial \chi}{\partial \xi} + (1 - \mu)(\xi + 1) \varpi_\xi + 2\mu \varpi - \alpha u. \tag{3.4}$$

Steady states of system (3.1)–(3.3) are determined by solutions to the corresponding system of nonlinear ordinary differential equations.

Taking into account (3.4), we find from (3.1)–(3.3) that the functions $u_s(\xi)$, $w_s(\xi)$, and $\chi_s(\xi)$ satisfying the relationships

$$w_s = \frac{\rho}{2\mu + 1} \equiv \rho - \alpha, \quad \mu = \frac{\alpha}{2(\rho - \alpha)}, \tag{3.5}$$

$$\delta(w_s^2 u_s u_{s\xi})_\xi + (1 - \mu)(\xi + 1)u_{s\xi} = 0, \tag{3.6}$$

$$\chi_s = -\delta w_s \varpi \varpi_\xi, \tag{3.7}$$

are steady states of (3.1)–(3.3) at

$$\kappa = \delta, \quad \delta = \frac{3}{\rho - \gamma}, \quad \gamma = \frac{3}{2}\alpha, \quad \rho - \gamma > 0. \tag{3.8}$$

Starting from the formulation of the problem, we find for u_s that

$$u_s(-\infty) = a_- t_0^{2\mu + 1}, \quad u_s(+\infty) = a_+ t_0^{2\mu + 1}, \tag{3.9}$$

where $a_\pm = \lim_{z \to \pm\infty} \epsilon(z, 0)$, $a_\pm > 0$..

Numerical methods were used in [10] to solve the Cauchy problem for Eq. (3.6). At zero boundary conditions, equations of such a form were studied in [11] in connection to self-similar solutions to the equation of motion for gas (liquid) in a porous medium. The analysis carried out for integral curves of the equation also demonstrates the existence of the solutions belonging to the class of positive functions. We shall analyze this class of solutions in detail for the boundary-value problem (3.6), (3.9). The following theorem is valid:

Theorem 3.1. *For any positive finite numbers* a_- *and* a_+ *(*$a_- \leq a_+$*), there exists a value of parameter* t_0 *such that the boundary-value problem (3.6), (3.9) has a unique positive monotonically increasing solution.*

Having determined u_s, we calculate ϵ_a according to the formula

$$\epsilon_a(z, t) = \frac{u_s(\xi)}{(t + t_0)^{2\mu + 1}};$$

and for $\langle w_a^2 \rangle$, we have

$$\langle w_a^2 \rangle = \epsilon_a v = (\rho - \alpha)(t + t_0)\epsilon_a.$$

To determine $\langle w_a^3 \rangle$, we use expression (3.7), which yields

$$\langle w_a^3 \rangle = -\delta \tilde{\tau} \langle w_a^2 \rangle \langle w_a^2 \rangle_\xi, \quad \tilde{\tau} = (\rho - \alpha)(t + t_0). \tag{3.10}$$

The calculations, which take into account (3.8) and the above-formulated assumptions for d, m, λ, and λ_i, show that the differential equation for $\langle w_a^3 \rangle$ is satisfied identically.

Theorem 3.2. *Let* $\rho - \gamma > 0$ *and conditions (3.8) for parameters of the model hold. Then, there exists a self-similar solution* $\langle w_a^2 \rangle$, $\langle w_a^3 \rangle$, ϵ_a *to system (1.1)–(1.3) such that* $\langle w_a^3 \rangle$ *satisfies the algebraic model (3.10).*

Remark 3.1. *Relation (3.10) coincides with the tensor-invariant model obtained in [4].*

Let us consider the equation

$$\langle w^3 \rangle_z = -\delta \tilde{\tau} \langle w^2 \rangle \langle w^2 \rangle_{zz} - \delta \tilde{\tau} \langle w^2 \rangle_z^2 \qquad (3.11)$$

written in variables (z, t). We then supplement two differential constraints $\tilde{\tau}_z = 0$ and (3.11) into system (1.1)–(1.3). This leads to an overdetermined system which has a solution concordant with Theorem 3.2. In other words, the self-similar solution $\langle w_a^2 \rangle$, $\langle w_a^3 \rangle$, ϵ_a is a particular solution to the overdetermined system, whereas algebraic relationship (3.10) is interpreted in the framework of the method of differential constraints. The method of differential constraints [2] can be applied to separate out other classes of solutions and to derive algebraic relationships useful for numerical simulations of statistical characteristics.

ACKNOWLEDGMENTS

REFERENCES

1. N. N. Yanenko, in *Proceedings of IV All-Union Mathematical Conference* (Nauka, Leningrad, 1964), Vol. 2.
2. A. F. Sidorov, V. P. Shapeev, and N. N. Yanenko, *Methods of Differential Relations and Its Application in Gas Dynamics* (Nauka, Novosibirsk, 1984).
3. B. B. Ilyushin, in *Closure Strategies for Turbulent and Transition Flows* (Cambridge Univ. Press, Cambridge, 1999).
4. K. Hanjalic and B. E. Launder, J. Fluid Mech. **52**, 609 (1972).
5. B. B. Ilyushin, Prikl. Mekh. Tekh. Fiz. **40** (5), 106 (1999).
6. G. I. Barenblatt, *Cambridge Texts in Applied Mathematics*, Vol. 14: *Sealing, Self-Similarity, and Intermediate Asymptotics* (Cambridge Univ. Press, Cambridge, 1996).
7. N. V. Aleksenko, V. I. Bukreev, and V. A. Kostomakha, Prikl. Mekh. Tekh. Fiz., No. 1 (149), 57 (1985).
8. J. Hulshof, J. Math. Anal. Appl. **28** (1), 33 (1997).
9. A. A. Samarskii, V. A. Galaktionov, S. P. Kurdumov, and A. P. Mikhailov, *Blow-up in Quasilinear Parabolic Equations* (Walter de Gruyter, Berlin, 1995).
10. P. Ya. Polubarinova-Kochina, Dokl. Akad. Nauk SSSR **63**, 623 (1948).
11. G. I. Barenblatt, Prikl. Mat. Mekh. **16**, 67 (1952).

Translated by Yu. Verevochkin

═══════════════ **MECHANICS** ═══════════════

Semi-Inverse Solutions Leading to Two-Dimensional Boundary Value Problems in Nonlinear Elasticity Theory

L. M. Zubov

Presented by Academician I.I. Vorovich January 17, 2000

Received January 28, 2000

In this study, we apply the semi-inverse method for solving static problems of nonlinear elasticity theory. Under the semi-inverse method, we understand procedures of constructing such particular solutions for which the initial set of equations is reduced to equations with a smaller number of independent variables. The semi-inverse solutions to static and quasistatic problems related to large strains of continuum, which involve unknown functions of only one spatial variable, were constructed in [1, 2]. Below, we find several two-parametric families for final strains of an isotropic elastic body for which the set of three-dimensional equations of equilibrium is reduced to a set with two independent variables. The semi-inverse solutions obtained make it possible to reduce to two-dimensional boundary value problems a number of spatial problems in nonlinear elasticity theory for the bending and torsion of prismatic bodies, as well as for curved bars having the shape of a sector of an axisymmetric body.

In the absence of mass forces, the set of equations of the elastostatics for an isotropic homogeneous body involves the equilibrium equations for the Piola stress tensor $\mathbf{D}$ [3],

$$\operatorname{div}\mathbf{D} = 0, \tag{1}$$

the equations of state

$$\mathbf{D} = (a_0\mathbf{E} + a_1\mathbf{G} + a_{-1}\mathbf{G}^{-1}) \cdot \mathbf{C},$$
$$a_m = a_m(I_1, I_2, I_3),$$
$$m = -1, 0, 1; \quad I_1 = \operatorname{tr}\mathbf{G}, \tag{2}$$
$$I_2 = \frac{1}{2}(\operatorname{tr}^2\mathbf{G} - \operatorname{tr}\mathbf{G}^2), \quad I_3 = \det\mathbf{G}$$

and the geometrical relationships

$$\mathbf{G} = \mathbf{C} \cdot \mathbf{C}^{\mathrm{T}}, \quad \mathbf{C} = \operatorname{grad}\mathbf{R}, \quad \mathbf{R} = X_k\mathbf{i}_k. \tag{3}$$

In (1)–(3), $\mathbf{C}$ is the strain gradient; X_k, $k = 1, 2, 3$, are the Cartesian coordinates of particles of the deformed body (Euler coordinates) and $\mathbf{G}$ is the Cauchy strain measure; I_1, I_2, and I_3 are the invariants of the tensor $\mathbf{G}$; a_m are certain functions of the invariants; $\mathbf{i}_k$ are the unit vectors of the coordinates; $\mathbf{E}$ is the unit tensor; and div and grad are the divergence operator and gradient operator in the Lagrangian coordinates. Furthermore, we use for these coordinates the Cartesian coordinates x_s, $x = 1, 2, 3$ for the body reference configuration and also the circular cylindrical coordinates r, φ, and z, which are connected with the Cartesian coordinates by the relationships

$$x_1 = r\cos\varphi, \quad x_2 = r\sin\varphi, \quad x_3 = z.$$

Set (1)–(3) can be easily reduced to a set of three scalar nonlinear equations with unknown functions X_1, X_2, X_3 and independent variables x_1, x_2, x_3. Below, we deal with the particular solutions to the set of Eqs. (1)–(3) containing unknown functions of only two Lagrangian coordinates. Each of these solutions represents a two-parametric family of strains described by the function $X_k = X_k(x_1, x_2, x_3)$ or $X_k = X_k(r, \varphi, z)$.

The first family is

$$X_1 = u_1(x_1, x_2)\cos\psi x_3 - u_2(x_1, x_2)\sin\psi x_3,$$
$$X_2 = u_1(x_1, x_2)\sin\psi x_3 + u_2(x_1, x_2)\cos\psi x_3, \tag{4}$$
$$X_3 = \lambda x_3 + w(x_1, x_2), \quad \lambda, \psi = \text{const.}$$

The family of strains (4), which was presented previously in [4] in the other form, describes the torsion and tension of a prismatic (cylindrical) body with the generatrix parallel to the x_3-axis. As a particular case ($\psi = 0$), formulas (4) contain the combination of the generalized plane strain and antiplane strain. The strain gradient corresponding to transformation (4) has the form (α, $\beta = 1, 2$)

$$\mathbf{C} = \frac{\partial X_k}{\partial x_s}\mathbf{i}_s\mathbf{i}_k = \frac{\partial u_\beta}{\partial x_\alpha}\mathbf{i}_\alpha\mathbf{e}_\beta + \frac{\partial w}{\partial x_\alpha}\mathbf{i}_\alpha\mathbf{e}_3$$
$$- \psi u_2\mathbf{i}_3\mathbf{e}_1 + \psi u_1\mathbf{i}_3\mathbf{e}_2 + \lambda\mathbf{i}_3\mathbf{e}_3,$$
$$\mathbf{e}_1 = \mathbf{i}_1\cos\psi x_3 + \mathbf{i}_2\sin\psi x_3, \tag{5}$$
$$\mathbf{e}_2 = -\mathbf{i}_1\sin\psi x_3 + \mathbf{i}_2\cos\psi x_3, \quad \mathbf{e}_3 = \mathbf{i}_3.$$

Rostov State University, pr. Stachki 194,
Rostov-on-Don, 344104 Russia

Since the vectors $\mathbf{e}_1$, $\mathbf{e}_2$, and $\mathbf{e}_3$ form an orthonormalized basis, the Cauchy strain measure $\mathbf{G}$ is independent of the x_3-coordinate. On the basis of (2) and (5), we conclude that the Piola stress tensor is represented as

$$\mathbf{D} = D_{sk}\mathbf{i}_s\mathbf{e}_k, \quad s, k = 1, 2, 3, \tag{6}$$

where the components D_{sk} are independent of x_3 and satisfy the equations of equilibrium,

$$\frac{\partial D_{11}}{\partial x_1} + \frac{\partial D_{21}}{\partial x_2} = \psi D_{32},$$

$$\frac{\partial D_{12}}{\partial x_1} + \frac{\partial D_{22}}{\partial x_2} = -\psi D_{31}, \quad \frac{\partial D_{13}}{\partial x_1} + \frac{\partial D_{23}}{\partial x_2} = 0, \tag{7}$$

which follow from (1) and (6).

Since the values D_{sk} are expressed in terms of the functions u_1, u_2, and w, relationships (7) represent the set of three equations with respect to the three functions of two variables. Thus, expressions (4) satisfy initial equilibrium Eqs. (1)–(3) with three independent variables, x_1, x_2, and x_3 if and only if the two-variable functions u_1, u_2, and w satisfy Eqs. (7).

If a distributed external load $\mathbf{f}$ is given on the lateral area of a prism with the unit normal $\mathbf{n} = n_1\mathbf{i}_1 + n_2\mathbf{i}_2$, then the boundary conditions on this surface have the form

$$\mathbf{n} \cdot \mathbf{D} = \mathbf{f}. \tag{8}$$

We assume that the vector $\mathbf{f}$ of the load can be represented in the form

$$\mathbf{f} = \mathbf{n} \cdot (b_0\mathbf{E} + b_1\mathbf{G} + b_2\mathbf{G}^2) \cdot \mathbf{C},$$

$$b_t = b_t(I_1, I_2, I_3, x_1, x_2), \quad t = 0, 1, 2. \tag{9}$$

In this case, boundary conditions (8) for the strain of type (4) contain no variable x_3. Together with Eqs. (7), they form the two-dimensional boundary value problem for a plane domain having the form of the cross section of a prism. Relationships (9) are true, for example, for the loading in the form of a uniformly distributed hydrostatic pressure. In the case of a prismatic bar with a finite length, the constants λ and ψ can be determined assuming that the longitudinal force and the torsional moment applied to the bar ends are given.

The second family is

$$X_1 = u(r, z)\sin\eta\varphi + v(r, z)\cos\eta\varphi,$$

$$X_2 = \kappa\varphi + w(r, z), \quad \kappa, \eta = \text{const}, \tag{10}$$

$$X_3 = u(r, z)\cos\eta\varphi - v(r, z)\sin\eta\varphi.$$

Formulas (10) describe the straightening and torsion of a curved bar having the shape of an annular sector (axisymmetric body) in the reference configuration. The deformation gradient and the Piola stress tensor have the form

$$\mathbf{C} = \frac{\partial v}{\partial r}\mathbf{g}_1\mathbf{h}_1 + \frac{\partial w}{\partial r}\mathbf{g}_1\mathbf{h}_2 + \frac{\partial u}{\partial r}\mathbf{g}_1\mathbf{h}_3 + \frac{\eta u}{r}\mathbf{g}_2\mathbf{h}_1$$

$$+ \frac{\kappa}{r}\mathbf{g}_2\mathbf{h}_2 - \frac{\eta v}{r}\mathbf{g}_2\mathbf{h}_3 + \frac{\partial v}{\partial z}\mathbf{g}_3\mathbf{h}_1 + \frac{\partial w}{\partial z}\mathbf{g}_3\mathbf{h}_2 + \frac{\partial u}{\partial z}\mathbf{g}_3\mathbf{h}_3,$$

$$\mathbf{D} = D_{sk}(r, z)\mathbf{g}_s\mathbf{h}_k,$$

$$\mathbf{g}_1 = \mathbf{i}_1\cos\varphi + \mathbf{i}_2\sin\varphi, \tag{11}$$

$$\mathbf{g}_2 = -\mathbf{i}_1\sin\varphi + \mathbf{i}_2\cos\varphi, \quad \mathbf{g}_3 = \mathbf{i}_3,$$

$$\mathbf{h}_1 = \mathbf{i}_1\cos\eta\varphi - \mathbf{i}_3\sin\eta\varphi,$$

$$\mathbf{h}_2 = \mathbf{i}_2, \quad \mathbf{h}_3 = \mathbf{i}_1\sin\eta\varphi + \mathbf{i}_3\cos\eta\varphi.$$

The components of the Cauchy deformation measure $\mathbf{G}$ in the basis $\mathbf{g}_1$, $\mathbf{g}_2$, and $\mathbf{g}_3$ are independent of the φ-coordinate. The functions of two variables u, v, and w are determined by solving the two-dimensional boundary value problem for the domain with the shape of the annular cross section, i.e., the cross section of the axisymmetric body by a plane passing through the x_3-axis. The indicated boundary value problem involves the equilibrium equations

$$\frac{\partial D_{11}}{\partial r} + \frac{\eta}{r}D_{23} + \frac{\partial D_{31}}{\partial z} = 0,$$

$$\frac{\partial D_{12}}{\partial r} + \frac{D_{12}}{r} + \frac{\partial D_{32}}{\partial z} = 0, \tag{12}$$

$$\frac{\partial D_{13}}{\partial r} + \frac{D_{13}}{r} - \frac{\eta}{r}D_{21} + \frac{\partial D_{33}}{\partial z} = 0$$

and the boundary conditions of form (8), (9) in which, now,

$$\mathbf{n} = n_1\mathbf{g}_1 + n_3\mathbf{g}_3, \quad b_t = b_t(I_1, I_2, I_3, r, z).$$

The third family is

$$X_1 = \rho(x_1, x_3)\cos[\omega x_2 + \beta(x_1, x_3)],$$

$$X_2 = \rho(x_1, x_3)\sin[\omega x_2 + \beta(x_1, x_3)], \tag{13}$$

$$X_3 = \alpha(x_1, x_3) + lx_2, \quad \omega, l = \text{const}.$$

Formulas (13) describe the spatial bending of the prismatic bar whose axis is parallel to the x_2-axis. On the basis of (2), (3), and (13), we find

$$\mathbf{C} = \frac{\partial\rho}{\partial x_1}\mathbf{i}_1\mathbf{k}_1 + \rho\frac{\partial\beta}{\partial x_1}\mathbf{i}_1\mathbf{k}_2 + \frac{\partial\alpha}{\partial x_1}\mathbf{i}_1\mathbf{k}_3 + \omega\rho\mathbf{i}_2\mathbf{k}_2$$

$$+ l\mathbf{i}_2\mathbf{k}_3 + \frac{\partial\rho}{\partial x_3}\mathbf{i}_3\mathbf{k}_1 + \rho\frac{\partial\beta}{\partial x_3}\mathbf{i}_3\mathbf{k}_2 + \frac{\partial\alpha}{\partial x_3}\mathbf{i}_3\mathbf{k}_3,$$

$$\mathbf{k}_1 = \mathbf{i}_1\cos\Phi + \mathbf{i}_2\sin\Phi,$$

$$\mathbf{k}_2 = -\mathbf{i}_1\sin\Phi + \mathbf{i}_2\cos\Phi, \quad \mathbf{k}_3 = \mathbf{i}_3, \tag{14}$$

$$\Phi = \omega x_2 + \beta(x_1, x_3),$$

$$\mathbf{G} = G_{mn}(x_1, x_3)\mathbf{i}_m\mathbf{i}_n, \quad \mathbf{D} = D_{mn}(x_1, x_3)\mathbf{i}_m\mathbf{k}_n.$$

In this case, the equilibrium equations and the boundary conditions on the lateral surface of the prism,

which form the two-dimensional boundary value problem with respect to the functions α, β, and ρ, have the following form:

$$\frac{\partial D_{11}}{\partial x_1} - \frac{\partial \beta}{\partial x_1} D_{12} - \omega D_{22} + \frac{\partial D_{31}}{\partial x_3} - \frac{\partial \beta}{\partial x_3} D_{32} = 0,$$

$$\frac{\partial \beta}{\partial x_1} D_{11} + \frac{\partial D_{12}}{\partial x_1} + \omega D_{21} + \frac{\partial \beta}{\partial x_3} D_{31} + \frac{\partial D_{32}}{\partial x_3} = 0, \quad (15)$$

$$\frac{\partial D_{13}}{\partial x_1} + \frac{\partial D_{33}}{\partial x_3} = 0,$$

$$n_1 D_{1m} + n_3 D_{3m} = \mathbf{f} \cdot \mathbf{k}_m,$$
$$n_s = \mathbf{n} \cdot \mathbf{i}_s, \quad m = 1, 2, 3. \quad (16)$$

An important particular case of semi-inverse solution (13) is the bending strain in the $x_1 x_2$-plane when $l = 0$, $\beta = 0$, and $\mathbf{f} \cdot \mathbf{k}_2 = 0$. In this case, according to (2) and (14), we have $D_{12} = D_{21} = D_{32} = D_{23} = 0$, as a result of which one of equations (15) and one of boundary conditions (16) are identically satisfied.

The fourth family is

$$X_1 = \sigma(r, z) \cos[\mu\varphi + \gamma(r, z)],$$

$$X_2 = \sigma(r, z) \sin[\mu\varphi + \gamma(r, z)], \quad (17)$$

$$X_3 = \tau(r, z) + \nu\varphi, \quad \mu, \nu = \text{const.}$$

Transformation of coordinates (17) corresponds to the spatial-bending strain of the annular sector and leads to the following expressions for the strain gradient, Cauchy strain measure, and Piola stress tensor:

$$\mathbf{C} = \frac{\partial \sigma}{\partial r}\mathbf{g}_1\mathbf{p}_1 + \frac{\partial \gamma}{\partial r}\sigma\mathbf{g}_1\mathbf{p}_2 + \frac{\partial \tau}{\partial r}\mathbf{g}_1\mathbf{p}_3 + \frac{\mu}{r}\sigma\mathbf{g}_2\mathbf{p}_2$$

$$+ \frac{\nu}{r}\mathbf{g}_2\mathbf{p}_3 + \frac{\partial \sigma}{\partial z}\mathbf{g}_3\mathbf{p}_1 + \frac{\partial \gamma}{\partial z}\sigma\mathbf{g}_3\mathbf{p}_2 + \frac{\partial \tau}{\partial z}\mathbf{g}_3\mathbf{p}_3,$$

$$\mathbf{p}_1 = \mathbf{i}_1 \cos\theta + \mathbf{i}_2 \sin\theta,$$

$$\mathbf{p}_2 = -\mathbf{i}_1 \sin\theta + \mathbf{i}_2 \cos\theta, \quad \mathbf{p}_3 = \mathbf{i}_3,$$

$$\theta = \mu\varphi + \gamma(r, z),$$

$$\mathbf{G} = G_{mn}(r, z)\mathbf{g}_m\mathbf{g}_n, \quad \mathbf{D} = D_{mn}(r, z)\mathbf{g}_m\mathbf{p}_n.$$

The boundary value problem for the functions σ, τ, and γ are written out in the form

$$\frac{\partial D_{11}}{\partial r} + \frac{D_{11} - \mu D_{22}}{r} - \frac{\partial \gamma}{\partial r} D_{12} + \frac{\partial D_{31}}{\partial z} - \frac{\partial \gamma}{\partial z} D_{32} = 0,$$

$$\frac{\partial D_{12}}{\partial r} + \frac{\partial \gamma}{\partial r} D_{11} + \frac{D_{12} + \mu D_{21}}{r} + \frac{\partial \gamma}{\partial z} D_{31} + \frac{\partial D_{32}}{\partial z} = 0,$$

$$\frac{\partial D_{13}}{\partial r} + \frac{D_{13}}{r} + \frac{\partial D_{33}}{\partial z} = 0, \quad (18)$$

$$n_1 D_{1m} + n_3 D_{3m} = \mathbf{f} \cdot \mathbf{p}_m,$$
$$n_k = \mathbf{n} \cdot \mathbf{g}_k, \quad m = 1, 2, 3. \quad (19)$$

For $\nu = 0$, $\gamma = 0$, and $\mathbf{f} \cdot \mathbf{p}_2 = 0$, with second equation in (18) and with boundary condition in (19) are identically satisfied for $m = 2$.

In conclusion, we note that the above semi-inverse solutions also remain valid in the quasistatic meaning for homogeneous isotropic inelastic (including elasto-plastic) bodies.

REFERENCES

1. A. Green and J. Adkins, *Large Elastic Deformation and Non-Linear Continuum Mechanics* (Clarendon Press, Oxford, 1960; Mir, Moscow, 1965).

2. L. M. Zubov, Dokl. Akad. Nauk SSSR **256**, 556 (1981) [Sov. Phys. Dokl. **26**, 111 (1981)].

3. A. I. Lur'e, *Nonlinear Elasticity Theory* (Nauka, Moscow, 1980).

4. L. M. Zubov, Dokl. Akad. Nauk SSSR **270**, 827 (1983) [Sov. Phys. Dokl. **28**, 512 (1983)].

Translated by V. Bukhanov

══════ **MECHANICS** ══════

The Uncertainty Principle Expressed in the Quantum-Mechanical Heisenberg Form for Automatic-Control Systems

S. A. Klimov and V. I. Tumarkin

Presented by Academician B.F. Bunkin October 25, 1999

Received October 28, 1999

In [1], the uncertainty principle for linear automatic-control systems (ACS) was formulated. In accordance with this principle, for a class of steady physically realizable and asymptotically stable ACS with a finite transmission band, the uncertainty function $\Phi(t, \omega)$ is defined (t and ω are, respectively, the current time and frequency). For this function, the size of the uncertainty body with dimensions 1 and 2 is constant and equal to 1 for an arbitrary pulse transition function $k(\tau)$ of the indicated class. This form of representation for the uncertainty principle, which was suggested by Woodward in the theory of signals, was later developed by a number of authors [2].

The goals of this paper are the formulation of the uncertainty principle for ACS in a significantly new form similar to that proposed by Heisenberg in quantum mechanics [3] and the proof of the equivalence of two indicated forms for ACS.

In order to solve the problem, we prove the following theorem:

Theorem 1. *Let* $L = L(t)$ *and* Δp *and* Δq *be the linear self-conjugate positive-definite operator,* L^{-1}, *its inverse operator, and the physical parameters, respectively, defined by the relations*

$$\int_0^\infty dt \frac{1}{2\pi} \int_{-\infty}^\infty [L\Phi(t, \omega)]^2 d\omega = \Delta p; \tag{1}$$

$$\int_0^\infty dt \frac{1}{2\pi} \int_{-\infty}^\infty [L^{-1}\Phi(t, \omega)]^2 d\omega = \Delta q. \tag{2}$$

Then,

$$\Delta p \cdot \Delta q \geq 1, \tag{3}$$

where Δp *and* Δq *are expressed in seconds* [s] *and reciprocal seconds* [s⁻¹], *respectively. Since the dimen-*

Al'fair State Research and Industrial Association, Aviamotornaya ul. 57, Moscow, 111024 Russia

sion of Δq *is* Hz, *then*

$$\Delta p \cdot \Delta q \geq \frac{1}{2\pi}; \tag{4}$$

i.e., (3) *acquires the standard form of the Heisenberg principle.*

In accordance with the property of the Woodward uncertainty function for ACS [1], we have

$$4\pi^2 = \left[\int_0^\infty dt \int_{-\infty}^\infty \Phi^2(t, \omega) d\omega \right]^2 = \left[\int_0^\infty a(t, \omega) b(t, \omega) d\omega \right]^2,$$

where $a(t, \omega) = L\Phi(t, \omega)$ and $b(t, \omega) = L^{-1}\Phi(t, \omega)$.

After two successive applications of the Bunyakowsky–Schwartz inequality to the last relationship, we arrive at (3) and (4).

Corollary. *Let* L *be the operator of multiplying by the time-dependent function* $f(t) > 0$, *which is integrable within the semiaxis* $(0, \infty)$.

Then (3) *and* (4) *take the form*

$$\Delta T \Delta \Omega \geq 1, \quad \Delta T \Delta F \geq 1/2\pi, \tag{5}$$

where

$$\Delta T = \Delta p = \int_0^\infty f^2(t) dt \frac{1}{2\pi} \int_{-\infty}^\infty \Phi^2(t, \omega) d\omega,$$

$$\Delta \Omega = \Delta q = \int_0^\infty f^{-2}(t) dt \frac{1}{2\pi} \int_{-\infty}^\infty \Phi^2(t, \omega) d\omega,$$

while

$$\frac{1}{2\pi} \int_{-\infty}^\infty \Phi^2(t, \omega) d\omega = \frac{1}{\Omega^2} \int_0^t k^2(\tau) k^2(t - \tau) dt$$

is the estimate for the signal-to-noise ratio and

$$\Omega = \int_0^\infty k^2(\tau) d\tau$$

is the effective transmission band.

If, for example, $f(t) = 2\sqrt{t}$, then relationship (5) exhibits the inequality for estimating attainable duration ΔT [s] of the transition process and the frequency band $\Delta\Omega$ [s^{-1}] or ΔF [Hz]:

$$\Delta T = \frac{2}{\Omega^2}\int_0^\infty t\,dt\int_0^t k^2(\tau)k^2(t-\tau)d\tau,$$

$$\Delta\Omega = \frac{1}{2\Omega^2}\int_0^\infty t^{-1}dt\int_0^t k^2(\tau)k^2(t-\tau)d\tau. \tag{6}$$

It is worth noting that, in [4], the duration of the process ΔT and the frequency band ΔF are bound by a relationship similar to (5). However, ΔT and $\Delta\Omega$ are given, in this case, in a manner which requires the difference between the orders of the numerator and the denominator of the transfer function corresponding to $k(\tau)$ to be no lower than 2. This requirement excludes, e.g., inertial links, astatic vibration links with astaticism of the second order, etc. Formulas (5) and (6) are free of this constraint and, by virtue of Theorem 1, are the corollaries of the uncertainty principle expressed, according to (6), in Woodward signal form.

Formulas (5) and (6) also hold true for unsteady $k(t, \tau)$ of the class indicated, but the parameter Ω^2 is changed by the parameter

$$\Omega_2^2 = \int_0^\infty dt\int_0^t k(t,\tau)k(t,t-\tau)d\tau.$$

The following theorem follows from formulas (3), (5) as well:

Theorem 2. *The constancy of the volume $\Phi(t, \omega)$ of the uncertainty body, i.e., the uncertainty principle in the Woodward form, follows from the relationship $\Delta p\Delta q \geq 1$.*

For the proof, it is sufficient to choose the unit operator for L. Then,

$$\Delta p\Delta q = \frac{1}{\Omega^4}\left[\int_0^\infty dt\int_0^t k^2(\tau)k^2(t-\tau)d\tau\right]^2$$

$$\leq \frac{1}{\Omega^4}\left[\int_0^\infty dt\int_0^\infty k^2(\tau)k^2(t-\tau)d\tau\right]^2.$$

From this, together with opposite inequality (3), the statement of Theorem 2 follows.

Corollary. *The expressions of the uncertainty principle for the* ACS *in the Woodward signal form and in the Heisenberg quantum-mechanical form are equivalent.*

We note also that if $L = L(\omega)$ and the action of the operator L is reduced to multiplication by the integrable squared function $\varphi(\omega)$ of the frequency ω in the region $(-\infty, \infty)$, then Δp and Δq are expressed similarly to (5).

However, in this case, $f^2(t)$ and $f^{-2}(t)$ are replaced by $\varphi^2(\omega)$ and $\varphi^{-2}(\omega)$, respectively, and integrals over t and ω are interchanged by their positions.

The expressions for ΔT and $\Delta\Omega$ can be generalized by using not the Bunyakowsky–Schwartz inequality, but the Hölder inequality:

$$\Delta\tilde{T}\Delta\tilde{\Omega} \geq 1, \quad \Delta\tilde{T}\Delta\tilde{F} \geq \frac{1}{2\pi},$$

$$\Delta\tilde{T} = \left[\int_0^\infty t^r dt\frac{1}{2\pi}\int_{-\infty}^\infty \Phi^r(t,\omega)d\omega\right]^{1/r},$$

$$\Delta\tilde{\Omega} = \left[\int_0^\infty t^{-s}dt\frac{1}{2\pi}\int_{-\infty}^\infty \Phi^s(t,\omega)d\omega\right]^{1/s}, \tag{7}$$

where $1/r + 1/s = 1$.

Another important generalization of theorems 1 and 2 is their application to the class of discrete systems.

For the class indicated, the expression for the uncertainty function takes the form

$$\Phi(n, m) = \frac{1}{\Omega}\sum_{j=0}^n k_j k_{n-j}e^{im(n/2-j)h}, \tag{8}$$

where

$$\Omega = \sum_{j=0}^\infty k_j^2, \quad h = \Delta\omega\Delta t, \quad k_j = k(j\Delta t).$$

Here, Δt and $\Delta\omega$ are the discrete time and discrete frequency, respectively, the Ω series being convergent.

For the constant volume of the uncertainty body

$$\frac{1}{2\pi}\sum_{n=0}^\infty \sum_{m=-\infty}^\infty \Phi^2(n, m) = 1, \tag{9}$$

we obtain

$$4\pi^2 = \sum_{n=0}^\infty \sum_{m=-\infty}^\infty \Phi(n, m)f(n)\Phi(n, m)f^{-1}(n),$$

where $f(n)$ is an arbitrary integer-valued function. Applying the discrete Bunyakowsky–Schwartz inequality to the last equality twice, we find

$$\Delta T_d\Delta\Omega_d \geq \Delta t\Delta\omega = h,$$

$$\Delta T_d\Delta F_d \geq \Delta t\frac{\Delta\omega}{2\pi} = \frac{h}{2\pi} = \bar{h}, \tag{10}$$

where

$$\Delta T_{\mathrm{d}} = \Delta t \sum_{n=0}^{\infty} f(n) \frac{1}{2\pi} \sum_{m=-\infty}^{\infty} \Phi^2(n, m),$$

$$\Delta \Omega_{\mathrm{d}} = \Delta \omega \sum_{n=0}^{\infty} f^{-1}(n) \frac{1}{2\pi} \sum_{m=-\infty}^{\infty} \Phi^2(n, m).$$

Since

$$\frac{1}{2\pi} \sum_{m=-\infty}^{\infty} \Phi^2(n, m) = \frac{1}{\Omega^2} \sum_{j=0}^{n} k_j^2 k_{n-j}^2,$$

then formulas (10) can also be expressed in the form

$$\Delta T_{\mathrm{d}} = \frac{\Delta t}{\Omega^2} \sum_{n=0}^{\infty} f(n) \sum_{j=0}^{n} k_j^2 k_{n-j}^2,$$

$$\Delta \Omega_{\mathrm{d}} = \frac{\Delta \omega}{\Omega^2} \sum_{n=0}^{\infty} f^{-1}(n) \sum_{j=0}^{n} k_j^2 k_{n-j}^2. \tag{11}$$

In particular, if we assume $f(n) = n$ in (10), then relationship (9) defines the inequality for the duration of the transient process and the frequency band for a discrete ACS.

Similarly to the above-said, we can show the equivalence of (9) and (10), i.e., the uncertainty principle for an ACS in the signal and quantum-mechanical forms, and also extend this result to unsteady systems and systems with a finite memory.

We now consider two examples.

Example 1. The sequential connection of an arbitrary number n of identical inertial links

$$Y(p) = \prod_{k=1}^{n} (1 + pT)^{-1}, \quad n = 1, 2, \ldots$$

Here,

$$k(\tau) = \frac{\tau^{n-1} e^{-\tau/T}}{(n-1)! T^n}, \quad \Omega = \frac{(2n-2)! \frac{1}{T}}{2^{2n-1} [(n-1)!]^2}.$$

According to (6),

$$\Delta T = (4n-2)T, \quad \Delta \Omega = \frac{1}{4n-3} \frac{1}{T},$$

$$\Delta T \Delta \Omega = \frac{4n-2}{4n-3} = 1 + \frac{1}{4n-3} > 1.$$

The quantity $\Delta T \Delta \Omega \longrightarrow 1$ as $n \longrightarrow \infty$; i.e., this estimate cannot be improved (changed by the value not equal to an infinitely small one).

Example 2. The vibration link of the second order $(1 + 2\xi Tp + T^2 p^2)^{-1}$, $0 < \xi < 1$.

Here,

$$k(\tau) = \frac{\alpha^2 + \beta^2}{\beta} e^{-\alpha\tau} \sin\beta\tau, \quad \Omega = \frac{\alpha^2 + \beta^2}{4\alpha},$$

$$\alpha = \xi T^{-1}, \quad \beta = \sqrt{1 - \xi^2} T^{-1}.$$

Using the notation $\alpha/\beta = \lambda$, we find

$$\Delta T = \frac{3\lambda^2 + 1}{\lambda^2 + 1} \alpha^{-1},$$

$$\Delta \Omega = (\lambda^2 + 1)[(3\lambda^2 + 2) - 3\lambda(\lambda^2 + 1)\operatorname{arccot}\lambda]\alpha,$$

$$\Delta T \Delta \Omega = (3\lambda^2 + 1)[(3\lambda^2 + 2) - 3\lambda(\lambda^2 + 1)\operatorname{arccot}\lambda].$$

For $\lambda = 1$, $\Delta T \Delta \Omega \simeq 1.15$ and for $\lambda \longrightarrow 0$, $\Delta T \Delta \Omega \longrightarrow 1$; i.e., it is not possible to improve this estimate.

The set of the parameters Δp, Δq, for which formulas (3) and (4) are valid, can be extended proceeding from the mutual uncertainty function [2] with the following form for an ACS:

$$\Phi_{12}(t, \omega) = \frac{1}{\sqrt{\Omega_1 \Omega_2}} \int_0^t k_1(\tau) k_2(t - \tau) e^{i\omega(t/2 - \tau)} d\tau. \tag{12}$$

Here, $k_1(\tau)$ and $k_2(\tau)$ are pulse transient functions belonging to the above-mentioned class and Ω_1 and Ω_2 are the corresponding effective transmission bands. In this case, it is sufficient to replace $\Phi(t, \omega)$ with $|\Phi_{12}(t, \omega)|$ in (1) and $\Phi(t, \omega)$ with $|\Phi_{21}(t, \omega)|$ in (2) in accordance with (12).

In conclusion, we emphasize that the uncertainty principle for ACS in the Heisenberg form illustrates the ACS stability to statistic actions (noises): the higher the stability with respect to the noise, the narrower the chosen frequency range must be. However, in this case, in the framework of (5) and (6), the duration of the process treatment must be longer and, correspondingly, the ACS operation rate decreases. A similar situation will also take place for the relationship between the noise and maneuvering in tracing problems.

REFERENCES

1. S. A. Klimov and V. I. Tumarkin, Dokl. Akad. Nauk **364**, 35 (1999).

2. A. I. Sinsky and C. D. Wang, IEEE Trans. Aerosp. Electron. Syst. **10** (4), 117 (1974).

3. E. Schredinger, *Selected Works on Quantum Mechanics* (Nauka, Moscow, 1976).

4. W. Siebert, in *Circuits, Signals, and Systems* (MIT Press, Cambridge, 1986; Mir, Moscow, 1988), Part 2.

Translated by G. Merzon

<div align="center">═══════ MECHANICS ═══════</div>

The Features of Deformation in Initially Porous Bars Undergoing a Damage

V. I. Kondaurov* and N. V. Kutlyarova**

Presented by Academician E.I. Shemyakin December 2, 1999

Structural materials and rocks containing pores, microcracks, and other microscopic defects distributed initially in their bulk have some specific features. The most significant of these are elastic deformations under low pressures and small shears and the accumulation of damage under more intense loads (including compression), resulting eventually in the macroscopic fracture of the material. The process of crack accumulation in such materials is accompanied by the development of irreversible bulk strains (dilatation or compaction). In the case of a relatively high level of initial porosity, this leads, specifically, to the following effect: the bar becomes thicker under tensile stress. The energy model used in this paper [1, 2] provides a unified picture, taking into account the afore-mentioned features of deformation and fracture in the initially porous materials.

According to the mathematical modeling of the behavior of the initially porous brittle materials, we will consider the effective medium initially isotropic and the strains small. The state of the particle (in the isothermal approximation) is characterized by a tensor of small strains $\mathbf{e}$ and by the scalar degree of the damage ω. The response of the medium is determined by symmetrical stress tensor $\boldsymbol{\sigma}$, by density of elastic potential $u(\mathbf{e}, \omega)$, and by specific effective surface energy $u_f(\omega)$. In this case, $\boldsymbol{\sigma} = \boldsymbol{\sigma}(\mathbf{e}, \omega)$, $u = u(\mathbf{e}, \omega)$ are isotropic functions of the symmetrical tensor $\mathbf{e}$.

The local balance equation for total energy $U(\mathbf{e}, \omega) = u_f(\omega) + u(\mathbf{e}, \omega)$, which is equal to the sum of the elastic potential and the effective surface energy, is written in the form

$$\rho \dot{U} = \boldsymbol{\sigma} : \dot{\mathbf{e}}, \tag{1}$$

where ρ is the density of material. The relation of the stress tensor and the energy density is given by the

─────────────

* *Moscow Institute of Physics and Technology,*
Institutskii per. 9, Dolgoprudnyǐ, Moscow oblast,
141700 Russia

** *Schmidt Joint Institute of Physics of Earth,*
Russian Academy of Sciences,
Bol'shaya Gruzinskaya ul. 10, Moscow,
123810 Russia

formula

$$\boldsymbol{\sigma}(\mathbf{e}, \omega) = \rho \frac{\partial U(\mathbf{e}, \omega)}{\partial \mathbf{e}}. \tag{2}$$

It follows from (1) and (2) that $\dot{\omega} \dfrac{\partial U(\mathbf{e}, \omega)}{\partial \omega} = 0$; i.e., in the medium undergoing a damage, two processes are possible, passive ($\dot{\omega} = 0$) and active. For the latter we have

$$\frac{\partial U(\mathbf{e}, \omega)}{\partial \omega} = 0, \quad \dot{\omega} > 0, \quad \omega \geq 0. \tag{3}$$

The density of total energy is postulated in the form

$$\rho U(\mathbf{e}, \omega) = \rho u_f^0 + \gamma \omega + \frac{1}{2} \beta \omega^2$$
$$+ \frac{1}{2} K I_1^2 + G J^2 - \alpha_p(I_1) \omega I_1 - \alpha_s \omega J. \tag{4}$$

The values of bulk strain I_1 and shear strain intensity J are determined by the relationship

$$I_1 = \mathbf{I} : \mathbf{e}, \quad J = (\mathbf{e}' : \mathbf{e}')^{1/2}, \quad \mathbf{e}' = \mathbf{e} - \frac{1}{3} I_1 \mathbf{I},$$

where $\mathbf{I}$ is the unit second-rank tensor. Parameters K, G, α_s, β, u_f^0, and γ of the medium are assumed to be dependent only on the properties of the frame and on the initial porosity. In contrast to the elastic potential of the damaged homogeneous medium [1], representation (4) contains function $\alpha_p(I_1)$, which is essentially sign-alternating. Under conditions of intense compression ($I_1 < 0$), this allows us to take into account the decrease in elastic potential with the growth of damage. From (2)–(4), it follows that

$$\boldsymbol{\sigma} = (K I_1 - \hat{\alpha}_p(I_1) \omega) \mathbf{I} + \left(2G - \frac{\alpha_s \omega}{J} \right) \mathbf{e}', \tag{5}$$

$$\hat{\alpha}_p(I_1) = \alpha_p(I_1) + I_1 \alpha_p'(I_1),$$

$$\omega = \frac{1}{\beta} \{ \alpha_p(I_1) I_1 + \alpha_s J - \gamma \}. \tag{6}$$

Within the framework of the proposed model, we consider the axially symmetric problem concerning the deformation of the infinite circular cylindrical bar with radius R_0 made of the material undergoing the damage and subjected to fixed tensile stress ($\sigma_0 > 0$). We will approximate the boundary of the elastic region in the half-plane of states (I_1, J) using piecewise linear function $J = f(I_1)$ (Fig. 1). Then, the condition of the onset for the active process, $\omega(I_1, J) = 0$, gives $\hat{\alpha}_p(I_1)$ as a piecewise constant function: $\hat{\alpha}_p = \alpha_s J_0/I_1^+$ for $I_1^* \leq I_1 \leq I_1^+$, $\hat{\alpha}_p = \alpha_s J_1/I_1^-$ for $I_1^- \leq I_1 \leq I_1^*$. We choose a cylindrical coordinate system (r, φ, z), whose z-axis coincides with the bar axis. The motion vector of a particle is denoted as $\mathbf{u} = (u(r, z), 0, w(r, z))$. The balance equations have the form

$$\frac{\partial\sigma_{rr}}{\partial r} + \frac{\partial\sigma_{rz}}{\partial z} + \frac{\sigma_{rr} - \sigma_{\varphi\varphi}}{r} = 0,$$

$$\frac{\partial\sigma_{rz}}{\partial r} + \frac{\partial\sigma_{zz}}{\partial z} + \frac{\sigma_{zr}}{r} = 0,$$

where σ_{rr}, $\sigma_{\varphi\varphi}$, σ_{zz}, and σ_{rz} are the nonzero physical components of the stress tensor.

The boundary conditions can be written as follows: for $r = R_0$

$$\sigma_{rr}(R_0, z) = 0, \ \sigma_{rz}(R_0, z) = 0;$$

for $r = 0$

$$u(0, z) = 0, \ \sigma_{rz}(0, z) = 0;$$

for $z = 0$

$$w(r, 0) = 0, \ \frac{\partial u(r, z)}{\partial z} = 0;$$

for $z \longrightarrow \infty$

$$\sigma_{rr}(r, z) \longrightarrow \sigma_0, \ \sigma_{rz}(r, z) \longrightarrow 0.$$

We will seek the solution in the form $u(r, z) = U_0 r$, $w(r, z) = W_0 z$, where $U_0 = \text{const}$, $W_0 = \text{const}$. Then, we obtain from (5) and (6)

$$\sigma_{rr}(r, z) = (KI_1 - \hat{\alpha}_p\omega(I_1, J))$$

$$+ \frac{1}{3}\left(2\mu - \frac{\alpha_s\omega(I_1, J)}{J}\right)(U_0 - W_0) = \text{const},$$

$$\sigma_{zz}(r, z) = (KI_1 - \hat{\alpha}_p\omega(I_1, J))$$

$$+ \frac{2}{3}\left(2\mu - \frac{\alpha_s\omega(I_1, J)}{J}\right)(W_0 - U_0) = \text{const},$$

(7)

$$\sigma_{\varphi\varphi} \equiv \sigma_{rr}, \quad \sigma_{rz} \equiv 0, \quad \omega = (\hat{\alpha}_p I_1 + \alpha_s J - \gamma),$$

$$I_1 = 2U_0 + W_0, \quad J = \sqrt{2/3}|(W_0 - U_0)|.$$

From boundary conditions $\sigma_{rr}(R_0) = 0$, $\sigma_{zz}(r) = \sigma_0$, $0 \leq r \leq R_0$ it follows that $\sigma_{rr}(r, z) \equiv 0$ and $\sigma_{zz}(r, z) \equiv \sigma_0$; consequently, the balance equations are satisfied iden-
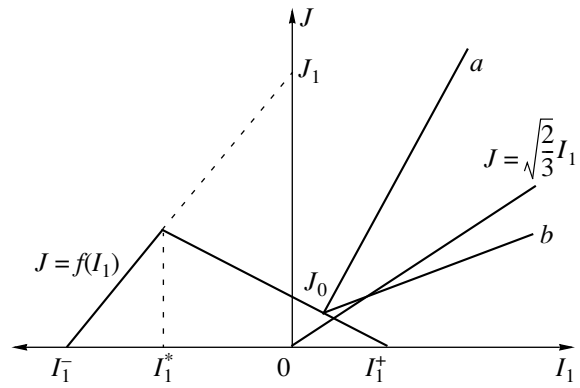
Fig. 1.

tically. Thus, solution $u(r, z) = U_0 r$, $w(r, z) = W_0 z$ meets the balance equations and boundary conditions.

Using (7), we can determine the values U_0 and W_0 from the set

$$\sigma_{rr}(U_0, W_0) = 0, \quad \sigma_{zz}(U_0, W_0) = \sigma_0; \qquad (8)$$

however, the solutions found by such a method are relatively cumbersome.

Below, in system (8), it is more convenient to pass to variables I_1 and J, which are defined by relationships (7). Then, the system is written in the form

$$AJ - BI_1 = C_1(\sigma_0), \quad -BJ + DI_1 = C_2(\sigma_0),$$

where $A = 2\mu - \dfrac{\alpha_s^2}{\beta}$, $B = \dfrac{d\alpha_s^2}{\beta}$, $D = K - \dfrac{d^2\alpha_s^2}{\beta}$, and $d = \dfrac{\hat{\alpha}_p}{\alpha_s}$ are the constant coefficients, which depend only on the parameters of the material, and $C_1 = \sqrt{\dfrac{2}{3}}\sigma_0 - \dfrac{\gamma\alpha_s}{\beta}$ and $C_2 = \dfrac{\sigma_0}{3} - \dfrac{d\gamma\alpha_s}{\beta}$ are the quantities determined both by the properties of the material and by applied load σ_0. The solutions of this system have the form

$$I_1(\sigma_0) = \frac{BC_1(\sigma_0) + AC_2(\sigma_0)}{AD - B^2},$$

$$J(\sigma_0) = \frac{DC_1(\sigma_0) + BC_2(\sigma_0)}{AD - B^2}.$$

(9)

From condition $\omega(I_1, J) = 0$, it follows that the process of damage accumulation in the bar starts when the applied load attains the value

$$\sigma_0 = \sigma_* \equiv \frac{3\sqrt{6}K\mu\gamma}{\alpha_s}(\sqrt{6}\mu d + 3K).$$

Since the process of cracking accumulation in the media undergoing a damage is accompanied by the

development of the irreversible bulk strain (dilatation or compaction) [3, 4], this can give rise to an often observed anomalous phenomenon, namely, to the thickening of the bar under tensile strain. Is it possible to describe this phenomenon within the framework of the model under discussion?

Note that the thickening of the bar arises at $U_0 > 0$. According to (7), this corresponds to $J < \sqrt{2/3}\, I_1$. This means that, at the points of plane (I_1, J) located above the line of the uniaxial deformation $J = \sqrt{2/3}\, I_1$, the tension of the bar is accompanied by a decrease in the bar diameter, whereas, at the points located under this line, thickening occurs. It follows from (9) that, in the active process, we have $J = aI_1 + b$, where

$$a = \frac{\sqrt{6}D + B}{\sqrt{6}B + A}, \quad b = \frac{(\sqrt{6}d - 1)\alpha_s\gamma/\beta}{\sqrt{6}B + A}.$$

The mutual arrangement of lines $J = \sqrt{2/3}\, I_1$ and $J = aI_1 + b$ allows us to make definite conclusions concerning the possible thinning or thickening of the bar based on σ_0 and on the parameters of the material. The onset of the damage accumulation process would be accompanied by the bar thickening if $J(\sigma_*) < \sqrt{2/3}\, I_1(\sigma_*)$. This condition corresponds to $2\mu > 3K$ or $-1 < \nu < 0$. Assuming that the Poisson coefficient for the isotropic materials varies within the range $0 \le \nu \le 0.5$, we find that $2\mu \le 3K$; i.e., $J(\sigma_*) \ge \sqrt{2/3}\, I_1(\sigma_*)$. Thus, within the framework of our model, the bar diameter always decreases at the onset of the damage accumulation. When σ_0 increases, one of two possible regimes shown in Fig. 1 occurs. For the material with $a > \sqrt{2/3}$ (Fig. 1, straight line a), the diameter of the bar decreases at all values of σ_0. At $a < \sqrt{2/3}$ (Fig. 1, straight line b), the decrease of the diameter of the bar occurs at small values of σ_0 corresponding to the neighborhood of the boundary of the elasticity domain. However, when the load reaches the value

$$\sigma_0 = \sigma^* \equiv \frac{(3K - 2\sqrt{6}\mu d)\gamma\alpha_s}{\beta(\sqrt{6}D - \sqrt{2/3}A - B)},$$

the bar diameter starts to increase.

Note that the first regime is characteristic of the initially homogeneous material with effective moduli differing only slightly from the elasticity moduli and, consequently, that $a = \sqrt{6}\, K/(2\mu) + o(1) > \sqrt{2/3}$. The second regime only becomes possible at a certain level of initial porosity.

Another characteristic feature of the deformation of the initially porous materials is the development of damage under compressing loads. Analysis similar to that presented above suggests that the damage accumulation is either always accompanied by the thickening of the bar or that the thickening occurs in the beginning of the active process. This depends on the material parameters and the magnitude of compressing stress σ_0. In the latter case, the thickening of the bar can change by the decrease in the bar diameter with the growth of the load due to the material compaction at the increase in the damage.

Let us consider now the rheological instability of the bar material. State $\mathbf{e}_0$ is referred to as *rheologically unstable* if there exists such a normal $\mathbf{n}_0$ that the velocity of the non-steady-state surface corresponding to the weak discontinuity obeys condition $c(\mathbf{e}_0, \mathbf{n}_0) \longrightarrow 0$ for $\mathbf{e} \longrightarrow \mathbf{e}_0$, $\mathbf{n} \longrightarrow \mathbf{n}_0$ [1]. The values of velocities c are determined by the following relationships [2]:

$$\rho c_{1,2}^2 = M + Q \pm (Q^2 + q)^{1/2}, \quad \rho c_3^2 = M,$$

$$Q(\mathbf{e}, \mathbf{n}) = K + \frac{1}{3}\mu - \check{\alpha}_p\omega$$

$$-\frac{1}{\beta}\mathbf{n}\cdot(\check{\alpha}_p\mathbf{I} + \alpha_s\mathbf{N})^2\cdot\mathbf{n} + \varphi\left(\mathbf{n}\cdot\mathbf{N}^2\cdot\mathbf{n} - \frac{1}{6}\right),$$

$$q = \zeta(\mathbf{n}\cdot\mathbf{N}^2\cdot\mathbf{n} - (\mathbf{n}\cdot\mathbf{N}\cdot\mathbf{n})^2), \quad \zeta = \xi^2 + \eta\Lambda,$$

$$\mathbf{N} = \frac{\mathbf{e}'}{J}, \quad \xi = \frac{\check{\alpha}_p\alpha_s}{\beta}, \quad \eta = \frac{\alpha_s^2}{\beta} - \varphi, \quad \varphi = \frac{\alpha_s\omega}{J},$$

$$\Lambda = K + \frac{1}{3}G - \frac{1}{6}\varphi - \frac{\check{\alpha}_p^2}{\beta} - \check{\alpha}'_p\omega, \quad M = G - \frac{1}{2}\varphi.$$

The vanishing of the smallest velocity defines the condition of rheological instability appearing in the material, whereas the direction of the extremal normal determines the shape of the stability loss domain. For $\mathbf{n} = (0, 0, 1)$, the rheological instability occurring in the form of the failure plane arises under condition $\varphi = 2\mu$. For $\mathbf{n} = (1, 0, 0)$, the condition of rheological instability has the form

$$\varphi = 2\left(\frac{4}{3}\mu + K - \left(\hat{\alpha}_p \mp \frac{\alpha_s}{\sqrt{6}}\right)^2\middle/\beta\right).$$

The failure plane, in this case, is the longitudinal plane of separation. This can be treated as the nucleation of the longitudinal crack separating the bar, which is
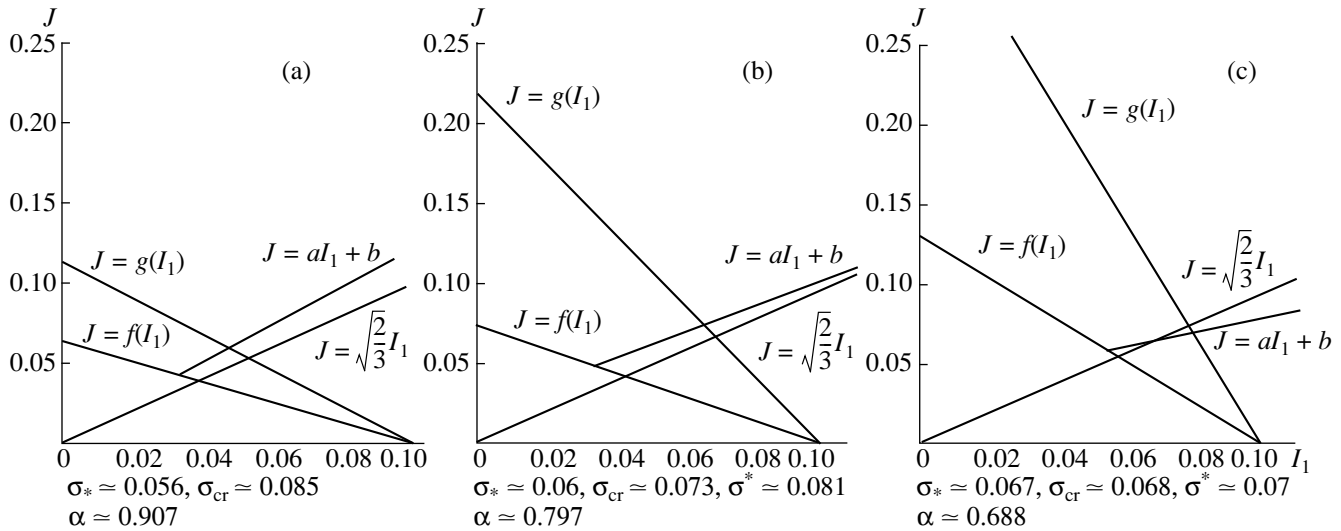
Fig. 2.

directed along the z-axis. The mechanism of crack formation was discussed in detail in [5, 6]. If

$$n_1^2 + n_2^2 - 2n_3^2 = \frac{1}{2} - \frac{M}{\zeta}\left(\frac{\varphi}{2} + \left(\sqrt{6}d - \frac{1}{2}\right)\frac{\alpha_s^2}{\beta}\right),$$

then the failure surface is a cone with normal **n** determined as described. The smallest possible value of $\varphi = \varphi_*$ determines the shape of the failure surface arising earliest.

The results of numerical calculations for the specific case of $E/\beta = 1.3$, $\gamma/\beta = 0.1$, $\alpha_s/\beta = 0.7$, and $I_1^+ = 0.1$ are presented in Fig. 2. Depending on the value of tangent d (the slope of the boundary of the elasticity domain), we found the following possible regimes of the bar deformation. For $d = 0.6$ (Fig. 2a), the active process of loading is accompanied by the decrease in the bar diameter until a loss of stability occurs. For $d = 0.7$ (Fig. 2b), a possible thickening of the bar does not take place since the stress σ^* needed to generate such a regime is higher than σ_{cr}. If $d = 0.8$ (Fig. 2c), the decrease of the bar diameter changes by its increase when the applied stress attains value σ^*. This increase

Taking into account the definition of φ and expression for ω, we find

$$J = -d\left[1 - \frac{\varphi\beta}{\alpha_s^2}\right]^{-1} I_1 + \frac{\alpha\gamma}{\alpha_s^2 - \varphi\beta}.$$

Straight line $J = g(I_1)$ from this family, corresponding to φ_*, bounds the domain of the steady-state deformation of the bar in plane (I_1, J) (Fig. 2). Thus, there exists the critical value

$$\sigma_{cr} = \frac{\left\{K(2\mu - \varphi_*)\gamma\frac{\alpha_s}{\beta}\right\}}{\left\{\sqrt{\frac{2}{3}}\frac{\alpha_s^2}{\beta}\left(\sqrt{\frac{2}{3}}\mu d \pm K\right) + \varphi_*\left(d\left(d - \frac{1}{2}\right)\frac{\alpha_s^2}{\beta} \mp \sqrt{\frac{2}{3}}K\right)\right\}},$$

at which the bar looses its rheological stability.

continues as long as the bar retains its rheological stability. In all cases under discussion, the rheological instability arises at conical surfaces.

Thus, a solution constructed based on the proposed fracture model describes the following features characterizing the behavior of the bar undergoing a damage. For $|\sigma_0| < |\sigma_*|$, the bar is in an elastic state, its tension is accompanied by an increase in its diameter. In the case when the applied stress is in the range $|\sigma_*| \leq |\sigma_0| \leq |\sigma_{cr}|$, the state of the bar is characterized by the damage accumulation process, the bar extension can be accompanied by thickening owing to the dilatation, and the compression of the bar can be accompanied by a decrease in its transverse size as related to compaction. For $|\sigma_0| =$

$|\sigma_{cr}|$, the material of the bar becomes rheologically unstable. This instability can be interpreted as the result of macroscopic failures nucleating in the bar and oriented in a regular manner.

ACKNOWLEDGMENTS

REFERENCES

1. V. I. Kondaurov, Prikl. Mat. Mekh. **52**, 302 (1988).
2. V. I. Kondaurov, N. V. Kutlyarova, and V. E. Fortov, Dokl. Akad. Nauk **355**, 342 (1997) [Phys.–Dokl. **42**, 395 (1997)].
3. V. N. Nikolaevskiĭ, *Mechanics of Porous and Cracked Media* (Nedra, Moscow, 1984).
4. R. I. Nigmatulin, *Mechanics of Heterogeneous Media* (Nauka, Moscow, 1978).
5. L. V. Nikitin and V. N. Odintsev, Izv. Akad. Nauk SSSR, Mekh. Tverd. Tela, No. 6, 135 (1988).
6. V. N. Odintsev, *Break-off Fracture of Rock Massifs* (Moscow, 1996).

Translated by T. Galkina

═══════════════ **MECHANICS** ═══════════════

Differentiation of Energy Functionals in the Theory of Cracks with Possible Edge Contact

J. Sokolowskiĭ* and A. M. Khludnev**

Presented by Academician V.P. Myasnikov December 27, 1999

Dependence of energy functionals on crack shape is important in fracture mechanics. In particular, when the Griffith's fracture criterion is formulated, the derivative of the energy functional with respect to crack length is the basic parameter [1]. In classical crack theory, the boundary conditions specified at the edges have the form of equalities. This can lead to contradictions. In fact, the solutions can correspond to the interpenetration of opposite crack edges [2, 3]. Derivatives of energy functionals with respect to crack length are known in the classical theory [4, 5]. Variation of crack shape was studied in [6] for the three-dimensional case with the classical boundary conditions $\sigma_{ij}n_j = 0$ ($i = 1, 2, 3$) at the edges. Recently, there appeared significant advances in nonlinear crack theory based on boundary conditions corresponding to noninterpenetrating edges [7]. In this paper, we consider the boundary value problems that ensure the absence of edge interpenetration and derive formulas for derivatives of the energy functionals with respect to crack length.

1. Two-dimensional case. Let $D \subset R^2$ be a bounded domain with smooth boundary Γ. The set

$$\Xi_{l+\delta} = \{(x_1, x_2) \,|\, 0 < x_1 < l + \delta,\ x_2 = 0\}$$

models a crack, where $l > 0$ and δ is the parameter which tends afterwards to zero. We assume that, for all sufficiently small δ, $\Xi_{l+\delta}$ belongs to D and consider domains $\Omega_\delta = D \backslash \bar\Xi_{l+\delta}$ and $\Omega = D \backslash \bar\Xi_l$ with cuts $\Xi_{l+\delta}$ and Ξ_l, respectively.

Below, we present the formulation of the equilibrium problem for a linearly elastic body, which, in the

---

* *Laboratoire de Mathématiques, Institut Elie Cartan,*
  Université Henri Poincare, Nancy I BP 239,
  Vandoeuvre-Les-Nancy Cedex, 54506 France
  E-mail: sokolovs@iecn.u-nancy.fr

** *Lavrent'ev Institute of Hydrodynamics,*
  Siberian Division, Russian Academy of Sciences,
  pr. Akademika Lavrent'eva 15, Novosibirsk,
  630090 Russia
  E-mail: khlud@hudro.nsc.ru

undeformed state, occupies domain Ω. We need to determine vector function $W = (u, v)$ such that

$$-\sigma_{ij,j} = f_i \quad \text{in} \ \Omega, \quad i = 1, 2, \tag{1.1}$$

$$W = 0 \quad \text{at} \ \Gamma, \tag{1.2}$$

$$[v] \geq 0, \quad \sigma_{22} \leq 0, \quad [\sigma_{22}] = 0, \quad \sigma_{12} = 0,$$
$$[v]\sigma_{22} = 0 \quad \text{at} \ \Xi_l. \tag{1.3}$$

Here, $\sigma_{ij} = \sigma_{ij}(W)$ are the components of stress tensor and $[v] = v^+ - v^-$ is the jump of function v across Ξ_l. The signs $\pm$ correspond to positive and negative directions of normal $n = (0, 1)$ to set $\Xi_{l+\delta}$. The summation is performed over identical subscripts. The subscript after the comma denotes differentiation. It is assumed that the Hooke's law

$$\sigma_{ij} = 2\mu\varepsilon_{ij} + \lambda \operatorname{div} W \delta_j^i, \quad i, j = 1, 2 \tag{1.4}$$

holds. Here, $\lambda \geq 0$ and $\mu > 0$ are the Lamé parameters, δ_j^i is the Kronecker delta, $\varepsilon_{ij} = \varepsilon_{ij}(W)$ are the components of the strain tensor, $\varepsilon_{11} = u_{x_1}$, $\varepsilon_{22} = v_{x_2}$, and $\varepsilon_{12} = 1/2(u_{x_2} + v_{x_1})$. For the given external load, we assume that $f = (f_1, f_2) \in C^1(\bar D)$. The first inequality in (1.3) is interpreted as a condition ensuring the noninterpenetration of opposite crack edges.

Let $\langle \cdot, \cdot \rangle$ and $\langle \cdot, \cdot \rangle_\delta$ be scalar products in $L^2(\Omega)$ and $L^2(\Omega_\delta)$, respectively. Relationships (1.1)–(1.3) are, in fact, the differential representations of the problem concerning the minimization of the functional

$$I(\Omega; U) = \frac{1}{2}\langle \sigma_{ij}(U), \varepsilon_{ij}(U)\rangle - \langle f, U \rangle,$$
$$U = (u, v) \tag{1.5}$$

at a convex closed set of the Sobolev space. Namely, we introduce the closed convex sets

$$K_0 = \{(u, v) \in H^1(\Omega) \,|\, u = v = 0 \ \text{at} \ \Gamma, \ [v] \geq 0 \ \text{at} \ \Xi_l\},$$

$$K_\delta = \{(u, v) \in H^1(\Omega_\delta) \,|\, u = v = 0 \ \text{at} \ \Gamma, \ [v] \geq 0 \ \text{at} \ \Xi_{l+\delta}\}.$$

Function $W \in K_0$ is a solution to the variational inequality

$$\langle \sigma_{ij}(W), \varepsilon_{ij}(V) - \varepsilon_{ij}(W) \rangle \geq \langle f, V - W \rangle \quad \forall V \in K_0. \quad (1.6)$$

In addition to problem (1.1)–(1.3), we consider a family of the perturbed problems. Namely, the determination of vector function $W^\delta = (u^\delta, v^\delta)$ is required. This function meets the following conditions:

$$-\sigma_{ij,j} = f_i \quad \text{in } \Omega_\delta, \quad i = 1, 2, \quad (1.7)$$

$$W^\delta = 0 \quad \text{at } \Gamma, \quad (1.8)$$

$$[v^\delta] \geq 0, \quad \sigma_{22} \leq 0, \quad [\sigma_{22}] = 0,$$
$$\sigma_{12} = 0, \quad [v^\delta]\sigma_{22} = 0 \quad \text{at } \Xi_{l+\delta}. \quad (1.9)$$

Here, we have $\sigma_{ij} = \sigma_{ij}(W^\delta)$ and $\varepsilon_{ij} = \varepsilon_{ij}(W^\delta)$, where σ_{ij} and ε_{ij} are related by Hooke's law (1.4). Similarly to problem (1.1)–(1.3), function $W^\delta \in K_\delta$ is a solution to the variational inequality

$$\langle \sigma_{ij}(W^\delta), \varepsilon_{ij}(V) - \varepsilon_{ij}(W^\delta) \rangle_\delta \geq \langle f, V - W^\delta \rangle_\delta$$
$$\forall V \in K_\delta, \quad (1.10)$$

which, consequently, minimizes the functional

$$I(\Omega_\delta; U) = \frac{1}{2}\langle \sigma_{ij}(U), \varepsilon_{ij}(U) \rangle_\delta - \langle f, U \rangle_\delta,$$
$$U = (u, v)$$

at set K_δ. Let $J(\Omega_\delta) = I(\Omega_\delta; W^\delta)$ and $J(\Omega) = I(\Omega; W)$. In this paper, we intend to justify the differentiability of the energy functional with respect to crack length and to derive the corresponding formula, i.e., to find the following limit:

$$\lim_{\delta \to 0} \frac{J(\Omega_\delta) - J(\Omega)}{\delta}, \quad (1.11)$$

where W^δ and W are the solutions to problems (1.6) and (1.10), respectively. The following statement is valid:

Theorem 1. *The derivative of the energy functional with respect to crack length can be calculated using the relationship*

$$\frac{dJ(\Omega_\delta)}{d\delta}\bigg|_{\delta=0} = \frac{1}{2}\int_\Omega ((2\mu + \lambda)u_{,1}^2(-\theta_{,1}) + \mu u_{,2}^2 \theta_{,1}$$

$$+ 2\mu u_{,1} u_{,2}(-\theta_{,2}) + \mu v_{,1}^2(-\theta_{,1}) + (2\mu + \lambda)v_{,2}^2 \theta_{,1}$$
$$+ 2(\lambda + \mu)u_{,1} v_{,1}(-\theta_{,2}) \quad (1.12)$$

$$+ 2(2\mu + \lambda)v_{,1} v_{,2}(-\theta_{,2})) - \int_\Omega (\theta f_1)_{,1} u - \int_\Omega (\theta f_2)_{,1} v.$$

Here, function θ is sufficiently smooth and finite in D. It is equal to unity and zero in the vicinity of points $x_l = (l, 0)$ and $(0, 0)$, respectively. It can be proved that the right-hand side of (1.12) is independent of θ. Relationship (1.12) is usually referred to as the Griffith's

formula. In the framework of two-dimensional elasticity theory with nonlinear boundary conditions (1.3) at crack edges, the Griffith's formula determines the value of the derivative of the energy functional with respect to the crack length.

According to [7], a solution to problem (1.6) has an additional smoothness compared to that of the variational procedure. Namely, for any $x \in \Xi_l$, there exists a certain vicinity V of the point x such that $W \in H^2(V \backslash \Xi_l)$. Consequently, conditions (1.3) are met almost everywhere at Ξ_l. Note that the equality $\sigma_{22} = (2\mu + \lambda)v_{,2} + \lambda u_{,1}$ holds here. In addition to (1.3), we can prove the validity of boundary condition

$$[\sigma_{22} v_{,1}] = \sigma_{22}[v_{,1}] = 0 \quad \text{a.e. on } \Xi_l. \quad (1.13)$$

The Griffith's formula (1.12) can be written in a form not containing the function θ. For this purpose, we choose circle $B_{x_l}(r)$ having radius r and boundary $\Gamma(r)$ in such a way that $\theta = 1$ in $B_{x_l}(r)$. Then, integration by parts in (1.12) yields

$$\frac{dJ(\Omega_\delta)}{d\delta}\bigg|_{\delta=0} = I + \int_{B_{x_l}(r) \backslash \Xi_l} (f_1 u_{,1} + f_2 v_{,1}), \quad (1.14)$$

where

$$I = \frac{1}{2}\int_{\Gamma(r)} \nu_1((2\mu + \lambda)(u_{,1}^2 - v_{,2}^2) + \mu(v_{,1}^2 - u_{,2}^2))$$

$$+ \int_{\Gamma(r)} \nu_2((2\mu + \lambda)v_{,1} v_{,2} + (\lambda + \mu)u_{,1} u_{,2} + \mu u_{,1} u_{,2})$$

and (ν_1, ν_2) is the unit outer normal to $\Gamma(r)$. The right-hand side of (1.14) is independent of r. Thus, we have proven the following property. Let W be a solution to problem (1.6) and f be equal to zero in a certain vicinity of the point x_l. Then, integral I is independent of r for all sufficiently small r. Moreover, we consider the integral

$$I_C = \frac{1}{2}\int_C \nu_1((2\mu + \lambda)(u_{,1}^2 - v_{,2}^2) + \mu(v_{,1}^2 - u_{,2}^2))$$
$$\quad (1.15)$$
$$+ \int_C \nu_2((2\mu + \lambda)v_{,1} v_{,2} + (\lambda + \mu)u_{,1} v_{,1} + \mu u_{,1} u_{,2})$$

along curve C enclosing point x_l. Then, $\nu = (\nu_1, \nu_2)$ is the unit normal to the curve C. A part of this curve can coincide with Ξ_l. Let $\Xi = \Xi_l \cap C$. Then, according to (1.13) and (1.3), integrals in (1.15) can be taken along edges Ξ^+ and Ξ^-. We assume that function f vanishes in the domain with boundary C. The following statement holds:

Theorem 2. *Let the function f be equal to zero in the neighborhood of point x_l. Then, integral I_C is independent of the curve C.*

The integral in form (1.15) is called the Rice–Cherepanov integral. We demonstrated the independence of this integral from the integration path for nonlinear boundary conditions (1.3). The available results concerning the independence of the Rice–Cherepanov integral of the integration path relate to the boundary conditions $\sigma_{22} = 0$, $\sigma_{12} = 0$, which are met on $\Xi_l^{\pm}$ [8]. In this connection, the integral is usually written out in the form

$$\int_C \left(\sigma_{ij} \nu_j w_{,1}^i - \frac{1}{2} \sigma_{ij} \varepsilon_{ij} \nu_1 \right). \qquad (1.16)$$

Here, $(w^1, w^2) = (u, v)$. The direct verification shows that integrands in (1.15) and (1.16) coincide with each other; hence, integral (1.15) has the classical form.

2. Three-dimensional case. Let $D \subset R^3$ be a bounded domain with a smooth boundary Γ. A crack is modeled by the surface

$$\Xi_{l+\delta}$$
$$= \{(x_1, x_2, x_3) | x_3 = 0, -h < x_2 < h, 0 < x_1 < l + \delta\}.$$

Here, $h > 0$, $l > 0$, and δ is a small parameter. We assume that $\Xi_{l+\delta} \subset D$ for all sufficiently small δ and use the notation $\Omega_\delta = D \backslash \overline{\Xi}_{l+\delta}$ and $\Omega = D \backslash \overline{\Xi}_l$.

Below, we present the formulation of the equilibrium problem for an elastic body, which, in an undeformed state, occupies domain Ω. We need to find function $W = (u, v, w)$ such that

$$-\sigma_{ij,j} = f_i \text{ in } \Omega, \quad i = 1, 2, 3, \qquad (2.1)$$

$$W = 0 \text{ at } \Gamma, \qquad (2.2)$$

$$[W]n \geq 0, \quad \sigma_n \leq 0, \quad [\sigma_n] = 0,$$
$$\sigma_\tau = 0, \quad \sigma_n \cdot [W]n = 0 \text{ at } \Xi_l. \qquad (2.3)$$

Here, $\sigma_{ij} = \sigma_{ij}(W)$ are the components of the stress tensor, $n = (0, 0, 1)$ is the normal to the surface $\Xi_{l+\delta}$, and $\{\sigma_{ij} n_j\}_{i=1}^3 = \sigma_n \cdot n + \sigma_\tau$. We assume that Hooke's law holds in the form (1.4) for the three-dimensional case, $\varepsilon_{ij}(W) = \frac{1}{2}(w_{,j}^i + w_{,i}^j)$ and $(w^1, w^2, w^3) \equiv (u, v, w)$.

Similar to the two-dimensional case, problem (2.1)–(2.3) reduces to the minimization of the functional

$$I(\Omega; U) = \frac{1}{2} \langle \sigma_{ij}(U), \varepsilon_{ij}(U) \rangle - \langle f, U \rangle,$$
$$U = (u, v, w)$$

on the set

$$K_0 = \{(u, v, w) \in H^1(\Omega) | u = v = w = 0 \text{ at } \Gamma,$$
$$[w] \geq 0 \text{ at } \Xi_l \},$$

where $f = (f_1, f_2, f_3) \in C^1(\overline{D})$ is the given function.

The perturbed problem corresponding to (2.1)–(2.3) can be formulated as follows. It is needed to find function $W^\delta = (u^\delta, v^\delta, w^\delta)$ such that

$$-\sigma_{ij,j} = f_i \text{ in } \Omega_\delta, \quad i = 1, 2, 3, \qquad (2.4)$$

$$W^\delta = 0 \text{ at } \Gamma, \qquad (2.5)$$

$$[W^\delta]n \geq 0, \quad \sigma_n \leq 0, \quad [\sigma_n] = 0,$$
$$\sigma_\tau = 0, \quad \sigma_n \cdot [W^\delta]n = 0 \text{ at } \Xi_{l+\delta}. \qquad (2.6)$$

Here, $\sigma_{ij} = \sigma_{ij}(W^\delta)$ where $\sigma_{ij}(W^\delta)$ and $\varepsilon_{ij}(W^\delta)$ satisfy the Hooke's law. As above, problem (2.4)–(2.6), in fact, reduces to the minimization of the functional

$$I(\Omega_\delta; U) = \frac{1}{2} \langle \sigma_{ij}(U), \varepsilon_{ij}(U) \rangle_\delta - \langle f, U \rangle_\delta,$$
$$U = (u, v, w)$$

on the set

$$K_\delta = \{(u, v, w) \in H^1(\Omega_\delta) | u = v = w = 0 \text{ at } \Gamma,$$
$$[w] \geq 0 \text{ at } \Xi_{l+\delta} \}.$$

Let us denote the energy functionals as $J(\Omega_\delta) = I(\Omega_\delta; W^\delta)$ and $J(\Omega) = I(\Omega; W)$, where W^δ and W are solutions to problems (2.1)–(2.3) and (2.4)–(2.6), respectively. The problem is to find the derivative in the form of (1.11) for this case.

Theorem 3. *The derivative of the energy functional in problem (2.1)–(2.3) can be calculated by the use of the following Griffith's formula:*

$$\frac{dJ(\Omega_\delta)}{d\delta} \bigg|_{\delta=0} = \frac{1}{2} \int_\Omega \Big((2\mu + \lambda)(u_{,1}^2(-\theta_{,1}) + v_{,2}^2 \theta_{,1}$$

$$+ w_{,3}^2 \theta_{,1} + 2v_{,1} v_{,2}(-\theta_{,2}) + 2w_{,1} w_{,3}(-\theta_{,3}))$$

$$+ \mu(u_{,2}^2 \theta_{,1} + v_{,1}^2(-\theta_{,1}) + u_{,3}^2 \theta_{,1} + w_{,1}^2(-\theta_{,1}) + v_{,3}^2 \theta_{,1}$$

$$+ w_{,2}^2 \theta_{,1} + 2u_{,1} u_{,3}(-\theta_{,3}) + 2u_{,1} w_{,1}(-\theta_{,3})$$

$$+ 2v_{,1} v_{,3}(-\theta_{,3}) + 2v_{,1} w_{,2}(-\theta_{,3}) + 2v_{,3} w_{,1}(-\theta_{,2}) \quad (2.7)$$

$$+ 2w_{,1} w_{,2}(-\theta_{,2}) + 2u_{,1} u_{,2}(-\theta_{,2}) + 2v_{,1} u_{,1}(-\theta_{,2})$$

$$+ 2v_{,3} w_{,2} \theta_{,1}) + 2\lambda(v_{,2} w_{,3} \theta_{,1} + u_{,1} w_{,1}(-\theta_{,3})$$

$$+ v_{,2} w_{,1}(-\theta_{,3}) + v_{,1} w_{,3}(-\theta_{,2}) + u_{,1} v_{,1}(-\theta_{,2})) \Big)$$

$$-\int_{\Omega}(\theta f_1)_{,1}u - \int_{\Omega}(\theta f_2)_{,1}v - \int_{\Omega}(\theta f_3)_{,1}w,$$

where the function θ *is smooth and finite in D and equal to unity and zero in the vicinity of sets* $L = \{(x_1, x_2, x_3)|\ x_1 = l, -h < x_2 < h, x_3 = 0\}$ *and* $M = \{(x_1, x_2, x_3)|\ x_1 = 0, -h < x_2 \le h, x_3 = 0\}$, *respectively.*

Similar to the two-dimensional case, we can show that the right-hand side of (2.7) is independent of θ. We reduce (2.7) to the form not containing function θ. For this purpose, we consider the vicinity S_L of the set L having smooth boundary Γ_L under the assumption that $\theta = 1$ in S_L. According to our notation, (ν_1, ν_2, ν_3) is the unit outer normal to Γ_L. Integration by parts in (2.7) yields

$$\left.\frac{dJ(\Omega_\delta)}{d\delta}\right|_{\delta=0} = \int_{S_L}(f_1 u_{,1} + f_2 v_{,1} + f_3 w_{,1})$$

$$+\frac{1}{2}\int_{\Gamma_L}\nu_1((2\mu+\lambda)(u_{,1}^2 - v_{,2}^2 - w_{,3}^2)$$

$$+\mu(v_{,1}^2 - u_{,2}^2 - u_{,3}^2 + w_{,1}^2 - v_{,3}^2 - w_{,2}^2 - 2v_{,3}w_{,2})$$

$$-2\lambda v_{,2}w_{,3}) + \int_{\Gamma_L}\nu_2((2\mu+\lambda)v_{,1}v_{,2} \qquad (2.8)$$

$$+\mu(v_{,3}w_{,1} + w_{,1}w_{,2} + u_{,1}u_{,2} + v_{,1}u_{,1})$$

$$+\lambda(v_{,1}w_{,3} + u_{,1}v_{,1})) + \int_{\Gamma_L}\nu_3((2\mu+\lambda)w_{,1}w_{,3}$$

$$+\mu(u_{,1}u_{,3} + u_{,1}w_{,1} + v_{,1}v_{,3} + v_{,1}w_{,2})$$

$$+\lambda(u_{,1}w_{,1} + v_{,2}w_{,1})).$$

Denoting the functional in the right-hand side of (2.8) as $k(l, h, f)$, we can write (2.8) in the form

$$\left.\frac{dJ(\Omega_\delta)}{d\delta}\right|_{\delta=0} = k(l, h, f).$$

Thus, $J(\Omega_\delta) = J(\Omega) + k(l, h, f)\delta + \alpha(\delta)\delta$, where $\alpha(\delta) \longrightarrow 0$ as $\delta \longrightarrow 0$. Note that $k(l, h, f)$ does not depend on the choice of neighborhood S_L. If function f is equal to zero in the vicinity of set L, then the sum of the corresponding integrals can be interpreted as an analog of the Rice–Cherepanov integral, since the right-hand side of (2.8) does not depend on Γ_L.

The proposed method allowing us to determine the derivative of the energy functional provides an opportunity to analyze more complicated crack front perturbations in the three-dimensional case. We assume that, in an unperturbed state, the crack front is determined by equation $x_1 = g(x_2)$, where g is the given function which satisfies the Lipshitz condition such that $g(-h) = g(h) = l$. The perturbed crack front is described by equation $x_1 = g(x_2) + \delta$. We assume that the chosen function θ meets condition $\theta \in C_0^\infty(D)$ and is equal to unity and zero in the neighborhood of sets $\{(x_1, x_2, x_3)|\ x_1 = g(x_2), -h < x_2 < h, x_3 = 0\}$ and M, respectively. Then, the Griffith's formula also has form (2.7), where domain Ω corresponds to the front $x_1 = g(x_2)$.

Similarly, let the crack front be determined by equation $x_1 = l$ and a front perturbation have the form $x_1 = l + \delta g(x_2)$. The given function g is assumed to be sufficiently smooth such that $g(-h) = g(h) = 0$. We choose function θ in the same way as before. Then, the Griffith's formula takes the form (2.7), where function θ should be substituted by $g\theta$.

ACKNOWLEDGMENTS

REFERENCES

1. G. P. Cherepanov, *Mechanics of Brittle Fracture* (Nauka, Moscow, 1974; McGraw-Hill, New York, 1979).

2. N. F. Morozov, *Mathematical Problems of the Fracture Theory* (Nauka, Moscow, 1984).

3. R. V. Gol'dshteĭn and V. M. Entov, *Qualitative Methods in the Mechanics of Continuous Media* (Nauka, Moscow, 1989).

4. V. G. Maz'ya and S. A. Nazarov, Tr. Mosk. Mat. O–va. **50**, 79 (1987).

5. P. Grisvard, *Singularities in Boundary Value Problems* (Masson, Paris, 1992).

6. K. Ohtsuka, Lect. Notes Numer. Appl. Anal. **13**, 39 (1994).

7. A. M. Khludnev and J. Sokolowski, *Modeling and Control in Solid Mechanics* (Birkhauser, Bazel, 1997).

8. V. Z. Parton and E. M. Morozov, *Mechanics of Elastoplastic Fracture* (Nauka, Moscow, 1985).

Translated by Yu. Verevochkin